The Lunar Dust Environment

by

Jamey Robert Szalay

B.S., Physics, *magna cum laude*

B.S., Mathematics, *with distinction*

James Madison University, Harrisonburg, VA, 2006

A thesis submitted to the

Faculty of the Graduate School of the

University of Colorado in partial fulfillment

of the requirements for the degree of

Doctor of Philosophy

Department of Physics

2015

This thesis entitled:
The Lunar Dust Environment
written by Jamey Robert Szalay
has been approved for the Department of Physics

_____

Mihály Horányi

_____

Sascha Kempf

Date _____

The final copy of this thesis has been examined by the signatories, and we find that both the content and the form meet acceptable presentation standards of scholarly work in the above mentioned discipline.

Szalay, Jamey Robert (Ph.D., Physics)

The Lunar Dust Environment

Thesis directed by Prof. Mihály Horányi

Planetary bodies throughout the solar system are continually bombarded by dust particles, largely originating from cometary activities and asteroidal collisions. Surfaces of bodies with thick atmospheres, such as Venus, Earth, Mars and Titan are mostly protected from incoming dust impacts as these particles ablate in their atmospheres as 'shooting stars'. However, the majority of bodies in the solar system have no appreciable atmosphere and their surfaces are directly exposed to the flux of high speed dust grains. Impacts onto solid surfaces in space generate charged and neutral gas clouds, as well as solid secondary ejecta dust particles. Gravitationally bound ejecta clouds forming dust exospheres were recognized by in situ dust instruments around the icy moons of Jupiter and Saturn, and had not yet been observed near bodies with refractory regolith surfaces before NASA's Lunar Dust and Environment Explorer (LADEE) mission.

In this thesis, we first present the measurements taken by the Lunar Dust Explorer (LDEX), aboard LADEE, which discovered a permanently present, asymmetric dust cloud surrounding the Moon. The global characteristics of the lunar dust cloud are discussed as a function of a variety of variables such as altitude, solar longitude, local time, and lunar phase. These results are compared with models for lunar dust cloud generation. Second, we present an analysis of the groupings of impacts measured by LDEX, which represent detections of dense ejecta plumes above the lunar surface. These measurements are put in the context of understanding the response of the lunar surface to meteoroid bombardment and how to use other airless bodies in the solar system as detectors for their local meteoroid environment. Third, we present the first in-situ dust measurements taken over the lunar sunrise terminator. Having found no excess of small grains in this region, we discuss its implications for the putative population of electrostatically lofted dust.

Dedication

To my Mom, for always providing me with abundant love and encouragement to be inquisitive and follow my passions. And, to my Dad, for being a strong role model even in absence, living on through our fond memories.

Acknowledgements

Looking back on the journey to completing this thesis, I am grateful to the many people who have helped steer my career trajectory along the way.

To John Fisher, who got me interested both in science and school in general. I may very well have not pursued a career in physics without his teaching;

To Will Devereux, who introduced me to space & planetary science and solidified my goal of pursuing research on the solar system;

To Dorn Peterson and Don Chodrow, who inspired me to continue a graduate career in physics by making undergraduate physics challenging, fun, and rewarding;

To David James, for making the many long days of LDEX pipeline development a really neat experience;

To Andrew Poppe, who sold me on CU and NH/SDC, mentored me for the year we overlapped in grad school, and whose scientific success and drive gave me a goal to strive for;

To Dave McComas, for encouraging me to continue my scientific career and giving me the opportunity to do so;

And especially, to my advisor, Mihály Horányi. When I arrived at CU, I was an eager, albeit wide-eyed college grad. From day one, Mihály always encouraged me to follow my interests and fostered my ability to hone in on interesting and fruitful scientific pursuits. I'm very fortunate to have spent my graduate tenure under his patient and astute tutelage, which led me to be the driven and motivated scientist I am today.

Contents

Chapter

Tables

Table

Figures

Figure

Chapter 1

Introduction

1.1 Dust in the Solar System

Dust is pervasive throughout the observable universe. It forms the building blocks of planetary bodies, as they are formed from the accretion of dust particles aggregating into much larger objects [7, 53]. While dust particles impacting planetary bodies at very low speeds contribute to their mass through accretion, high speed impacts from dust grains can liberate orders of magnitude more mass than the impacting particle. In this way, all planetary bodies can be both sources and sinks for dust grains.

In our solar system, dust grains can be grouped according to their sources or parent body populations. These sources include comets, both long period Halley Type Comets (HTC) and short period Jupiter Family Comets (JFC), asteroids, Oort Cloud Comets (OCC), and Edgeworth-Kuiper Belt Objects (KBO). Grains from all of these sources comprise the interplanetary dust particle (IDP) population. Each of these populations can further broken down into subpopulations. There is also a population of grains which originate from outside our solar system, interstellar grains (ISD). ISD's were first detected by the dust detector onboard the Ulysses spacecraft [37] and were identified to come from the direction of our solar system's relative motion within the local interstellar medium at 26 km/s.

1.2 The Dust Environment at the Moon

Characterizing the meteoroid environment at 1 AU is an active area of research and remains challenging in many regards. Meteoric influx at Earth is measured via visual [46, 18] and radar observations [8, 11], whose detection limits are highly sensitive to the mass and speed in incoming particles. A number of spacecraft-based measurements of the meteoroid distribution at 1 AU have also been made, namely by Pioneer 8, Pioneer 9, Helios, & HEOS [35], the Long Duration Exposure Facility [55], the Global Imaging Monitor of the Ionosphere Experiment [14] and Space Dust Experiment [81] aboard the Advanced Research and Global Observation Satellite, and the Cosmic Dust Experiment onboard the Aeronomy of Ice in the Mesosphere mission [68].

Before the Lunar Atmosphere and Dust Environment Explorer (LADEE) mission, meteoritic influx to the lunar surface has been monitered via visual light flash observations from only very large impactors (>1 kg) striking the lunar surface [79]. Additionally, two instruments in the Apollo Lunar Surface Experiments Package (ALSEP) were capable of monitoring influx: 1) the Apollo lunar seismic station, which operated from 1969 to 1977 and had an estimated mass sensitivity of 10^{-1} to 10^{3} kg [64], and 2) the Lunar Ejecta and Meteorites Experiment (LEAM), designed to monitor the interplanetary and interstellar dust flux and the secondary particles created due to their impacts [6]. However, interpretation of this instrument's data still remains controversial [36].

The Moon acts as a large area dust detector, amplifying the amount of material impacting the surface by ejecting a factor of approximately 1000 times more mass in outgoing exospheric solid ejecta [42]. Measuring this solid ejecta kicked up into the lunar exosphere from impacting meteoroids provides a new window into the meteoroid environment at 1 AU. This environment is broken up into 2 distinct groups, the meteoroid streams and the sporadic background, described below.

1.2.1 Meteoroid Streams

The dust environment at 1 AU is dominated by grains shed from asteroids and comets mainly within the orbit of Jupiter. This includes all sources named in the previous section with the exception of EKB grains, which are largely ejected from the solar system by Jupiter during their migration towards the Sun [38].

When grains are shed, their initial orbital elements are similar to their parent body's. In addition to the gravitational forces by the Sun and the planets, the dynamics of a small dust particle is influenced by additional forces that are size-dependent, including solar wind and Poynting-Robertson drags, radiation pressure, and the Lorentz force [38]. The combination of these forces causes the ejected grains to decouple from their parent bodies and follow divergent trajectories over time. However, large enough (radii > 100 μm) grains preferentially disperse along the trajectory of their parent body, and may fill its entire orbital loop to form a tube of material [25]. Once the orbit of a source body has been filled out, it becomes a potential meteor stream. If Earth's orbit intersects the ascending or descending node of this tube, it leads to a meteor shower and is named according to the constellation in the apparent direction or radiant of the shower.

For streams of cometary origin, the cross sectional area of a given stream is determined by where along the orbit the material was ejected by the comet. Ejected grains have an ejecta velocity approximately proportional to $d^{-9/8}$ [82] where d is heliocentric distance. From this simple dependence, material ejected at perihelion will spread away from its parent body more rapidly than material ejected near apohelion, as grains ejected at apohelion have comparatively lower relative velocities to their parent bodies than grains ejected at perihelion. Hence, the dense, central region of any meteoroid tube originates from material ejected near apohelion. The timescales for a trajectory to fill in can vary depending on many factors. For example, the Geminids meteor stream filled in its trajectory on timescales of a few to 1000's of years [25]. Figure 1.1 shows a modeled version of the Geminids meteor stream's tubelike structure.

The first documented analysis of a meteor in scientific literature was in 1862 [63]; currently

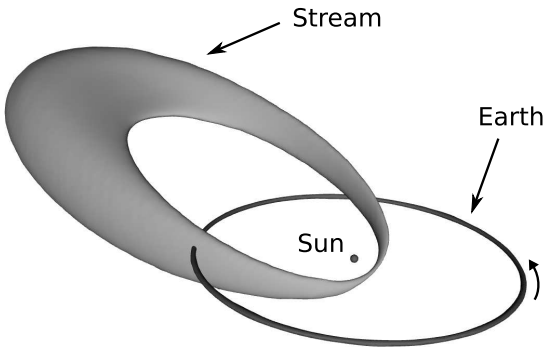

Figure 1.1: The Geminids meteor stream shown as a surface [4].

there are hundreds of documented meteor showers. Amongst them, the Geminids produces one of the strongest responses at Earth, generating approximately 100 times more visual meteors per unit time than the sporadic background [24, 48, 58]. The evolution of this stream is dominated by gravitational perturbations, where an Earth observed maximum flux occurred around 1965 [24]. The Geminids would have produced meteor showers on Venus 500 years ago, when the descending node of the mean stream intersected the Venetian orbit.

1.2.2 The Sporadic Background

Smaller grains that are more susceptive to non-gravitational perturbations disperse, and follow orbits that rapidly diverge from their parent body, forming the 'sporadic background.' The sporadic background has its own structure and is organized by various radiant groupings: a) the helion/anti-helion (HE/AH); b) apex/anti-apex (AP/AA); and c) the northern/southern toroidal (NT/ST) sources [47]. Figure 1.2 shows activity contours for a selection of these sources in the ecliptic frame centered on Earth.

In the ecliptic plane, the three dominant sources are the HE, AP, & AH. The HE & AH sources are due to grains with a higher eccentricity than the Earth on prograde orbits, either having just passed their perihelion and moving away from the Sun (HE), hence hitting the Earth from the sunward direction, or returning towards the Sun (AH), impacting the Earth from the anti-

sunward direction. The AP source is observed to have large impact velocities and are most likely due to retrograde particles impacting the Earth in its apex direction. Therefore, the distribution of impactors to the Earth-Moon system is azimuthally symmetric, and varies as a function of local time.

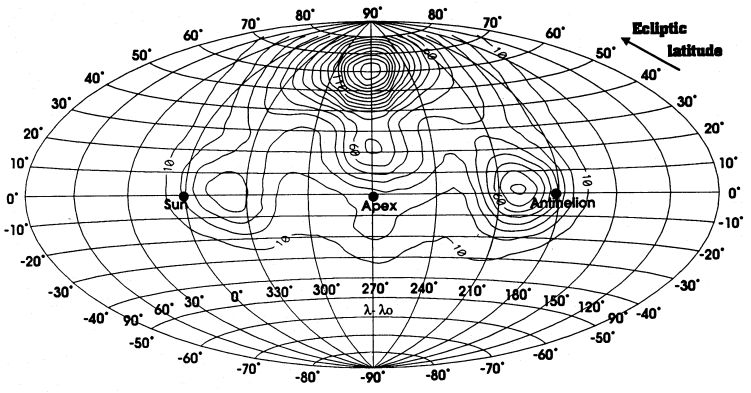

Figure 1.2: Activity contours from the Harvard radio surveys, showing the Helion (labeled 'Sun'), Anti-Helion, and Apex sources [47]. Apex points in the direction of Earth's orbital motion about the Sun.

The relative contributions from each source vary as a function of solar longitude [13]. Solar longitude, λ, is the longitude of the Sun with respect to the Earth in the J2000 reference frame. Solar longitude is used preferentially over the day of year (DOY) to identify features in meteoroid fluxes as the DOY is subject to the error induced by Earth not orbiting the Sun in exactly 365 days. 1 day is approximately equal to 1.02° λ. The variation of the sporadic background fluxes influences the spatial and temporal distribution of ejecta at the Moon. In addition to meteoroid bombardment, an additional process has also been suggested to mobilize small grains on the lunar surface.

1.2.3 Electrostatically Lofted Dust

Electrostatic dust mobilization on the lunar surface has remained a controversial topic since the Apollo era. In situ [6, 33, 70, 73] as well as remote sensing observations [23, 27, 28, 59] have potentially indicated the efficient lofting of charged dust particles near the lunar terminators. For

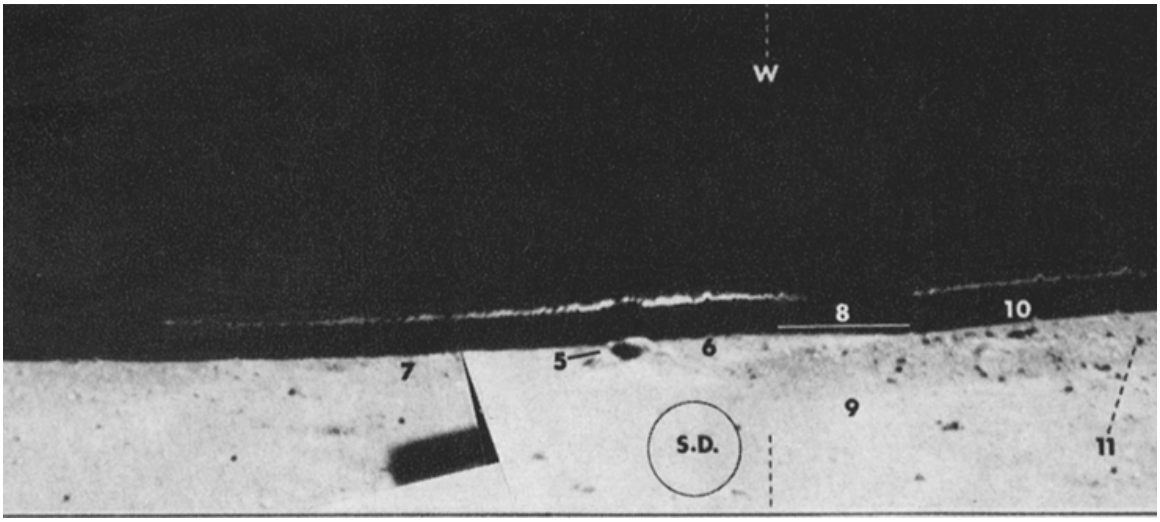

Figure 1.3: Surveyor 7 image showing horizon glow just after sunset. The sunlit foreground has been superimposed to show the surface features of the Moon relative to the dust cloud [17].

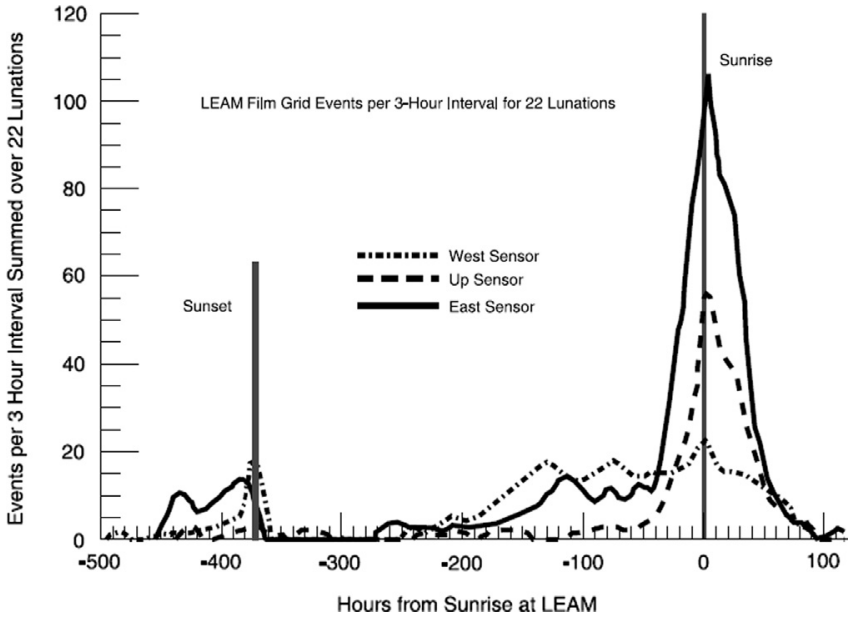

Figure 1.4: Number of events recorded by the LEAM sensors, showing the lunar sunrise and sunset enhancements [33].

example, in images taken just after sunset by the Surveyors 5, 6, and 7 cameras, a horizon glow was observed due west [17, 70]. This glow, shown in Figure 1.3, has been interpreted as forward scattered light from a cloud of dust particles levitating less than 1 meter above the surface with particle radii on the order of 5 μm [70]. However, as of yet, no mechanism capable of generating sufficiently large electric fields or dust grain charges to levitate such heavy particles has been identified. LEAM registered a multitude of unexpected hits during lunar sunrise and sunset, possibly caused by slow moving and highly charged dust grains transported across the lunar surface [5, 33], shown in Figure 1.4.

High altitude observations also indicated the existence of lofted dust at tens of km above the surface. The first high altitude, remote sensing optical observations were made during the Apollo 15-17 missions, which took a series of calibrated images to analyze the zodiacal light and the solar corona. Some of these images indicated an excess brightness that has been interpreted as forward scattered light from small grains with characteristic radii $a \simeq 0.1$ μm lofted over the terminator regions of the Moon by electrostatic effects. The density of such a dust population was first calculated to be on the order of 10^4 m^{-3} near the surface using Apollo data [28, 59]. Recent remote sensing surveys by Clementine [27] and LRO/LAMP [23] have significantly lowered the upper limit of the lofted dust density to $\sim$1 m^{-3} near the surface.

1.3 Scientific Motivation and Thesis Outline

The characteristics of the lunar dust environment until recently remained considerably unconstrained. The investigation of this environment is motivated by the need to improve our understanding of the basic impact ejecta physics at the lunar surface, to develop the ability to use the Moon or any airless body as a large meteoroid detector, and to characterize the hazards for future human and robotic missions to airless bodies. The Moon is continually exposed to meteoroid bombardment; understanding its environment sheds light on the dust environment of other airless bodies throughout the solar system such as Mercury, Mars' moons Phobos and Deimos, asteroids, and most of the outer planets' moons. This thesis is organized into three main sections:

A) **Description of the LDEX instrument.** LDEX was the first in-situ dust detector to characterize the lunar dust exosphere and the analysis of its measurements make up the results of this thesis. In Chapter 2, we describe its capabilities and how it is suited to measure the lunar dust cloud.

B) **The lunar dust cloud.** Three chapters are devoted to this topic. In Chapter 3, we describe the global characteristics of the lunar dust cloud due to the influx of IDPs from the sporadic background. The lunar dust cloud is found to be asymmetric, having a peak density in the lunar apex direction about the Sun, with a slight cant towards the sunward direction. Variations of this cloud over the period of a month to a year are found in the data and suggest the cloud waxes and wanes with the lunar phase. In Chapter 4, we descibe the Moon's response to meteor showers, which temporarily enhance the dust cloud density locally for a period of a few days. Here, we find the Moon is very sensitive to changes in IDP influx and are able to accurately determine the radiant for the Geminids meteoroid shower by analyzing groupings of particle detections. In Chapter 5, we focus on single ejecta plume detections and find the plumes LDEX encountered to be narrower than those suggested in previous literature. Each individual impact LDEX detects is part of an impact ejecta plume. By understanding how an individual plume evolves in time and how it is detected by LDEX, we can tie individual plume measurements to our measurements of the permanent dust cloud, which is sustained by the constant generation of plumes.

C) **Electrostatically lofted dust.** Separate from the permanent and global lunar dust cloud sustained by the bombardment of IDPs and subsequent impact ejecta plume generation, an additional population of dust has been suggested to exist at the Moon. Chapter 6 describes the LDEX measurements which were tailored to search for such a population. Analysis of the LDEX data indicates there is no evidence for the existence of this putative population and puts an upper limit on the density of such grains of 100 m^{-3} for altitudes above 3 km.

Chapter 2

The Lunar Dust Experiment

The results in this thesis are derived from measurements taken by the Lunar Dust Experiment (LDEX). In this chapter, we describe LDEX. Section 2.1 gives a brief overview of the LADEE mission LDEX flew on. Section 2.2 gives a description of the LDEX instrument. Section 2.3 discusses LDEX's detection modes.

2.1 LADEE Mission Overview

The Lunar Atmosphere and Dust Environment (LADEE) mission was launched on September 7, 2013. After reaching the Moon in approximately 30 days, it continued with an instrument checkout period of approximately 40 days in the altitude range of 220 - 260 km. LADEE began its $\simeq$150 days of science observations in the typical altitude range of 20 - 100 km, following a near-equatorial retrograde orbit, with a characteristic orbital speed of 1.67, km/s [22]. In addition to the Lunar Dust Experiment, the spacecraft carried a Neutral Mass Spectrometer [56], an Ultraviolet/Visible Spectrometer [15], and a Laser Communication Demonstration Experiment [22]. The LADEE orbit was optimized to take measurements over the lunar sunrise terminator. As such, LDEX had the most observation time in this region, as shown in Figure 2.1. The distribution of LDEX observation time in selenographic coordinates is shown in Figure 2.2.

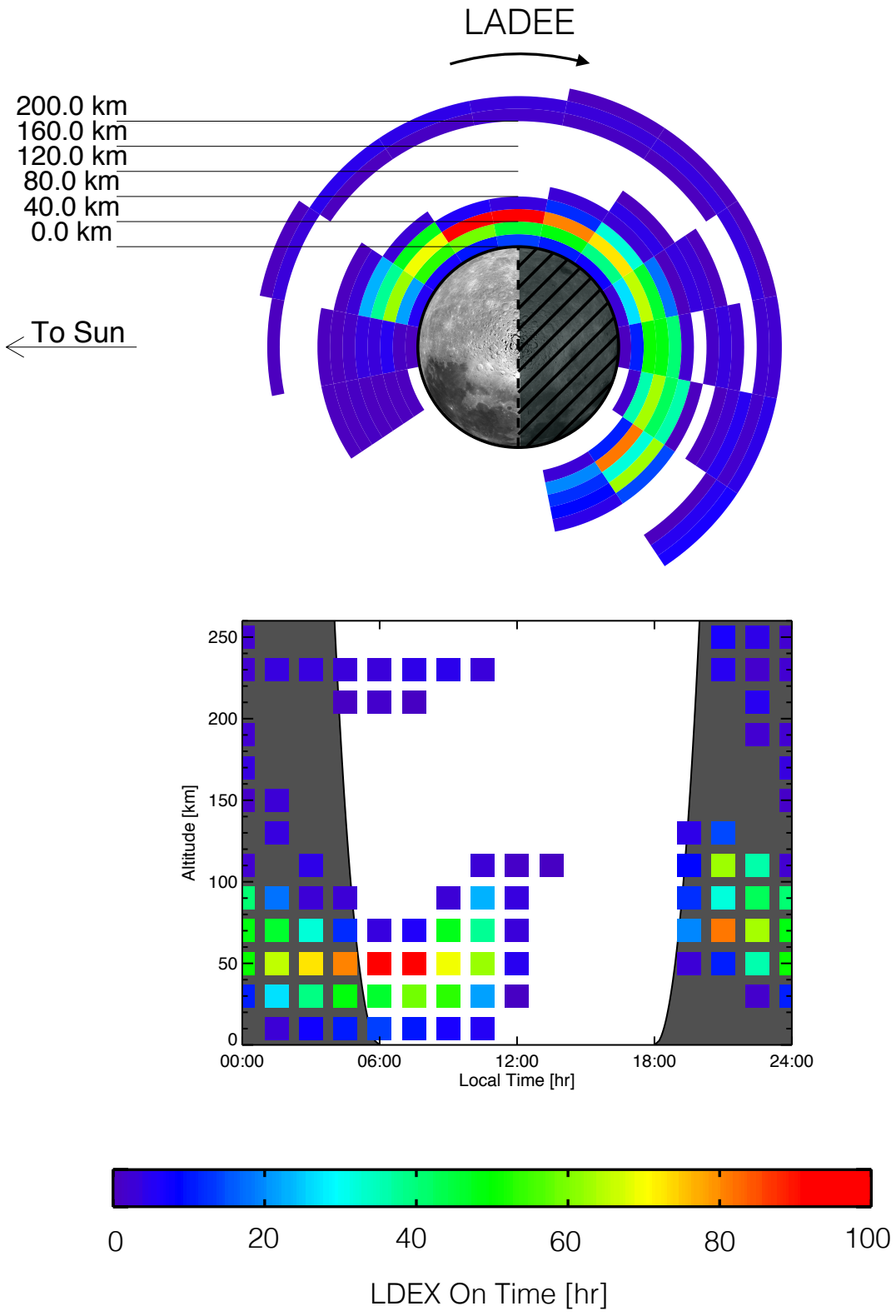

Figure 2.1: The total LDEX on time while LDEX pointed within 65° (dust FOV) from the LADEE apex throughout the mission as a function of local time and altitude.

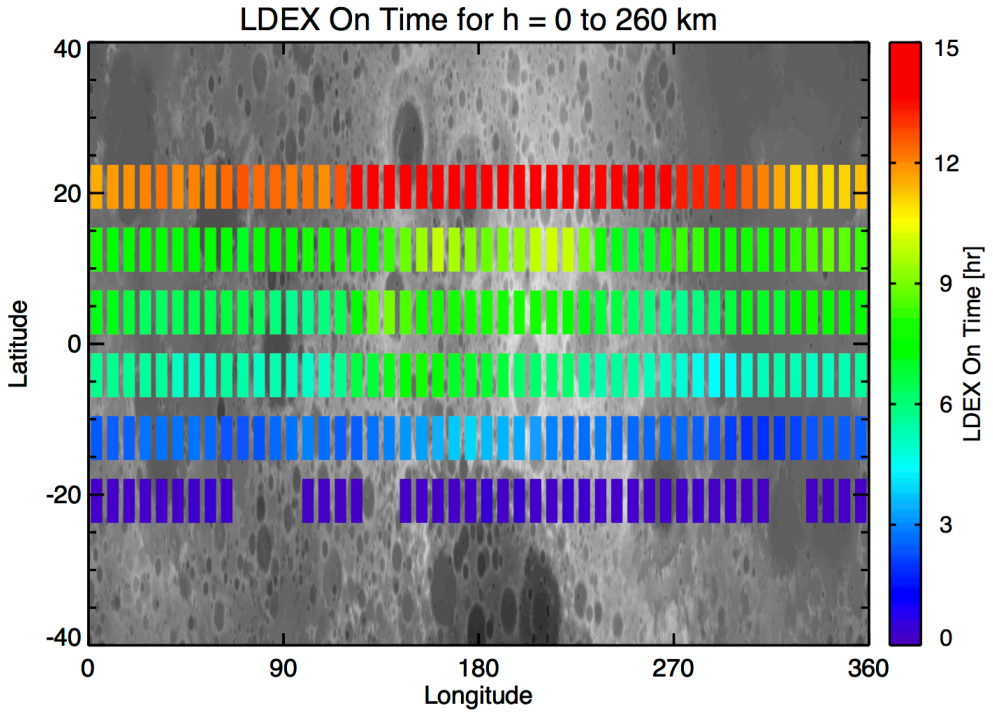

Figure 2.2: The total LDEX on time throughout the mission as a function of selenographic coordinates. The grayscale indicates the lunar terrain, taken from LOLA data [74].

2.2 Instrument Description

LDEX began its measurements on October 16, 2013 and detected a total of ≃140,000 dust hits during ≃80 days of cumulative observing time by the end of the mission on April 18, 2014. This instrument was designed to explore the ejecta cloud generated by sporadic interplanetary dust impacts, including possible intermittent density enhancements during meteoroid showers, and also to search for the putative regions with high densities of 0.1 micron-scale dust particles above the terminators. The previous attempt to observe the lunar ejecta cloud by the Munich Dust Counter onboard the HITEN satellite orbiting the Moon (February 15, 1992 to April 10, 1993) did not succeed due to its distant orbit, low sensitivity, and data archiving issues [43].

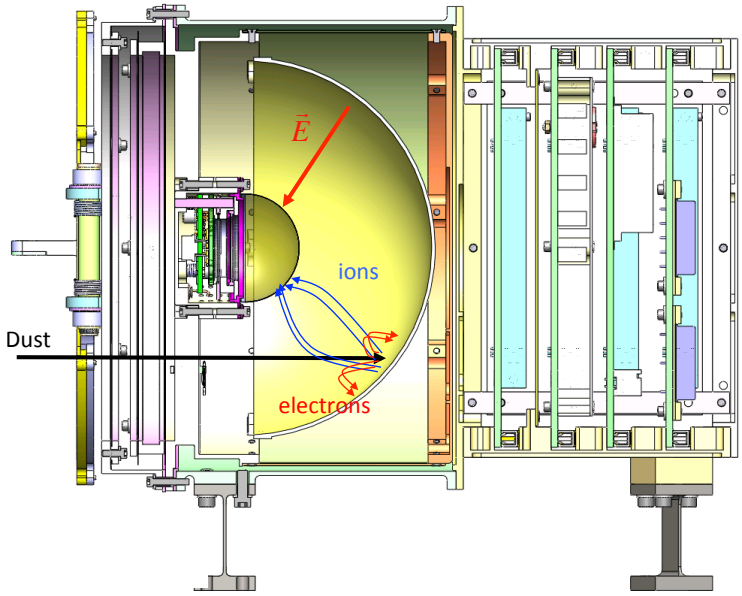

Figure 2.3: LDEX instrument schematic, illustrating a dust grain impact and the transport of electrons and ions in the instruments nominal electric field configuration.

Figure 2.3 shows a schematic of the instrument. When a dust particle with a speed greater than ≃ 1 km/s impacts LDEX's hemispherical target, it generates an impact plasma [41]. The impact ionization plasma charge (in number of electrons) produced by a dust grain (with mass m in kg) impacting LDEX is determined by the calibration of the instrument, whereby grains with

known masses and velocities were shot into LDEX, such that $q_{e^-} = (6.24 \times 10^{17}) m v^{4.76}$, where v is LADEE's orbital speed [41]. Laboratory calibrations used both iron and olivine to calibrate the impact response for lunar grains; olivine is chosen due to its similarity to lunar regolith. A negative bias potential is set up to create a radial electric field to separate the electrons and the negative ions from the positive ions. The electrons and the negative ions are collected on the target. The positive ions are detected by a microchannel plate (MCP) placed behind a focusing grid. The electric field between the target and the focusing grid in front of the MCP is periodically reversed from -200 V to +30 V, making LDEX blind to the contributions from dust impacts and low energy ions. These periods provide a self-calibration to remove the contributions from sources other than the small dust particles.

The instrument has a total sensitive area of 0.01 m^2, that gradually decreases as a function of impact angle ω to 0 for particles arriving from outside its dust field-of-view of 68° off from the normal direction (Figure 2.4). LDEX is sensitive to UV, hence its operations, in general, excluded the Sun in its optical field-of-view of ±90°.

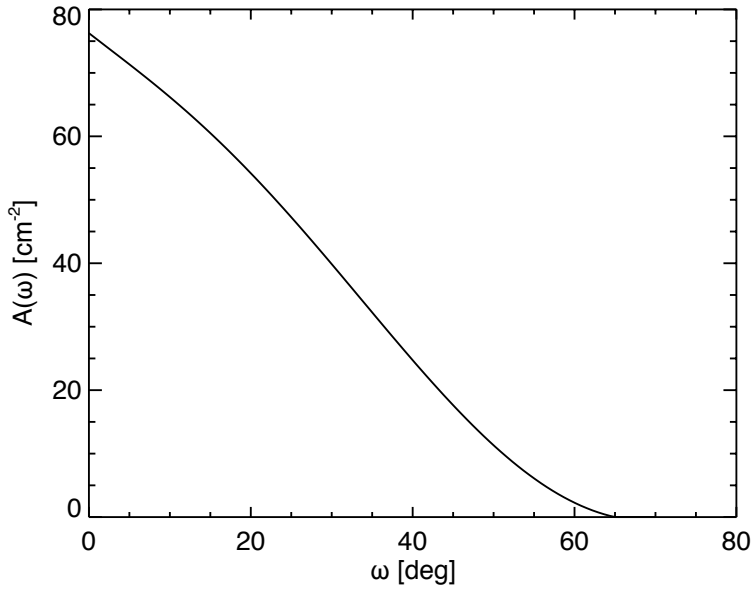

Figure 2.4: LDEX effective area as a function of impact angle ω [41].

2.3 Detection Modes

LDEX measured the dust environment via two different techniques. For large impacts ($a >$ 0.3 μm), it could determine the mass of each impacting particle, where a is the radius of the impacting dust grain. For smaller impacts, LDEX searched for a cumulative signal generated by many of these small impacts. These two detection modes are summarized in the following subsections.

2.3.1 Individual Impact Detection

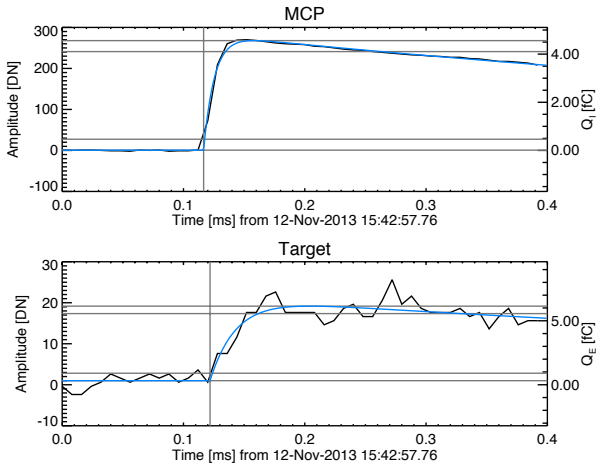

Figure 2.5: MCP and target waveforms (black lines) recorded by LDEX in orbit around the Moon on Nov. 12, 2013. Based on our laboratory calibrations, this dust particle had a mass $m = 4.5 \times 10^{-15}$ kg. The analytic fits (Eq. 2.1) to these waveforms are also shown (blue lines).

LDEX is an event-driven instrument and data acquisition is triggered by the MCP signal increasing over a threshold level of 3,000 e^-, governed by the various noise sources. This threshold level corresponds to a minimum detectable grain radius of $a \simeq 0.3$ μm. A running buffer holds the last 50 samples recorded at 8 μs intervals for both the target and the MCP signals. Once the MCP signal amplitude exceeds the threshold, the 15 samples prior to and 35 points after threshold crossing for both MCP and Target are recorded. The amplitude and shape of the waveforms are

used to estimate the mass of the dust particles. Figure 2.5 shows a typical waveform pair collected in orbit. If the incoming grains have an exceptionally large charge, they also generate an image charge on the target, which is captured in the target waveform (not depicted in Figure 2.5). Only ∼50 of the ∼140,000 dust impacts had easily identifiable image charge signals.

The MCP waveform capture can also be triggered by a number of spurious events, like cosmic ray hits or spacecraft discharging, for example. As part of the processing pipeline of downloaded data, for the identification of real dust impacts, each waveform pair is fitted by an analytical function to consistently identify their characteristics, using a non-linear least-squares fitting routine [57], given in Equation 2.1. The blue curves in Figure 2.5 show these fits.

$$
\begin{aligned}
w[t; t_0, C_0, C_1, C_2, \tau_0, \tau_1, \tau_2] = C_0 - \overbrace{\mathrm{H(t_0 - t)}\left[\mathrm{C_1 e^{-\left(\frac{t-t_0}{\tau_0}\right)^2}}\right]}^{\text{Image Charge}} \\
\underbrace{+\,\mathrm{H(t - t_0)}\left[\mathrm{C_2}\left(1 - \mathrm{e^{-\frac{t-t_0}{\tau_1}}}\right)\mathrm{e^{-\frac{t-t_0}{\tau_2}}} - \mathrm{C_1}\right]}_{\text{Impact Charge}}
\end{aligned}
\tag{2.1}
$$

The parameters in Equation 2.1 represent the initial baseline C_0, the characteristic width of the image charge signal τ_0, the time of the impact t_0, the characteristic rise time of the impact plasma generated signal τ_1 and the RC time constant of the charge sensitive amplifier τ_2. $H(x)$ is the Heaviside step function. For consistency, these analytic fits are used to identify the amplitude of the signals Q_e, and Q_I, the rise time τ_{rise}, which is customarily defined as the time the signal rises from 10% to 90% of its peak value, and the signal-to-noise ratios of a) the image-charge signal (if present) S/N_{im}, b) the target signal S/N_e, and c) the MCP signal S/N_I. The noise levels are calculated from the first eight points that also establish the baseline for each waveform. Identical fits are used for both the target and the MCP waveforms, with the only exception of setting $C_1 = 0$ for the MCP as it does not record the image charge induced by the charge a dust particle might carry before impacting the target.

The characteristics of the waveforms based on these parameters are used to classify our recorded events, Table 2.1. The parameters for this fit were driven by the characteristics a standard waveform should have without any noise. In addition to the parameters outlined above, we added a

quality parameter, $-\log_{10}\left(\frac{\sum(f-fit)^2}{amplitude^2}\right)$. Here, f is the waveform recorded by LDEX, fit is the best fit waveform, and *amplitude* is the amplitude of the given signal. This value is used to determine how similar a recorded waveform is to its actual fit, giving a shape metric. Hence, waveforms with low values of this fit quality, which would be caused by spurious signals that do not resemble a nominal waveform, are classified as noise.

Once we determine the best fit for a waveform, we classify it into one of five event classifications. The classification of the recorded events is based on the combination of satisfied conditions, as defined in Table 2.2. The lowest classification, "Noise", is given to waveforms which have no resemblance to a dust impact generated signal. "Candidate noise" is given to waveforms which at least have a decay constant consistent with the LDEX electronics. "Candidate dust impact" is given to waveforms which have an ion signal that is consistent with a dust impact, while "Dust impact" is given to waveforms where both ion and electron signals are consistent. Finally, "Dust impact with image charge", the highest level of confidence, is given to dust impacts which also have an image charge signature. We restrict our analysis to events with a classification of "Candidate dust impact" or greater throughout the analysis in this thesis.

2.3.2 Cumulative Current Detection Mode

For a 0.1 μm radius grain with a density of $\rho_d \simeq 3 \times 10^6$ kg/m^{-3} [54], the expected impact charge is $q_{e^-} \simeq 100$ electrons [19, 41]. This impact plasma charge is below LDEX's individual detection limit of 3,000 e^- and a novel method is used to search for the putative population of such small grains.

To enable the identification of regions with a high number density of particles that are too small for individual impact detection, the charge collected through the MCP is continuously integrated for periods of 0.1 s. Charges are collected while the bias voltage alternates with a cadence of 10 s. Every 9 out of 10 seconds, the bias voltage is kept at -200 V, accelerating virtually all positive ions into the MCP and a "nominal" current J_N is collected. For the last second of every 10, the "switched" current, J_S, is obtained by switching the polarity of the bias voltage to

+30V, blocking positive ions with energies less than approximately 30 eV from reaching the MCP. Since impact plasmas from dust impacts are low energy ($\simeq$ 1 eV), LDEX becomes blind to dust during these periods. This switched current gives a measure of the background contributions of photoelectrons, generated by UV photons reaching the MCP itself, and the high energy ions of solar wind origin entering LDEX, as neither of these will vary between the switched and un-switched (or nominal) periods. Hence, the difference between these two signals taken every 10 seconds yields the residual, low-energy ion current, $J = J_N - J_S$. The residual, low energy ions come from either dust impacts, J_D, the desired quantity, or from low energy ions entering LDEX, J_L.

The low energy current, J_L, LDEX measured can come from a variety of sources, including: a) back-scattered solar wind protons with initial typical energies of $>$ 100 eV [71] loosing energy inside LDEX by multiple scattering; b) sputtering the LDEX target by energetic neutral atoms [1, 72]; c) and the lunar ionosphere [67]. These currents, defined in Table 2.3, are summarized below

$$J_N = J_D + J_\nu + J_H + J_L$$

$$J_S = J_\nu + J_H$$

$$J = J_N - J_S = J_D + J_L$$

"Current" for the remainder of this thesis will refer to the residual, low-energy current, J. All impact plasma charges due to a flux of small grains to LDEX will be captured in this current if they exist. Hence, the current can be used to search for the putative population of grains with $a \simeq 0.1$ μm lofted over the sunrise terminator regions by electrostatic effects.

Figure 2.6 shows an example of the three currents, J_N, J_S, and J. It should be noted that the large majority of impacts of dust grains that are individually detectable, $a > 0.3$ μm, do not significantly contribute to any of these currents. An impact of a 0.3 μm radius grain yields approximately 3,000 e^-. These impacts occur with an average impact rate of 1 min^{-1}, which gives an average current contribution from 0.3 μm radius grains of approximately 50 e^-s^{-1}, negligibly small compared to the average value of $J \simeq 10^5$ e^-s^{-1}, measured by LDEX.

Table 2.1: Requirements on waveforms.

#	**Requirement**	**MCP**	**Target**
1	signal-to-noise	$S/N_I > 5$	$S/N_e > 3.5$
2	rise time [μs]	$20 < \tau^I_{rise} < 400$	$20 < \tau^e_{rise} < 400$
3	decay time [ms]	$0.25 < \tau^I_2 < 2$	$0.25 < \tau^e_2 < 2$
4	coincidence [μs]	$\lvert t^e_0 - t^I_0 \rvert < 50$	
5	$-\log_{10}\left(\frac{\sum(f-fit)^2}{amplitude^2}\right)$	> 1	> 0
6	image charge		$S/N_{im} > 2$

Table 2.2: Event classification. The list of requirements (1-6) are identified in Table 2.1. A ✓ indicates compliance with the MCP criteria while a ✓✓ indicates compliance with both the MCP and Target criteria. Criteria 5 is a quality of fit parameter, designed to removed waveforms that do not have a similar shape to the analytic fit. f is the 50 data points given by the LDEX collected waveform, fit is the fitted function, and *amplitude* is the amplitude of the signal.

Event	1	2	3	4	5	6
Dust impact with image charge	✓✓	✓✓	✓✓	✓✓	✓✓	✓
Dust impact	✓✓	✓✓	✓✓	✓✓	✓✓	
Candidate dust impact	✓	✓	✓		✓	
Candiate noise			✓			
Noise						

Table 2.3: Current Definitions

Current	Definition
J_N	Nominal current, taken 9 of every 10 seconds
J_S	Switched current, taken 1 of every 10 seconds
J_D	Dust current, desired science quantity
J_ν	Photoelectron current
J_H	High energy ion current ($\gtrsim$ 30 eV)
J_L	Low energy ion current ($\lesssim$ 30 eV)
J	Residual, low energy current

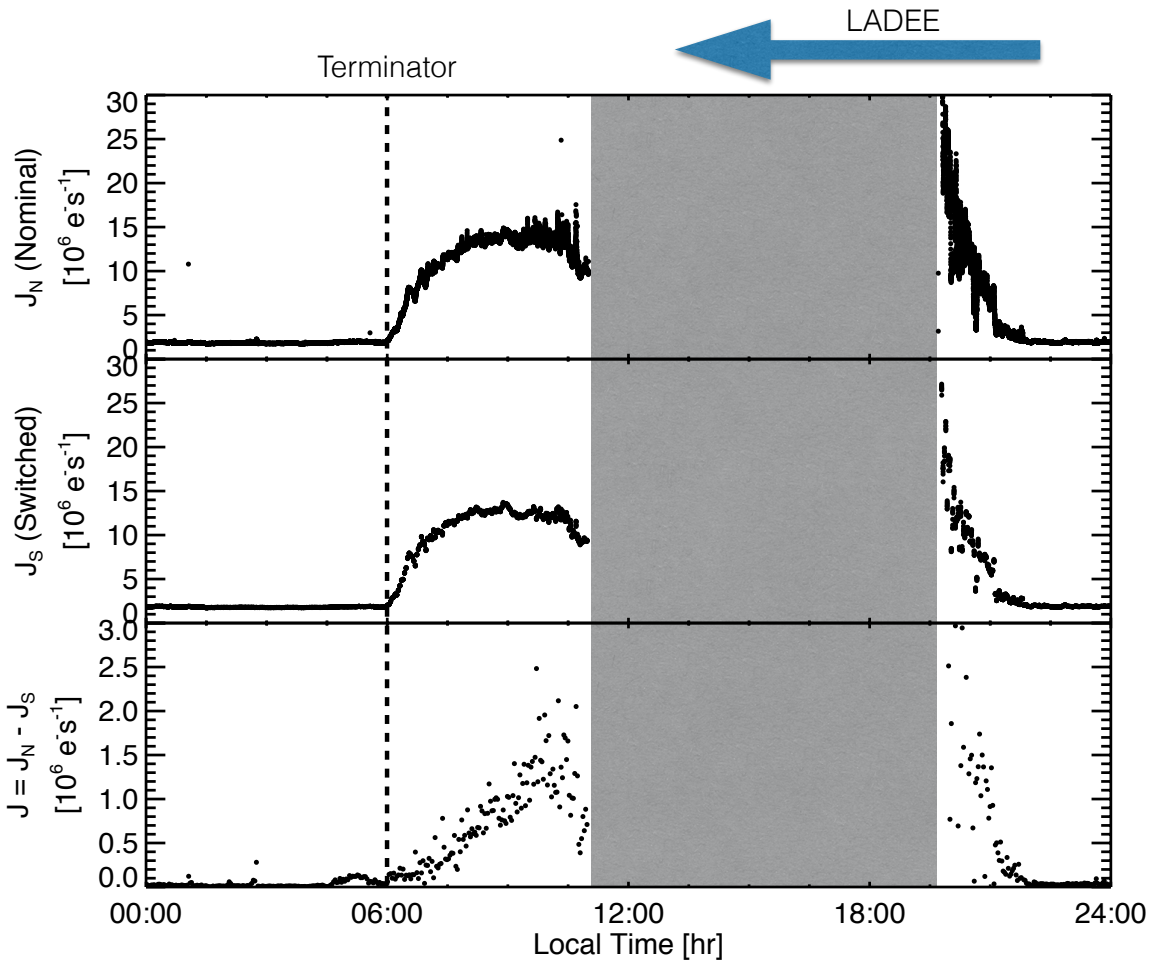

Figure 2.6: Top panel: J_N, or the nominal current, taken 9 of every 10 seconds at a bias potential of -200 V. This measurement captures all possible ion sources. Middle panel: J_S, or the switched current, taken 1 of every 10 seconds at a bias potential of 30V. This measurement captures only the high-energy ion sources. The bottom panel shows the "current", $J = J_N - J_S$. The gray bar indicates when LDEX was off during this orbit and the vertical dotted line denotes the terminator crossing.

Chapter 3

The Lunar Dust Exosphere

The previous chapter described the LADEE mission and LDEX's detector design and operations. LDEX was designed to characterize the lunar dust cloud and in this chapter, we focus on the bulk characteristics of this cloud. Section 3.1 describes the impact rates and mass distribution of particles detected by LDEX. Section 3.2 describes the lunar dust cloud density derived from these measurements and Section 3.3 compares these measurements with model predictions. Section 3.4 describes the annual variability and synodic modulation of the meteoroid flux to the Moon.

3.1 Impact Rates and Mass Distribution

When pointed in the direction of motion of the spacecraft, LDEX recorded average impact rates of $\simeq 1$ and $\simeq 0.1$ hit/minute of particles with impact charges of $q \geq 0.3$ and $q \geq 4$ fC, corresponding to particles with radii of $a \gtrsim 0.3$ and $a \gtrsim 0.7\mu$m, respectively. The impact rate measured by LDEX throughout the entire mission is shown in Figure 3.1. A few of the catalogued meteor showers, most notably the Geminids, generated enhanced impact rates and will be discussed in the following chapter.

The distribution of the detected impact charges remained largely independent of altitude, and throughout the entire mission it closely followed a power law $p_q(q) \propto q^{-(1+\alpha)}$ (Figure 3.2). This alone indicates that the initial mass distribution of the ejecta particles is, to a good approximation, independent of their initial speed and angular distributions, and the number of ejecta particles generated on the surface per unit time with mass $> m$ follows a power law $N^+(> m) \propto m^{-\alpha}$ [42].

The LDEX measurements indicate $\alpha \simeq 0.9$, surprisingly close to the value $\alpha_G = 0.8$ suggested by the Galileo mission at the icy moons of Jupiter [50], and to laboratory experimental results of ejecta production from impacts [9]. The derived ejecta size distribution also represents the size distribution of the smallest lunar fines on the surface as most ejecta particles return to the Moon and comprise the regolith itself, unless these small particles efficiently conglomerate on the lunar surface into larger particles.

3.2 Density Distribution

The characteristic velocities of dust particles in the cloud are on the order of a few 100's of m/s, which is small compared to the typical spacecraft speeds of 1.67 km/s. Hence, with the knowledge of the spacecraft orbit and attitude, impact rates can be directly turned into particle densities n as functions of time and position. The desired quantity is the number density of grains between mass range m and $m + dm$, velocity range v and $v + dv$, and altitude range h and $h + dh$, given by $n(m_d, v, h)$ where $\hat{\mathbf{n}}$ is along the LDEX's boresight. The number of grains LDEX detects in a time interval dt is

$$dN(m_d, v, h, t) = n(m_d, v, h, t)\mathbf{A}\big((\mathbf{v_{sc}} - \mathbf{v_d}) \cdot \hat{\mathbf{n}}, t\big) \cdot (\mathbf{v_{sc}} - \mathbf{v_d})\ dt \tag{3.1}$$

assuming the number density does not vary with time and that all grains are impacting LDEX with a velocity vector parallel to the area spacecraft velocity vector $\mathbf{v_{sc}}$, the total number of impacts over a time interval $[t_1, t_2]$ is found by integration,

$$\begin{aligned} N(m_d, v, h) &= \int_{t_1}^{t_2} dN(m_d, v, h, t) && (3.2)\\ &= \int_{t_1}^{t_2} n(m_d, v, h) A\big((\mathbf{v_{sc}} - \mathbf{v_d}) \cdot \hat{\mathbf{n}}, t\big) |\mathbf{v_{sc}} - \mathbf{v_d}|\ dt && (3.3)\\ &= n(m_d, v, h) \int_{t_1}^{t_2} A\big((\mathbf{v_{sc}} - \mathbf{v_d}) \cdot \hat{\mathbf{n}}, t\big) |\mathbf{v_{sc}} - \mathbf{v_d}|\ dt && (3.4) \end{aligned}$$

The number density can be determined, with the error from counting statistics $E = n/\sqrt{N}$, as

$$n(m_d, v, h) = \frac{N(m_d, v, h)}{\int_{t_1}^{t_2} A\big((\mathbf{v_{sc}} - \mathbf{v_d}) \cdot \hat{\mathbf{n}}, t\big) |\mathbf{v_{sc}} - \mathbf{v_d}|\ dt} \tag{3.5}$$

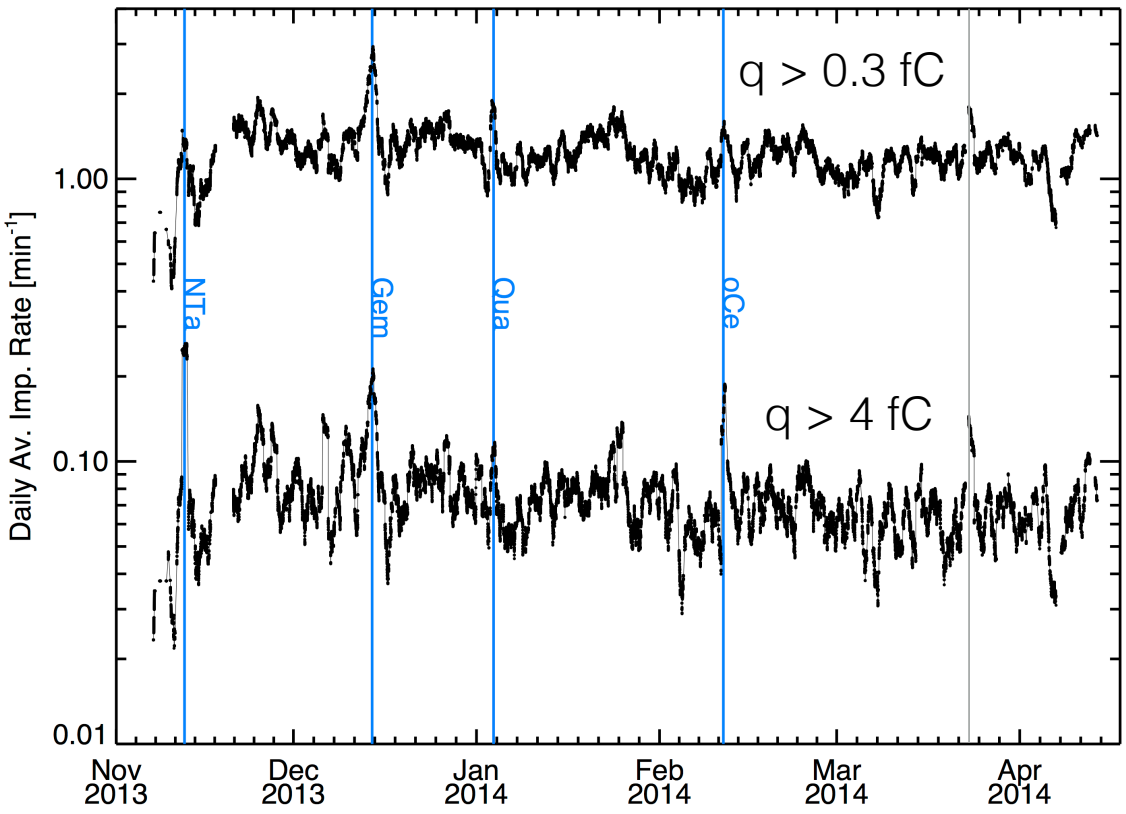

Figure 3.1: Impact rates throughout the mission. The daily running average of impacts per minute of particles that generated an impact charge of $q \geq 0.3$ fC (radius $a \gtrsim 0.3$ μm) and $q \geq 4$ fC (radius $a \gtrsim 0.7$ μm) recorded by LDEX. The initial systematic increase through November 20, 2013 is due to transitions from high-altitude checkout to the subsequent science orbits. Four of the several annual meteoroid showers generated elevated impact rates lasting several days. The labeled annual meteor showers are: Northern Taurids (NTa); Geminids (Gem); Quadrantids (Qua); Omicron Centaurids (oCe). The observed enhancement peaking on March 25, 2014 (grey vertical line) does not coincide with any of the prominent showers. During the Leonids meteor shower around November 17, 2013 the instrument remained off due to operational constraints. Based on counting statistics, the daily average impact rate of particles generating at least 0.3 fC charge is 1.25 hits/minute, hence the 1 sigma relative error is about 2%, while for particles generating an impact charge >% 4 fC the average rate is 0.08 per minute, hence the relative error is about 10%.

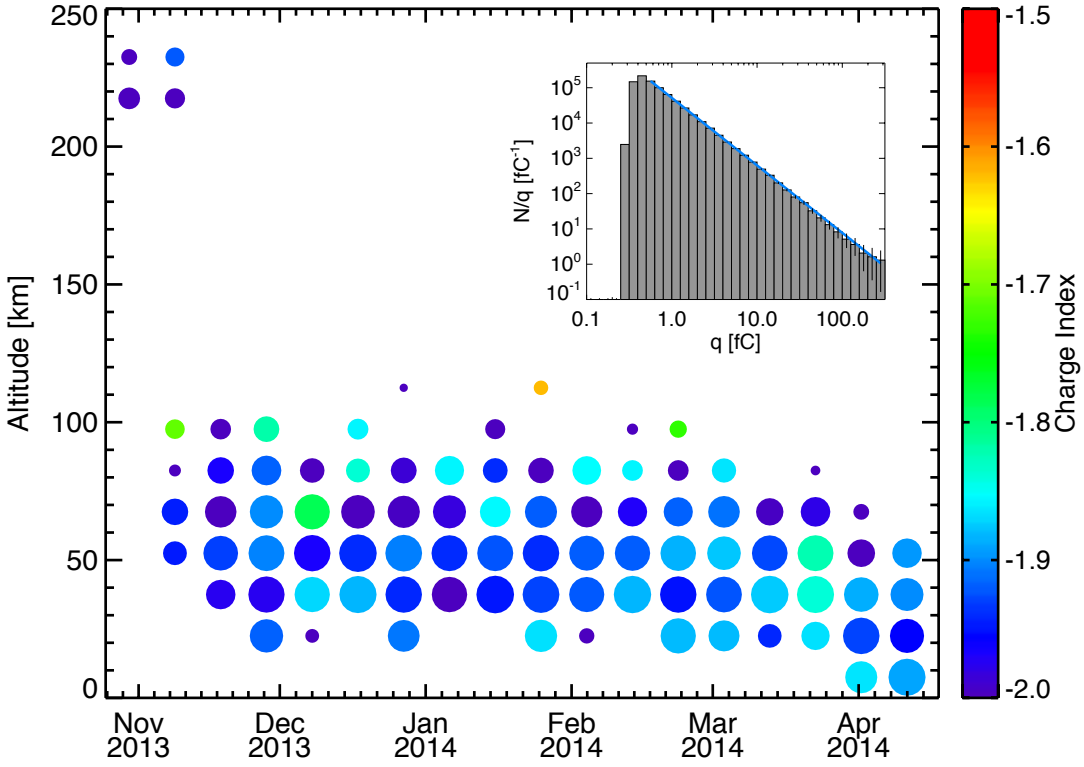

Figure 3.2: Slope of the charge and mass distribution. The exponent of the power law distributions of the impact charges $p_q(q) \propto q^{-(1+\alpha)}$ fitted to LDEX measurements as function of altitude (20 km bins) and time (5 day bins). The color indicates the value of the charge distribution index $-(1+\alpha)$, and the size of a circle is inversely proportional to its absolute uncertainty (largest circle: ± 0.1; smallest ± 0.5). The insert shows the impact charge distribution for all heights for the entire mission, resulting in a χ^2 minimalizing fit [57] of $\alpha = 0.910 \pm 0.003$.

The lunar dust density distribution as a function of altitude is shown in Figure 3.3a. The approach outlined above, with $v_d = 0$, is expected to result in a relative error $< 20\%$, based on a complete ejecta cloud model [42, 50]. Both the derived average number density as a function of height and the initial speed distribution match expectations only for altitudes $h \gtrsim 50$ km, as shown in Figure 3.3. This indicates that customary model assumptions, such as the simple power law speed distribution with a single sharp cutoff minimum speed u_0, are not applicable below certain altitudes. At higher values the speed distribution follows a simple power law [42], as predicted by existing models [50]. The average total mass of the dust ejecta cloud with $a \gtrsim 0.3$ μm is estimated to be $\simeq 120$ kg, approximately 0.5% of the neural gas atmosphere [78].

We found that the density distribution is not spherically symmetric around the Moon (Figure 3.4), exhibiting a strong enhancement near the morning terminator between 5 - 8 hour local time (LT), slightly canted toward the Sun from the direction of the motion of the Earth-Moon system about the Sun (6 LT). This is in contrast to the roughly isotropic ejecta clouds engulfing the Galilean satellites, where the vast gravitational influence of Jupiter is efficiently randomizing the orbital elements of the bombarding interplanetary dust particles [77]. The anisotropic ejecta production is consistent with existing models of the interplanetary dust distributions near the Earth combining in situ dust measurements, visible and infrared observations of the Zodiacal Cloud, as well as ground based visual and radar observations of meteors in the atmosphere [20, 60]. The dust production on the lunar surface is dominated by particles of cometary origin, as opposed to slower asteroidal dust particles following near-circular orbits as they migrate toward the Sun due to Poynting-Robertson drag [61]. Solely asteroidal meteoroids would sustain only a much weaker, more azimuthally symmetric ejecta cloud, contrary to LDEX observations [42].

3.3 Modeled dust production on the lunar surface

Figure 3.3 was generated assuming that the LT averaged ejecta cloud is spherically symmetric to determine the average properties of the cloud and allow for direct comparison with previous studies [50, 51]. Here we address the anisotropic nature of the dust influx to the lunar surface. To

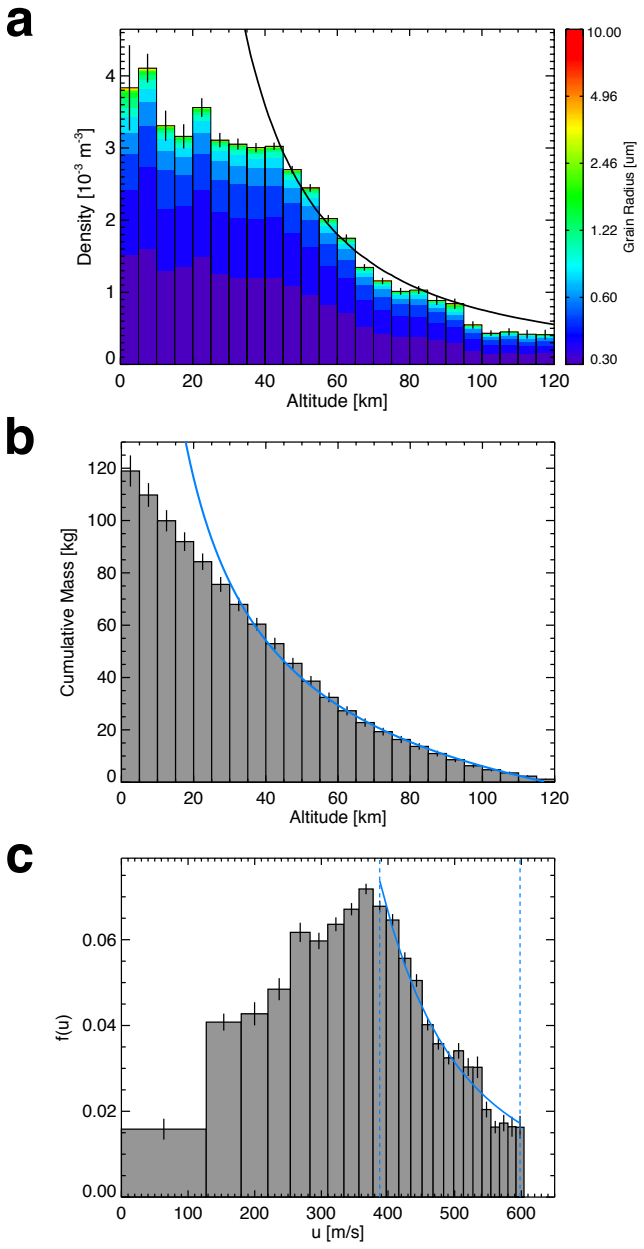

Figure 3.3: Comparison of observed and modeled cloud properties. **a,** The dust density $n(h)$ of the lunar ejecta cloud as function of altitude and size (color code). The continuous black line shows the model prediction [50] using the best fit parameters listed in [42]. The same model with different parameters, which describes a steady state dust ejecta cloud, was used to explain the Galileo Dust Detector data from the dust clouds around the Galilean moons [50]. The departure from the model prediction at altitudes below 40-50 km may be due to the discrepancy between the assumed and true velocity distributions. **b,** The cumulative dust mass in the lunar exosphere. The continuous blue line shows the ejecta model prediction [42]. **c,** The initial normalized vertical velocity distribution $f(u)$ calculated from $n(h)$ using energy conservation. The continuous line shows $f(u) \propto u^{-3.4\pm0.1}$ matched to the data at $u \geq 400$ m/s (altitude $h \simeq 50$ km). Error bars were calculated by propagating $\sqrt{N}$ error through the various calculations, where N is the number of detected dust impacts.

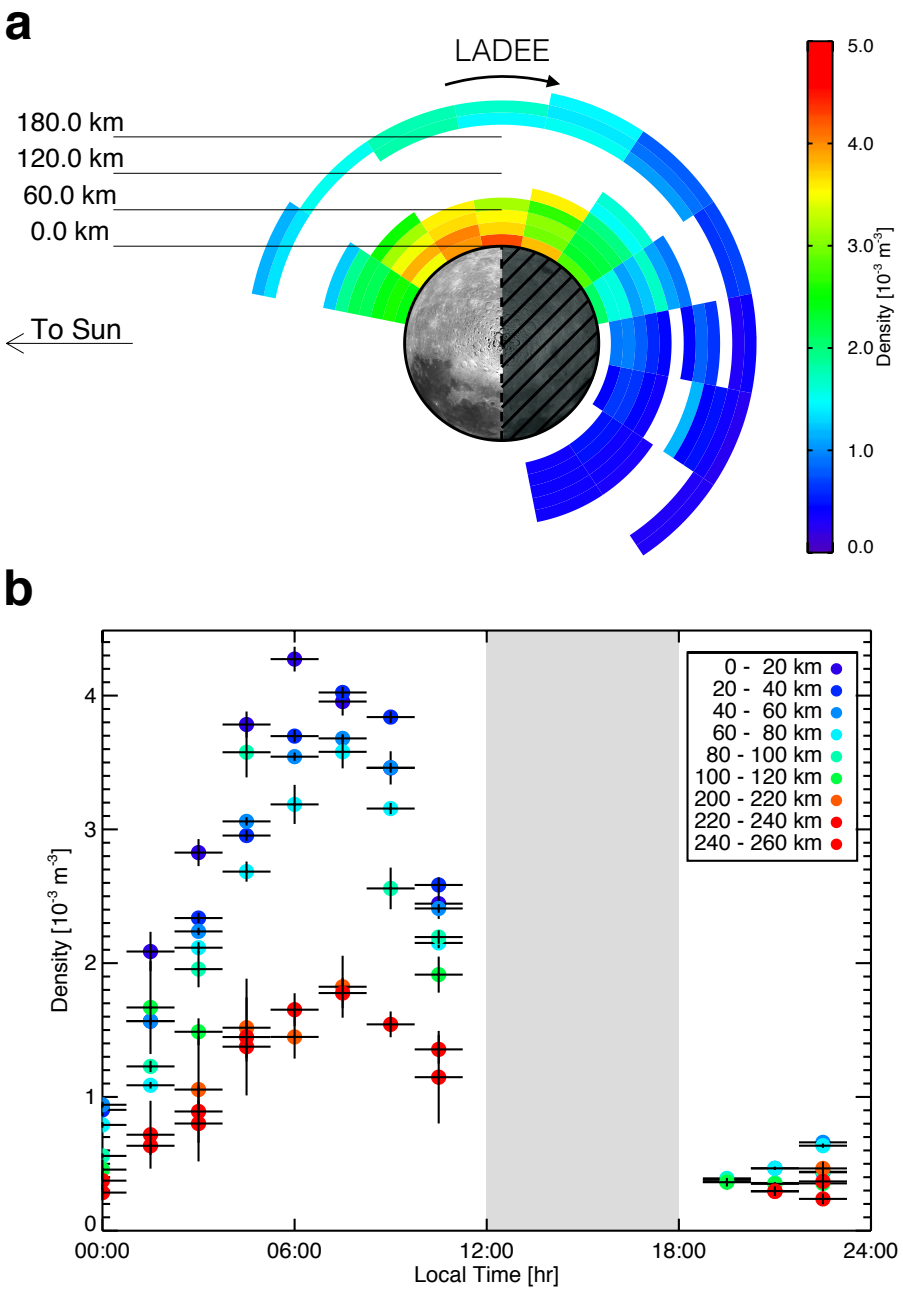

Figure 3.4: The density as a function of local time for $n(a \gtrsim 0.3\ \mu\text{m})$ at different altitude bins showing a persistent enhancement canted toward the Sun away from the direction of the orbital motion of the Earth-Moon system. While pointed near the direction of the motion of the spacecraft, LDEX did not make measurements between 12 and 18 LT. **a**, The top-down view of the dust density projected onto the lunar equatorial plane. **b**, The gray bar indicates local times LDEX did not take measurements. Error bars were calculated by propagating $\sqrt{N}$ error through the density calculation, where N is the number of detected dust impacts. White color indicates regions where LADEE did not visit or was not set up for normal operations.

this end we replace the single global dust mass production M^+ with an LT and time (t) dependent function of mass production per unit surface area $M^+(LT, t)$.

The mass flux of bombarding interplanetary dust particles with mass m and velocity v is a function of both the position on the lunar surface, and time, $F(m, v, LT, t)$. A single dust particle impacting a solid silica surface generates large number of ejecta particles with a total mass $m^+ = mY(m, v)$, with the yield given by

$$Y \simeq C m_{imp}^{\alpha} v_{imp}^{\beta} \cos^2 \varphi, \tag{3.6}$$

where $C = 30$ for a silicate surface, m_{imp} is the mass of the impacting particle in kg, v_{imp} is the velocity of the impacting particle in km/s, φ is the impact angle from the surface normal, $\alpha = 0.2$, and $\beta = 2.5$ [49, 50]. The angular dependence is derived from an experimental finding that the material excavated by impacts varies as $\cos^2 \varphi$ [26]. While this experiment [26] was performed for impacts into solid rock, which may has different impact physics compared to regolith, we still implement its results as it is the most relevant finding on the angular dependence of impact ejecta. At the Moon, $Y \approx 1000$ [42] at normal incidence.

Our detected impacts are dominated by ejecta particles generated along the ground track of the spacecraft that followed a nearly equatorial orbit. Hence, it is convenient to track the position on the lunar surface in local time (LT), with LT = 0, 6, 12, and 18 marking midnight, the dawn terminator, sub-solar point, and the dusk terminator, respectively. The mass production rate per surface area as function of LT is found by integrating the product of the interplanetary dust flux and the yield Y around the lunar equator

$$M^+(LT, t) = \int \int F(m, v, LT, t) Y(m, v) dm dv. \tag{3.7}$$

We evaluated Equation 3.7 using both NASA's Meteoroid Environment Model (MEM) [60] and ESA's Interplanetary Meteoroid Environment Model (IMEM) [20] models that agree well near 1 AU. The flux F and the predicted mass production rates $M^+(LT, t)$ are shown in Figures 3.5 & 3.6, and are consistent with the apex/anti-apex asymmetry in the dust ejecta cloud observed by

LDEX, however the location of the peak density is not always in agreement. We note that the meteoroid population still remains one of the most uncertain space environment components [21].

To understand effects of the various meteoroid sources on the ejecta cloud, we follow another line of study separate from the inherent complexities in MEM & IMEM. The mass production per unit surface has the form $M^+ = (F_{\rm imp}\cos\varphi)m_{\rm imp}Y$, where $F_{\rm imp}$ is the number flux of the impactors with characteristic mass $m_{\rm imp}$, $\cos\varphi$ is the projection area factor, and Y is given in Equation 3.6. The total mass production as a function of angle φ from apex for a finite number of discrete meteoroid sources is,

$$M^+(\varphi) = C\sum_s \underbrace{F_s m_s^{\alpha+1} v_s^{\beta}}_{M_s^+} \cos^3(\varphi-\varphi_s)\Theta(\varphi_s-\pi/2), \tag{3.8}$$

where s represents the various sources, φ_s is the characteristic angle from apex for each source radiant, and Θ is the Heaviside function, as each source only contributes to ejecta production on the hemisphere it impacts.

The dominant sources which impact the Moon in the equatorial plane of LADEE's orbit are the HE, AP, & AH sources. We therefore use these three sources to compare the predicted M^+ to LDEX observed densities. For the characteristic angles, we use $\varphi_{\rm HE} = 65^\circ$, $\varphi_{\rm AP} = 0$, and $\varphi_{\rm AH} = -65^\circ$ [12]. As M^+ gives the total amount of material ejected from the lunar surface, it is proportional to the dust cloud density. Since LDEX measured a relatively flat density distribution up to altitudes of 40 km [42], we use the dust column density in the altitude range of 0-40 km to gauge M^+.

From late October, 2013 to the end of December, 2013, the Moon experienced nearly continuous bombardment by meteoroid streams [8, 58], which mask the contributions of the various sporadic sources to the cloud distribution. Hence, we focus on the quiescent period, from January, 2014 to the end of mission in April, 2014, to investigate the response of the Moon to the sporadic background. We used χ^2 minimization to find the relative M_s^+ contributions of each sporadic source in Equation 3.8 that best match the shape of the observed cloud (Figure 3.7). For the average cloud, the relative contributions are found to be $M_s^+ = (0.37, 0.45, 0.18) \pm 0.01$ for the HE,

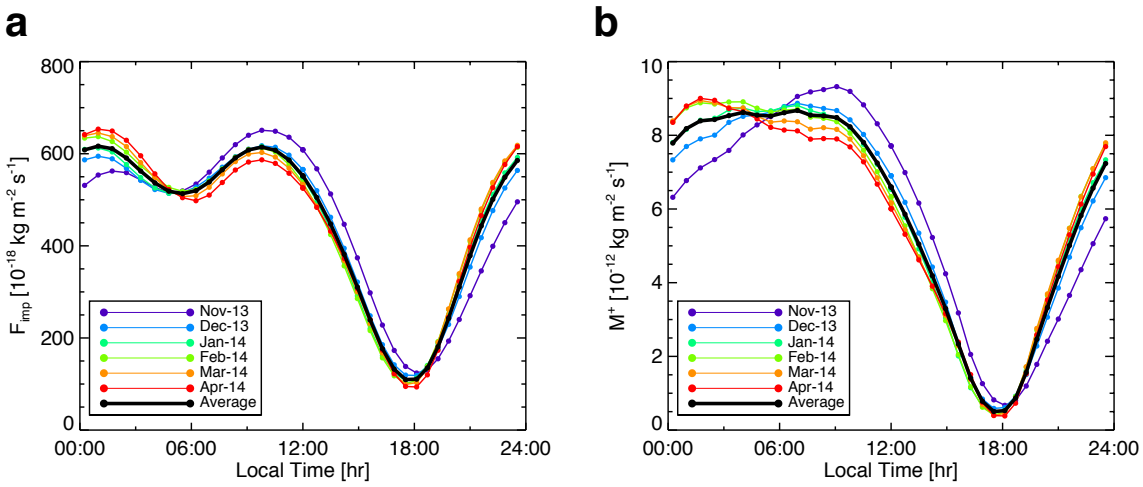

Figure 3.5: Modeled flux and mass production in the lunar equatorial plane. **a,** The calculated flux of interplanetary dust particles reaching the lunar equatorial region as function of LT and t (color coded for monthly averages), and **b,** the mass production rate (Equation 3.7) using a model for the spatial and velocity distributions of interplanetary dust particles near the Earth [60], consistent with the observed asymmetric dust cloud.

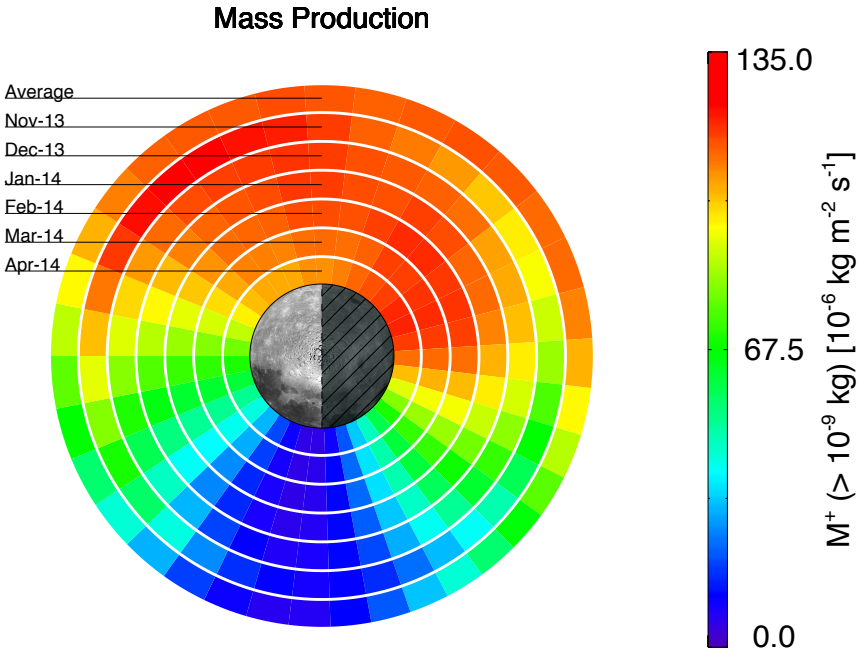

Figure 3.6: Modeled flux and mass production in the lunar equatorial plane. Each ring shows the average equatorial dust mass production rate M^+ predicted by LMEM for the months of November 2013 to April 2014.

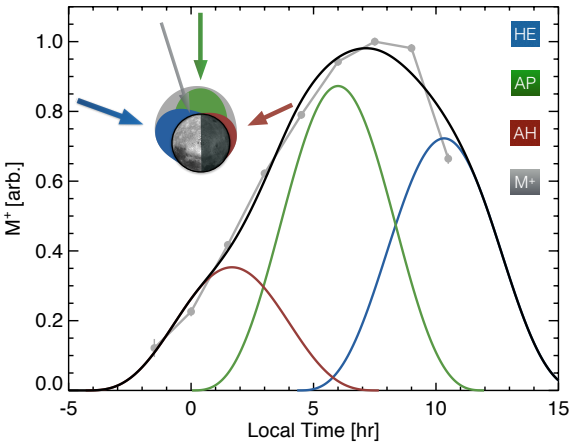

Figure 3.7: The best total M^+ fit (black) for the HE (blue), AP (green), & AH (red) sources to the LDEX data (gray) from January to April 2014. The schematic in the top left indicates the directions of the various sources and the apparent peak M^+ direction. The LDEX observed density is normalized to unity.

AP, & AH sources respectively, with the normalization $\sum M_s^+ = 1$. Errors are calculated via the χ^2 minimization used in the fitting routine [57].

The HE source is comprised of particles that just passed their perihelion and cross 1 AU moving out from the Sun [45, 47, 10, 62, 44]. On their return towards the Sun, they form the AH source. The HE and AH sources are comprised of the same material and originate from the same source bodies, therefore, $v_{\mathrm{HE}} \approx v_{\mathrm{AH}}$ and $m_{\mathrm{HE}} \approx m_{\mathrm{AH}}$. With this constraint, the ratio between the HE and AH mass production values directly yields their flux ratio and we find $F_{\mathrm{HE}}/F_{\mathrm{AH}} = M^+_{\mathrm{HE}}/M^+_{\mathrm{AH}} \approx 2.1 \pm 0.2$ on average, from January to April 2014.

3.4 Annual Variation and Synodic Modulation

From January to April, 2014, the cloud structure was observed to vary (Figure 3.8). The changes in the the observed densities are caused by changes in the relative contributions of the three dominant sources. To investigate this temporal dependence, we find the best fit for each M_s^+ throughout 2014 in a sliding window of 30 days (Figure 3.9). The flux ratio $F_{\mathrm{HE}}/F_{\mathrm{AH}}$ decreases by a factor of two from ~ 3 at the beginning of 2014 to ~ 1.5 in mid-April. Ground based measurements

indicate a similar factor of two decrease in this ratio, however for a smaller range of ~ 1.7 to 1.0 [12].

In addition to its sensitivity to the variation of each source flux, the lunar ejecta cloud density is also sensitive to changes in the impact velocity of incoming meteoroids, since $M^+ \propto v_{\text{imp}}^{\beta}$. The impact velocity of each source is modulated by the Moon's 1 km/s orbital velocity around the Earth, hence $v_s(\theta) = v_{s,av} + \cos(\theta - \varphi_s)$, where θ is the lunar phase and has a value of 0° at full moon. Hence, the mass production of each source peaks at $\theta_{s,\text{peak}} = \varphi_s$ and oscillates throughout the Moon's synodic period. Since the AP and HE sources dominate the mass production over the AH source, the lunar dust cloud is expected to peak during the waning gibbous phase between $\theta_{\text{AP,peak}} = 0°$ and $\theta_{\text{HE,peak}} = 65°$.

Figure 3.10 shows the observed lunar dust cloud distribution for lunar phases in increments of 45°. Each depicted lunar phase is averaged from 1-Jan-2014 to 18-Apr-2014. The lunar dust cloud is found to wax and wane with lunar phase as expected, peaking when the Moon is in its waning gibbous phase. The phase of this peak further validates the conclusion that the HE source dominates over the AH source for the period of measurement.

We are able to estimate the HE/AH flux ratio as a function of time, noting a factor of 1.5-2 discrepancy from radar based observations. Meteoroids impacting the lunar surface generate ejecta in a mechanism entirely different than how they ablate and ionize in the Earth's atmosphere. Detecting the signatures of primary impactors in each scenario relies on significantly different parameters. The discrepancy in $F_{\text{HE}}/F_{\text{AH}}$ between this method and radar based methods is most likely be due to the difference between these two very different mechanisms.

The high fidelity of the fit for just 3 sources matches the cloud profile quite accurately and suggests the ejecta production at the Moon is dominantly governed by these sources. This observation further strengthens the finding that the various strengths of the HE, AP, & AH sources change throughout the year, consistent with previous ground based radar studies [66, 12]. The annual variation of the HE & AH sources has been suggested to arise due to these sources having a small number of parent bodies, leading to an asymmetric orbital distribution [66, 12, 10, 83].

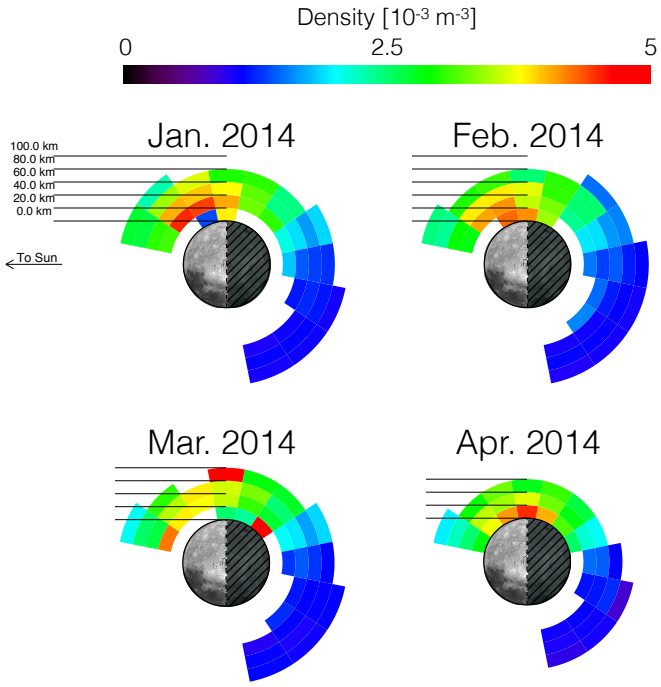

Figure 3.8: The average cloud density for each calendar month LADEE was operational in 2014. Each color ring corresponds to the density every 20 km.

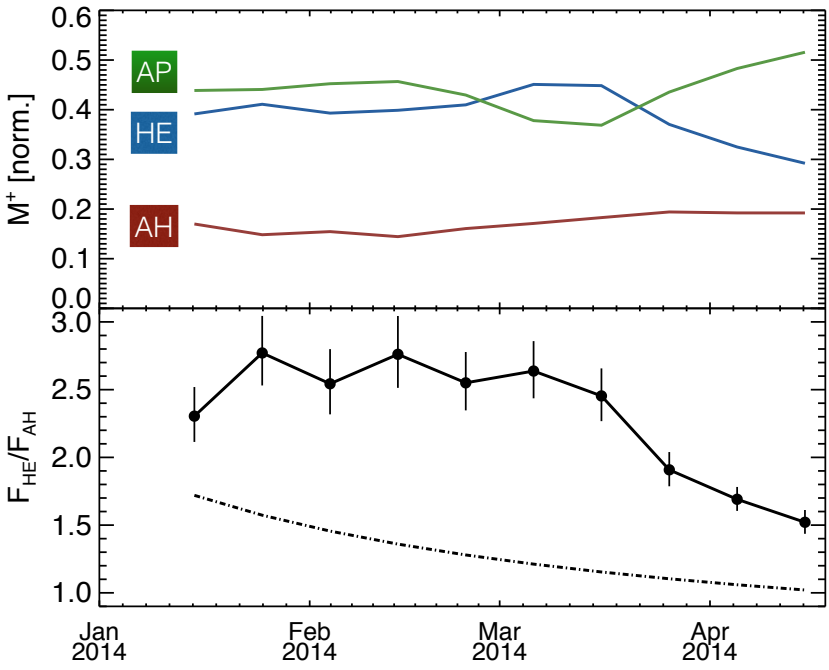

Figure 3.9: Top: The best fit M_s^+ for the HE (blue), AP (green), & AH (red) sources. Bottom: The flux ratio between the HE and AH sources from LDEX (solid) and ground based radar measurements [12]. Errors for each of the M_s^+ sources are no greater than 0.02.

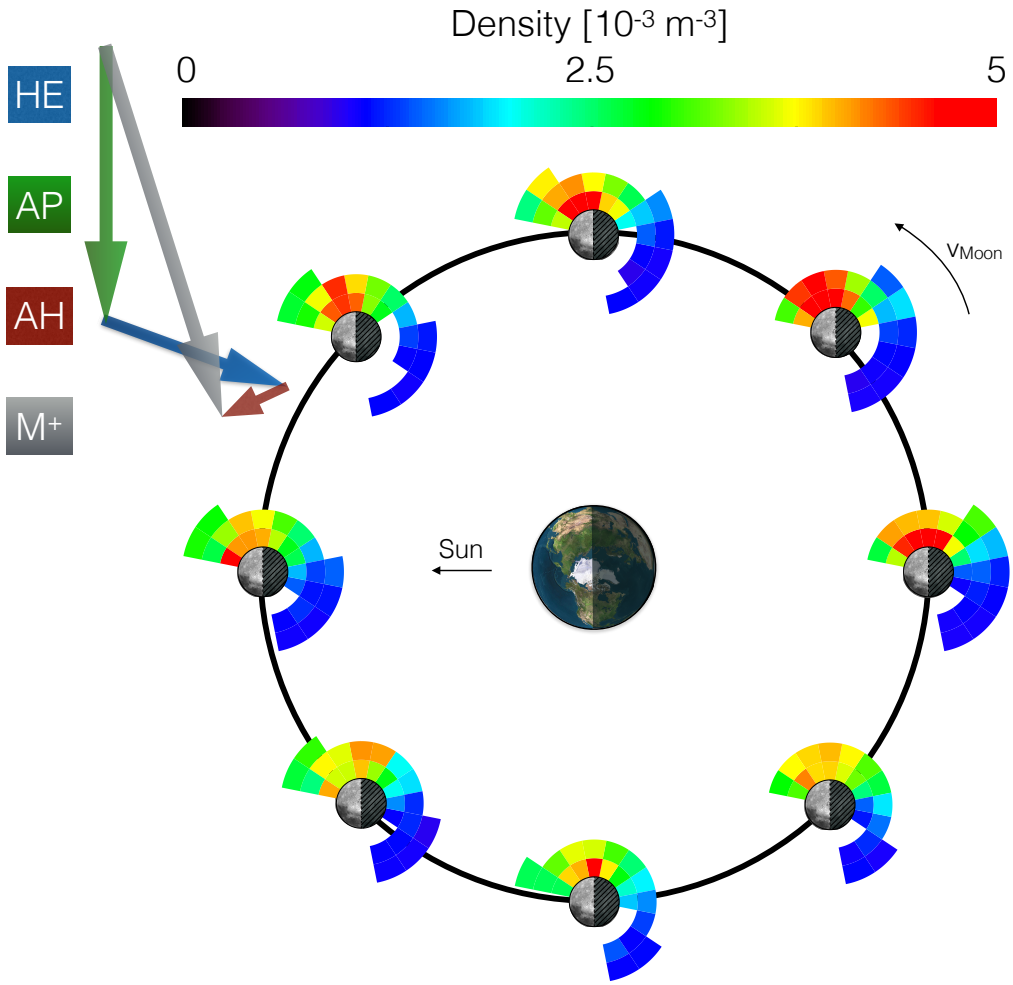

Figure 3.10: Lunar phase averaged cloud densities shown for 45° increments. Each color ring in the densities represent 40 km altitude bins. A peak lunar dust cloud density is observed while the Moon is in its waning gibbous phase, consistent with the finding that the AP & HE sources dominate over the AH source in this observation period.

However, our understanding of the Moon's response to its local meteoroid environment still remains incomplete. While the flux ratio of the HE to AH source can be derived from our fits due their similar impact parameters, the flux ratio of the AP source to either the HE or AH source is difficult to estimate. For example, the AP to HE flux ratio is both a function of the characteristic masses and velocities of each source

$$\frac{F_{\mathrm{AP}}}{F_{\mathrm{HE}}} = \frac{M^{+}_{\mathrm{AP}}}{M^{+}_{\mathrm{HE}}} \left(\frac{m_{\mathrm{HE}}}{m_{\mathrm{AP}}}\right)^{(1+\alpha)} \left(\frac{v_{\mathrm{HE}}}{v_{\mathrm{AP}}}\right)^{\beta}. \tag{3.9}$$

The AP source is primarily comprised of retrograde particles with an impact velocity of approximately 60 km/s, most likely originating from Halley Type or Oort Cloud Comets [12, 10, 62]. Its characteristic mass is most likely different than that of the HE/AH particles. Additionally, due to the nature of meteoroid detection from Earth, the velocity distribution as measured by radar does not accurately represent the true velocity distribution of incoming particles below a critical ionization cutoff at low velocities (<15-20 km/s) [61, 44]. Therefore, estimating the characteristic velocity v_{HE} (or similarly, v_{AH}) at the Moon becomes difficult; we do not attempt to derive an apex flux ratio in this work and suggest this task as a future line of study.

Chapter 4

Meteor Showers at the Moon

The previous chapter focused on the bulk characteristics of the lunar dust cloud and the variability of this cloud on timescales of a month or a year. In this chapter, we look at enhancements in the cloud density over short periods of a few days. As discussed in the introduction, the multitude of meteoroid showers which impact the Earth also impact the Moon. The meteoroid flux from some of these showers can be considerably higher than the average sporadic background and leads to temporary enhancements in the lunar dust cloud density in a localized manner. Section 4.1 describes the identification of "bursts" of particles measured by LDEX and identifies six periods of particularly enhancement activity. Section 4.2 uses groupings of these bursts to determine the radiant of the meteoroid shower which generated the largest measured activity enhancement, the Geminids meteoroid shower. Section 4.3 applies the same method to the five additional identified enhanced activity periods. Section 4.4 summarizes these measurements and discusses the extracted radiants and their errors given the method outlined in this chapter.

4.1 Burst Detections

The Moon is continually bombarded by IDPs from meteoroid streams, as well as the sporadic background. Surface regions that are transiently exposed to higher than average IDP fluxes respond with an increased mass production M^+ during these periods, and generate more frequent and denser ejecta plumes. If LADEE happens to fly through any of these plumes it is expected to observe higher than average impact rates. Hence, a period of unusually large impact rates detected by

LDEX can be used to identify the surface region that has been exposed to high incoming IDP fluxes during that period.

4.1.1 Identification of Unusual Periods

Throughout LADEE's six month science phase in orbit around the Moon, LDEX observed an average rate of $\simeq 1$ impact per minute. However, intermittently, LDEX detected "bursts" of tens to hundreds of impacts in a single minute. Particles detected in a burst most likely originate from the same well-timed and well-positioned lunar impact event that occurred just minutes before their detection on the ground-track of LADEE. These bursts are detections of individual ejecta plumes, dense enough to register multiple impacts on LDEX as it transits the plume.

LDEX received impacts above its detection threshold of $a > 0.3$ μm at a rate of $\mu = 2.3 \times 10^{-2}$ s^{-1} during commissioning and $\mu = 3.1 \times 10^{-2}$ s^{-1} during the nominal science mission, which began on 21-Nov-2013 [42]. We assume that subsequent impacts are independent of each other, hence the dust detection time series observed by LDEX can be approximated as a Poisson process. The probability of detecting n impacts within a time Δt can be calculated [64]

$$P(n, \Delta t) = 1 - e^{-\mu \Delta t} \sum_{n'=0}^{n-2} (\mu \Delta t)^{n'} / n'!, \tag{4.1}$$

where n is the number of impacts, Δt is the total elapsed time for the impacts, and μ is the average impact rate for the entire time series of dust detections. The upper limit of $n-2$ in the summation is due to the the fact that Δt begins and ends at individual particle detections. For example the probability of detecting 2 particles separated by time Δt is $P(2, \Delta t) = 1 - e^{-\mu \Delta t}$, as expected.

Bursts are short unusual periods that are identified in our time series analysis by setting an optimum value for n, and identifying low probability periods [64]. With n set to large values ($n \gg 20$), many bursts will be missed as the bursts LDEX detected contained considerably smaller numbers of particles. A small value of n identifies too many unusual periods, and makes it cumbersome to recognize if they actually belong to a single impact with a larger number of particles. By varying n, we found $n = 20$ to be a convenient particle number per burst for this analysis,

which is about the average number of particles comprising LDEX bursts. Unless stated otherwise, $P = P(n, \Delta t)$ with $n = 20$ will be used through the remainder of this analysis. Given the broad range in the exponent of the probabilities, it is convenient to express $P = 10^{-\gamma}$ in terms of its exponent $\gamma = -\log_{10} P$. Figure 4.1 shows γ for each consecutive 20 impact detections. If more than 20 impacts occur in a given burst, only the first 20 are counted. Any impacts occurring less than 30 seconds after a burst of 20 particles are considered part of this burst and removed from the analysis.

To identify unusual periods in the LDEX data, we set 2 criteria:

1) The impact rate deviation r_d exceeds 3σ above the average, either for $a > 0.3$ or 0.7 μm

2) The detected burst rate N_{burst} for $a > 0.3$ μm exceeds the average sporadic background N_{sp} by a factor of 3.

The impact rate deviation r_d is calculated by $r_d = r_{\text{day}} - r_{\text{week}}$ where r_{day} and r_{week} are running averages of the impact rates over a period of 1 day and 1 week, respectively. The 1 week average gives an estimate of the background to be subtracted from the impact rates, and 3σ is chosen to identify particularly unusual periods. LDEX occasionally observed bursts with atypical size distributions, some of which had significantly more larger particles than the average cloud. Due to this variation, two size cuts (0.3 and 0.7 μm) are utilized to ensure impact rate enhancements are detected even if bursts have different size distributions.

The sporadic rate, N_{sp}, is determined by taking the average burst rate for bursts with $\gamma > \gamma_0$ (probability threshold), listed in Table 4.1 for $\gamma_0 = 3; 6; 9;$ and 12. Figure 4.1 shows r_d for both size cutoffs of $a > 0.3$ & 0.7 μm, and the burst detection rate N_{burst} for the same four γ_0 values.

4.1.2 Correlation with Established Meteoroid Streams

Table 4.2 lists the known meteoroid showers determined by visual observations given by the International Meteor Organization [58]. Table 4.1 shows each identified unusual period along with their peak time and associated stream they coincide with. With the exception of period F, each

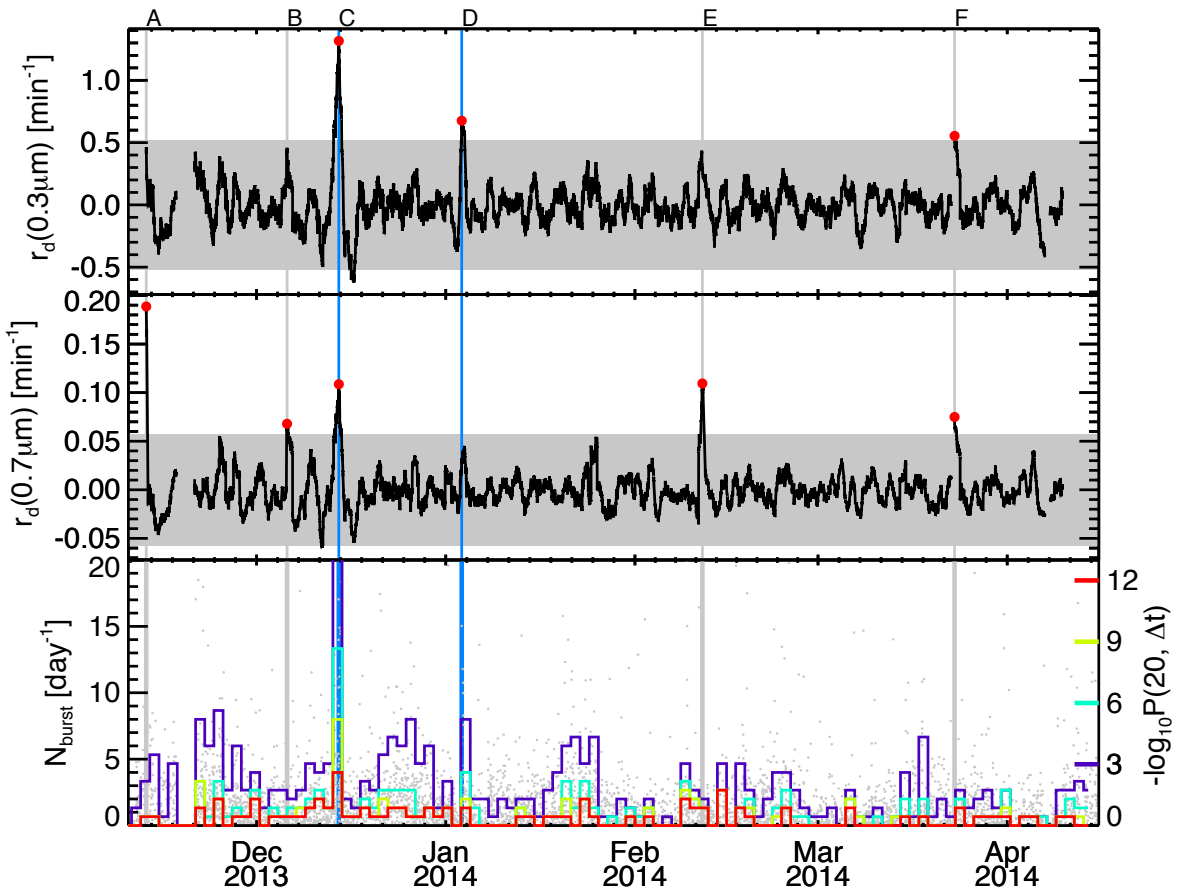

Figure 4.1: LDEX impact rates and Poisson probabilities for the duration of the mission. Top and middle: The difference between 1 day and 1 week rolling averages of the impact rate as a function of time for $a > 0.3$ & 0.7 μm respectively. The gray bar indicates 3σ error bars. Peak rates which exceed 3σ are indicated by red dots. Bottom: Gray dots show $\gamma(20, \Delta t)$ evaluated for each consecutive 20 impacts. A 1.5 day running histogram shows the total number of bursts for probability thresholds of $\gamma_0 = 3$; 6; 9; and 12; in purple, indigo, yellow, and red, respectively. Here, period C stands apart from the other five periods as having a significantly larger number of bursts than the rest of the mission. The 6 unusual periods which satisfy Criteria 1 (gray) or both Criteria (blue) are shown with the vertical lines, labeled A-F.

Period	LDEX Peak Time	$\xi(3)$	$\xi(6)$	$\xi(9)$	$\xi(12)$	Criteria	Associated Stream or Complex
		2.6	1.0	0.7	0.5		Sporadic Background
A	12-Nov-2013 22:10	1.3	0.6	1.0	1.3	✓	Taurid Complex
B	06-Dec-2013 00:00	0.8	1.3	1.0	1.3	✓	Puppid-Velorids I Complex
C	14-Dec-2013 11:34	10.3	13.0	12.1	7.8	✓✓	Geminids
D	03-Jan-2014 14:50	3.1	3.9	3.0	2.6	✓✓	Quandrantids
E	12-Feb-2014 01:11	0.8	1.3	2.0	2.6	✓	Centaurid I/II Complex
F	25-Mar-2014 08:54	1.0	1.9	2.0	2.6	✓	?

Table 4.1: Enhanced Burst Activity Periods. The period corresponds to those labeled in Figure 4.1. $\xi(\gamma_0) = N_{\text{burst}}/N_{\text{sp}}$ gives the ratio of the number of bursts in each period with the average number of sporadic bursts with the exception of the first row of data, which gives the sporadic background burst rates N_{sp}, in day^{-1}. The associated stream or complex which is temporally coincident with each period is given in the last column.

identified period occurs during a known meteoroid shower. However, temporal coincidence alone is not sufficient to establish the detection of a meteoroid shower. If a meteoroid stream impacts the Moon on the opposite hemisphere to where the concentration of bursts were to occur, it cannot be responsible for the burst rate enhancement. For each unusual burst activity period, an estimated radiant can be calculated, and at a minimum, it must be pointing to within the same hemisphere as the temporarily coincident known shower to be classified as a potential meteoroid shower detection.

4.2 Radiant Determination

During Period C, LDEX observed the largest burst rate enhancement, 8-13 times greater than the sporadic background. We therefore first focus on this period to establish a method to find the radiant of the responsible meteoroid shower. A right ascension, RA, and declination, δ, are calculated for each burst by determining the radiant which intersects the burst location normal to the lunar surface. We use the period of ± 1.5 days centered around each peak time, as this was approximately the duration of each period of elevated impacted rates (Table 4.1).

LDEX's observed impact rates peaked during Period C on 14-Dec-2013 11:34 [UTC]. The expected peak flux from the Geminids was 14-Dec-2013 7:49, less than 4 hours (or 2 LADEE orbits) apart. The Geminids is a well constrained and intense shower; its radiant is established precisely by ground-based visual observations.

Figure 4.2 shows the distribution of bursts detected by LDEX during Period C for an increasing set of γ_0 values. To a good approximation, the meteoroids arrive at the Moon in a parallel beam, hence the theoretical M^+ given in Eq. 3.8 can be calculated for a single source. For $\gamma_0 = 1$ the burst distribution remains isotropic. This is to be expected as 10% probability events are not unusual. For $\gamma_0 = 7$, the remaining bursts tend to concentrate around higher M^+ regions, and for $\gamma_0 = 16$, only the most unusual bursts remain, identifying the most dense ejecta plumes.

Figure 4.2 demonstrates that increasing γ_0 (decreasing the probability cut) gives increasingly better estimates for the radiant, hence it can be used to extract the direction information for a meteoroid stream. Using γ as a proxy for the density of each measured plume, such that higher

Name	ID	Start Time [UTC]	Stop Time [UTC]	Peak Time (Moon) [UTC]	RA [deg]	Dec [deg]	v [km/s]	ZHR [hr^{-1}]
Northern Taurids	NTa	20-Oct-2013	10-Dec-2013	12-Nov-2013 10:13	58	22	29	5
Leonids	Leo	06-Nov-2013	30-Nov-2013	17-Nov-2013 15:50	152	22	71	15
α-Monocerotids	aMo	15-Nov-2013	25-Nov-2013	21-Nov-2013 16:11	117	1	65	Var
Phoenicids	Pho	28-Nov-2013	09-Dec-2013	06-Dec-2013 09:57	18	-53	18	Var
Puppid/Velids	Pup	01-Dec-2013	15-Dec-2013	07-Dec-2013 03:41	123	-45	40	10
Monocerotids	Mon	27-Nov-2013	17-Dec-2013	09-Dec-2013 02:56	100	8	42	2
σ-Hydrids	sHy	03-Dec-2013	15-Dec-2013	12-Dec-2013 01:48	127	2	58	3
Geminids	Gem	04-Dec-2013	17-Dec-2013	14-Dec-2013 05:44	112	33	35	120
Comae Berenicids	CBe	12-Dec-2013	23-Dec-2013	19-Dec-2013 22:34	175	18	65	3
Urside	Urs	17-Dec-2013	26-Dec-2013	22-Dec-2013 14:14	217	76	33	10
Quadrantids	Qua	28-Dec-2013	12-Jan-2014	03-Jan-2014 19:39	230	49	41	120
α-Centaurids	aCe	28-Jan-2014	21-Feb-2014	08-Feb-2014 06:07	210	-59	56	6
Omicron Centaurids*	oCe	09-Feb-2014	13-Feb-2014	11-Feb-2014 17:07	175	-55	51	2
γ-Normids	gNo	25-Feb-2014	22-Mar-2014	14-Mar-2014 20:55	239	-50	56	6

Table 4.2: Working List of Visual Meteor Showers from the International Meteor Organization [58] during the LADEE operational period. *The Omicron Centaurids (oCe) is a weaker shower and was added to this list due to its temporal correlation with an observed peak. The peak times have been adjusted from the peak times observed at Earth by taking into account the position of the Moon relative to Earth and correcting for the appropriate lead/lag times.

values of γ indicate lower probability events and therefore higher plume densities, we analyzed the RA and δ distributions as a function of γ_0. Bursts with larger γ are generated in regions of higher M^+ and therefore as γ_0 increases, the corresponding radiant estimates becomes more accurate. Figure 4.3 shows the mean and standard deviations for RA(γ_0) and $\delta(\gamma_0)$. We use the largest γ_0 with at least 3 remaining bursts to determine the best value for RA and δ, $\gamma_0 = 16$ in the case of the Geminids. For $\gamma_0 > 16$, we observed no considerable change in burst distributions. With $\gamma_0 = 16$, we estimate the Geminids radiant within 1σ as (RA, δ) = (92$\pm$31°, 27$\pm$8°) compared to the established radiant of (112°, 33°) [58]. Therefore, the burst rate enhancement during Period C was indeed due to the Geminids meteoroid stream.

4.3 Application to Additional Periods

The analysis outlined in the previous section provides a method to calculate the radiant of a meteoroid shower for sufficiently large number of burst detections. However, even the most intense showers can escape detection by this method if their radiant intersects the lunar surface far outside LADEE's selenographic latitude range of $\pm$23°. The Geminids hit the lunar surface in an optimal location for LADEE's orbital geometry and generated bursts at a rate up to 13 times higher than the sporadic background. This shower, corresponding to Period C, stands out in the LDEX data as the strongest stream detection. The remaining unusual periods are discussed below and compared to temporally coincident known meteoroid streams.

4.3.1 Period A: Northern Taurids

During this period, LDEX recorded one of the largest impact rate enhancements, second only to the Geminids during Period C. However, unlike the Geminids, which generated a burst rate enhancement of $\xi = N_{\rm burst}/N_{\rm sp} \leq 13$, an enhancement of $\xi \leq 1.3$ was registered during Period A (Table 4.1). The bursts measured during this period were unusually dense, with γ values up to 15. Figure 4.4 shows the burst distributions during this period. The declination is correctly estimated, however the right ascension is not. The Northern Taurids have a ZHR which is 24 times less than

the Geminids and are therefore expected to impact the Moon at a much lower rate.

4.3.2 Period B: Puppid/Velids

The Puppid/Velids stream is also known to be weak, with a ZHR of 10, and at most registered a burst rate 30% higher than the sporadic burst rate. Additionally, its radiant impacts the lunar surface at a low selenographic longitude of -45°. Due to the geometry of the LADEE orbit, throughout each orbit LDEX essentially flys through iso-M^+ or iso-φ lines, as shown in Figure 4.5. Given this geometry and the relative weakness of the stream, extracting the radiant for this stream is difficult, but still its declination is correctly estimated.

4.3.3 Period D: Quadrantids

The Quadrantids is one of the strongest observed showers on Earth, similar in ZHR magnitude to the Geminids, and was predicted to peak approximately 6.5 hours after LDEX's observed peak in Period D. Figure 4.6 shows the burst distributions during this period. The radiant of this stream intersected the lunar surface at a very high lunar latitude, 63° in selenographic coordinates. Due to the geometry, the declination for this radiant cannot be accurately determined as LDEX did not visit the relevant δ range. However, LDEX did visit a large range of RA's in this period and an accurate estimate for the RA can be extracted from the data.

4.3.4 Period E: Omicron Centaurids

An additional stream which generated a significant enhancement in LDEX impact rates, as shown in Figure 4.1, was the Omicron Centaurids (oCe). Like the Quadrantids, this stream intersected the lunar surface at an unfavorable selenographic latitude of -51° (Figure 4.7). Due to the unfavorable geometry and lower burst rate enhancement for this period of 0.8 to 2.6, radiant estimation was challenging.

4.3.5 Period F: Unidentified

Several of the documented streams produced significant enhancements in impact rate at the expected time. Surprisingly, an uncharacteristically large impact rate enhancement rivaling the Geminids, was observed on 25-Mar-2014 that does not correspond to any established shower. If this impact rate enhancement is due to a meteoroid shower, its radiant can be estimated following the analysis outlined in the previous sections.

Figure 4.8 shows the burst distribution for this period. For the largest cut of $\gamma_0 = 5$, a radiant estimate is calculated as (RA, δ) = (268$\pm$41°, -22$\pm$13°) and the local impact rate maximum gives λ = 4.1$\pm$0.3°. The constellation in the sky at this radiant is Sagittarius, hence this stream could most likely be named the Sagittarids (Sag). Figure 4.8 shows the burst distribution for this unidentified stream.

Of all documented meteoroid streams, the only candidate stream with possibly similar temporal and spatial parameters to the unidentified stream on 25-Mar-2014 is the ζ-Serpentids shower. However, this stream is relatively weak and remains fairly unconstrained. The Meteor Data Center [69] gives the following radiant parameters: λ=5° and (RA, δ) = (266°, -6.3°). The RA value is within 1σ of the LDEX calculated radiant, with δ within 2σ and λ is within 1° (or one day) of the observed lunar peak time. However, the SonotaCo meteor orbit database gives a solar longitude for the ζ-Serpentids of λ=365°, with (RA, δ) = (266°, -6°) [30]. The radiant direction given in [30] could be consistent with the LDEX results, however the solar longitude is considerably different. Additionally, the lunar response to the unidentified stream is similar to the intense impact rates observed during the Geminids. This is not consistent with the low magnitude of the ζ-Serpentids which remains poorly characterized by ground-based observations.

4.4 Extracted Radiant Parameters

Table 6.1 summarizes the LDEX radiant estimates of the meteoroid showers. Of the 6 identified periods, the Geminids produced the largest burst rate enhancement. The LDEX data from this

period unambiguously verifies the detection of the lunar response and successfully extracts both radiant parameters as well as the peak time. For Periods A, B, D, & E, which correlate temporally to known showers, the radiant estimates were more difficult to extract. These difficulties arose from unfavorable geometry, low relative meteoroid stream strength, or both. The Quadrantids, which is comparable in magnitude to the Geminids as observed at Earth, generated the 2nd highest burst rate detected throughout the mission. However, due to its high selenographic latitude, it's declination can only be poorly reproduced.

Many of the streams listed in Table 4.2 did not generate significant burst rate enhancements. While the non-detection of these streams is largely unsurprising due to their low ZHR, the Leonids is strongest amongst these and should have registered a burst rate enhancement given the favorable geometry and its larger ZHR. However, LDEX turned off a few hours before the Leonids peak time and remained off for a few days due to spacecraft operational constraints, thereby missing this stream.

Table 4.3: Extracted Meteoroid Stream Parameters. The established three letter identification code is id, λ is the peak time in solar longitude, RA is right ascension, δ is the declination, $N(3)$ is the number of bursts with a probability cut of $\gamma_0 = 3$, and ZHR is zenith hourly rate [58]. Earth observed values [58], propagated in time to the position of the Moon at each peak time. The error on λ for LDEX measured values was calculated assuming LDEX could not resolve a maximum in impact rate within three LADEE orbits, corresponding to approximately 6 hours or 0.3° in solar longitude. Highlighted in bold are the values for which the estimates are within 1σ.

Per.	id	Lat [deg]	λ [deg]	λ_{LDEX} [deg]	RA [deg]	$\mathrm{RA}_{\mathrm{LDEX}}$ [deg]	δ [deg]	δ_{LDEX} [deg]	$N(3)$ [day^{-1}]	ZHR [day^{-1}]
A	NTa	1	227.7	**227.8±.3**	58	118±38	22	-5±27	3.3	5
B	PuV	-64	253.8	252.5±.3	123	205±19	-45	**-41±14**	2.0	10
C	Gem	10	261.6	**261.8±.3**	112	**92±31**	33	**27±8**	26.7	120
D	Qua	63	284.4	**284.6±.3**	230	**225±12**	49	-25±17	8.0	120
E	oCe	-50	325.1	**325.4±.3**	175	273±13	-55	-7±40	2.0	2
F				4.1±.3		275±38		-23±13	2.7	

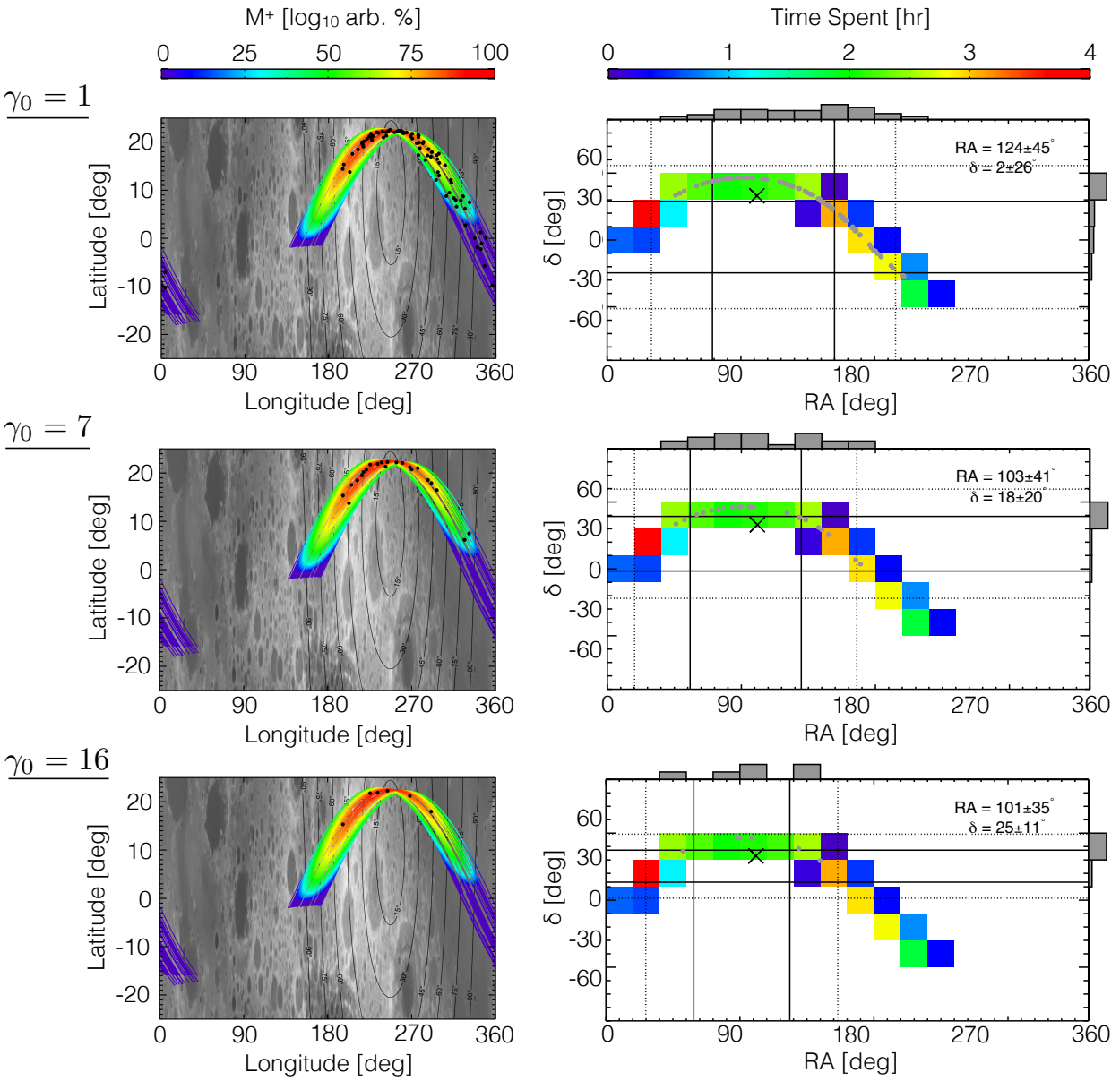

Figure 4.2: The burst distributions for probability cuts $\gamma_0 = 1, 7$, and 16, showing the correlation between γ_0 and the distribution of bursts around peak Geminids M^+. *Left column:* The LADEE trajectory for ± 1.5 days centered around the peak Geminids time, colored by M^+ from Equation 3.8 for a single source. Black dots mark the locations of bursts observed by LDEX, and the black contour lines show the angle φ of impact for the incident Geminids particles with respect to the surface normal. *Right column:* The RA and δ distributions for the bursts (gray dots). The color bar indicates the time spent in each [RA,δ] bin and the gray histograms on the top/right of each panel show the number of bursts per bin. The solid and dotted lines mark 1σ and 2σ error bars, respectively, and the large x marks the true radiant [58].

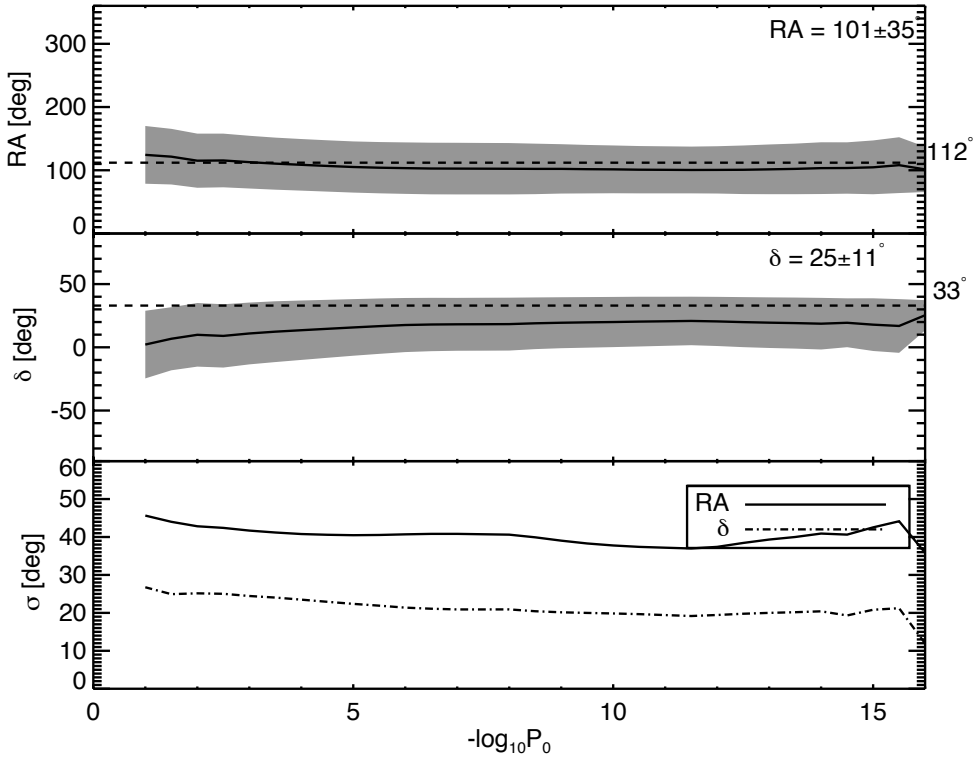

Figure 4.3: The RA (*top panel*) and δ (*middle*) values respectively for the bursts measured during the Geminids shower, as a function of $\gamma_0 = -\log_{10} P_0$. The solid line indicates the mean value and the gray band shows 1σ error. The horizontal dotted lines indicate the Earth observed radiant values [58]. *Bottom:* The 1σ error for RA and δ.

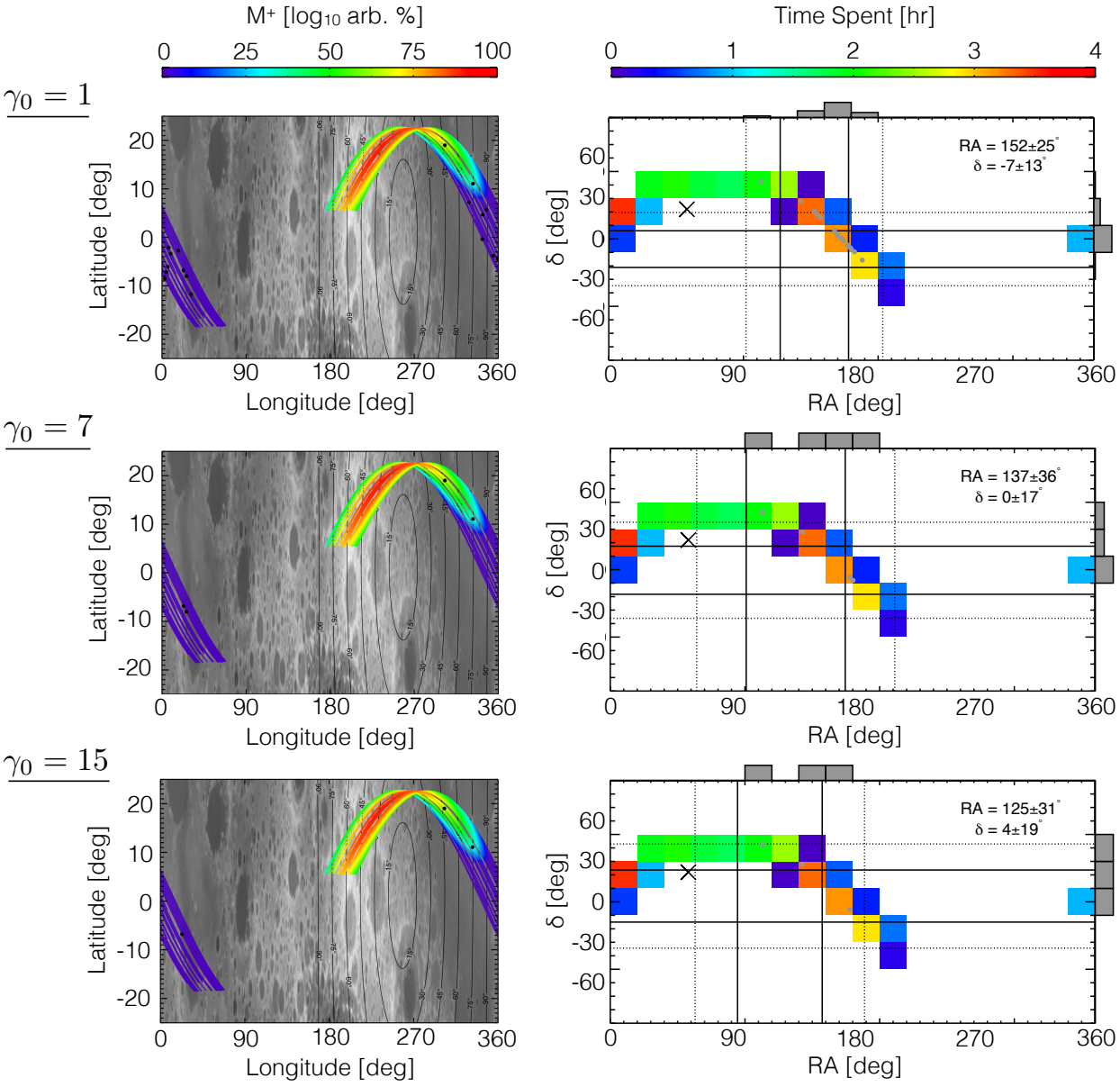

Figure 4.4: The burst distributions during Period A for $\gamma_0 = [1, 7, 15]$, corresponding to the Northern Taurids. See Figure 4.2 caption for further explanation.

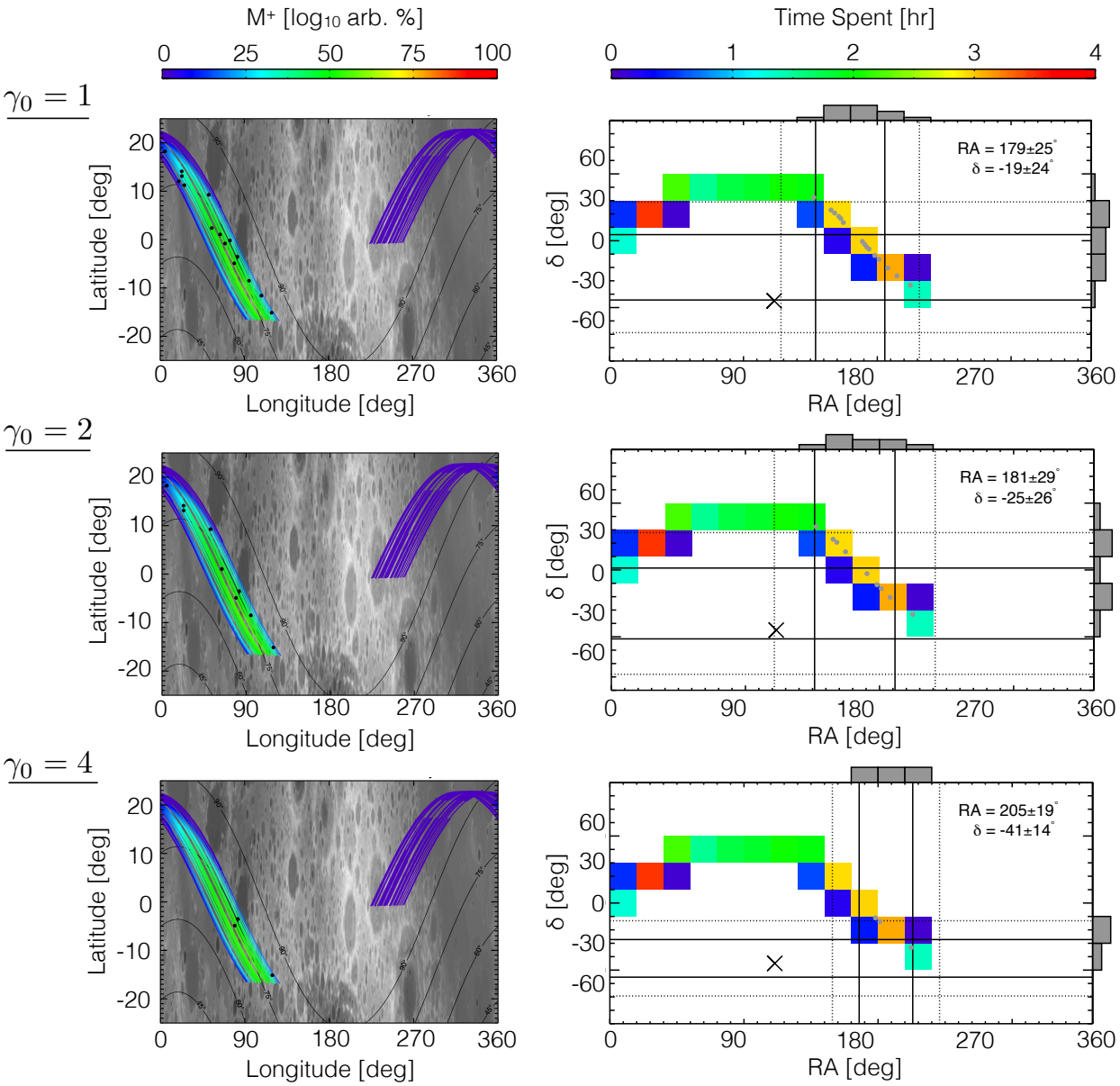

Figure 4.5: The burst distributions during Period B for $\gamma_0 = [1, 2, 4]$, corresponding to the Puppid/Velids. See Figure 4.2 caption for further explanation.

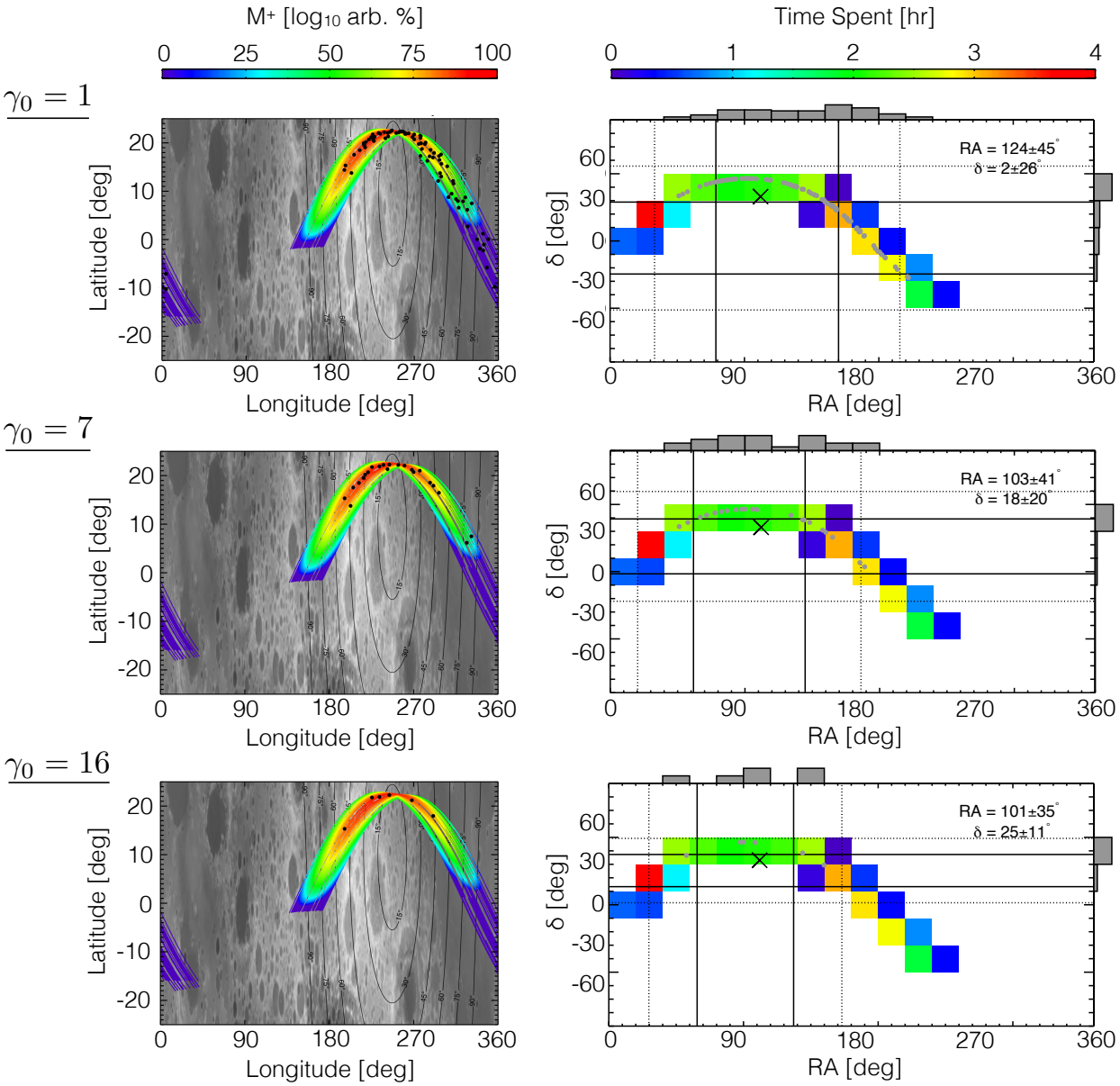

Figure 4.6: The burst distributions during Period D, corresponding to the Quadrantids for $\gamma_0 = [1, 7, 15]$. See Figure 4.2 caption for further explanation.

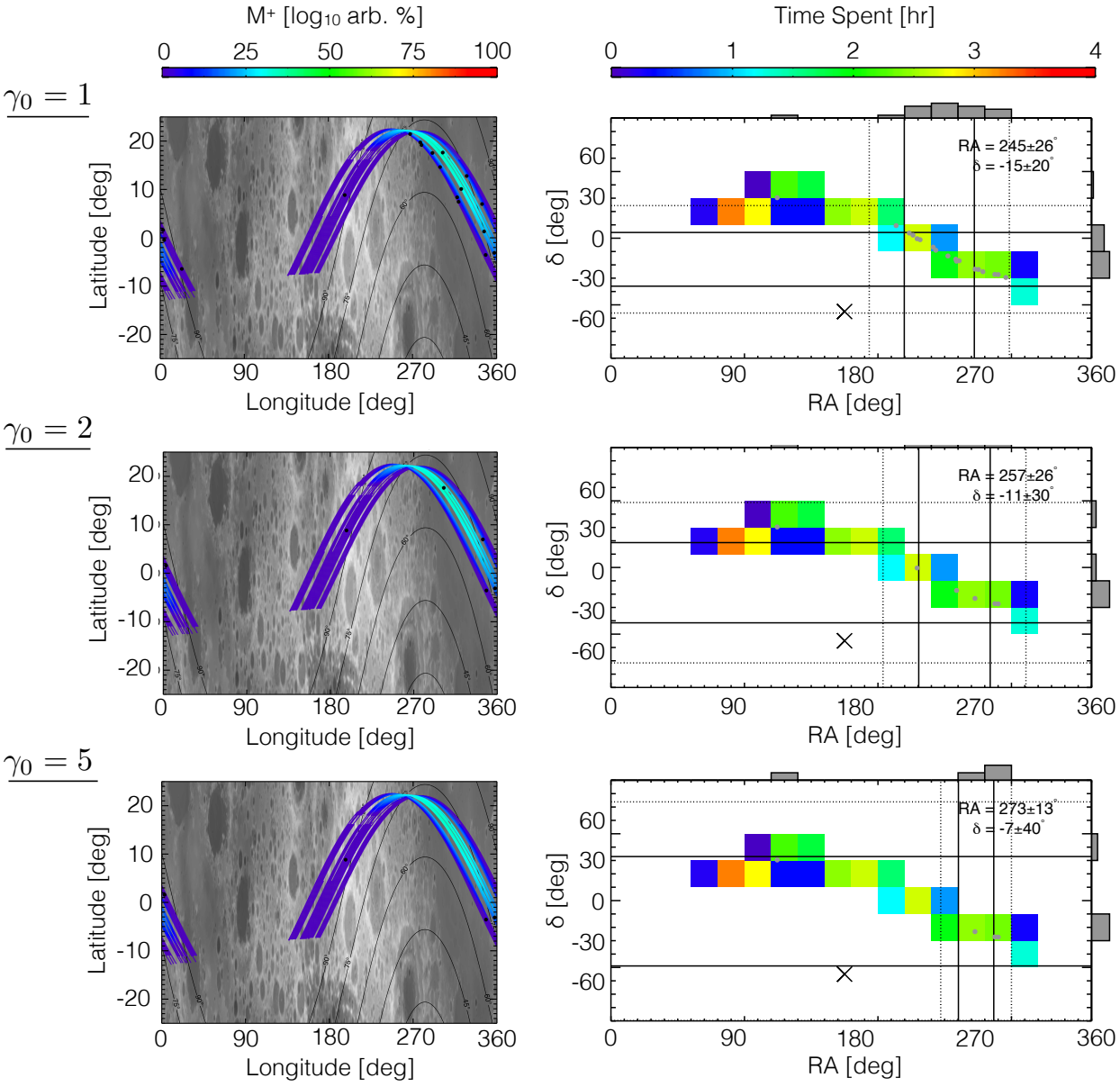

Figure 4.7: The burst distributions during Period E, corresponding to the Omicron Centaurids for $\gamma_0 = [1, 2, 5]$. See Figure 4.2 caption for further explanation.

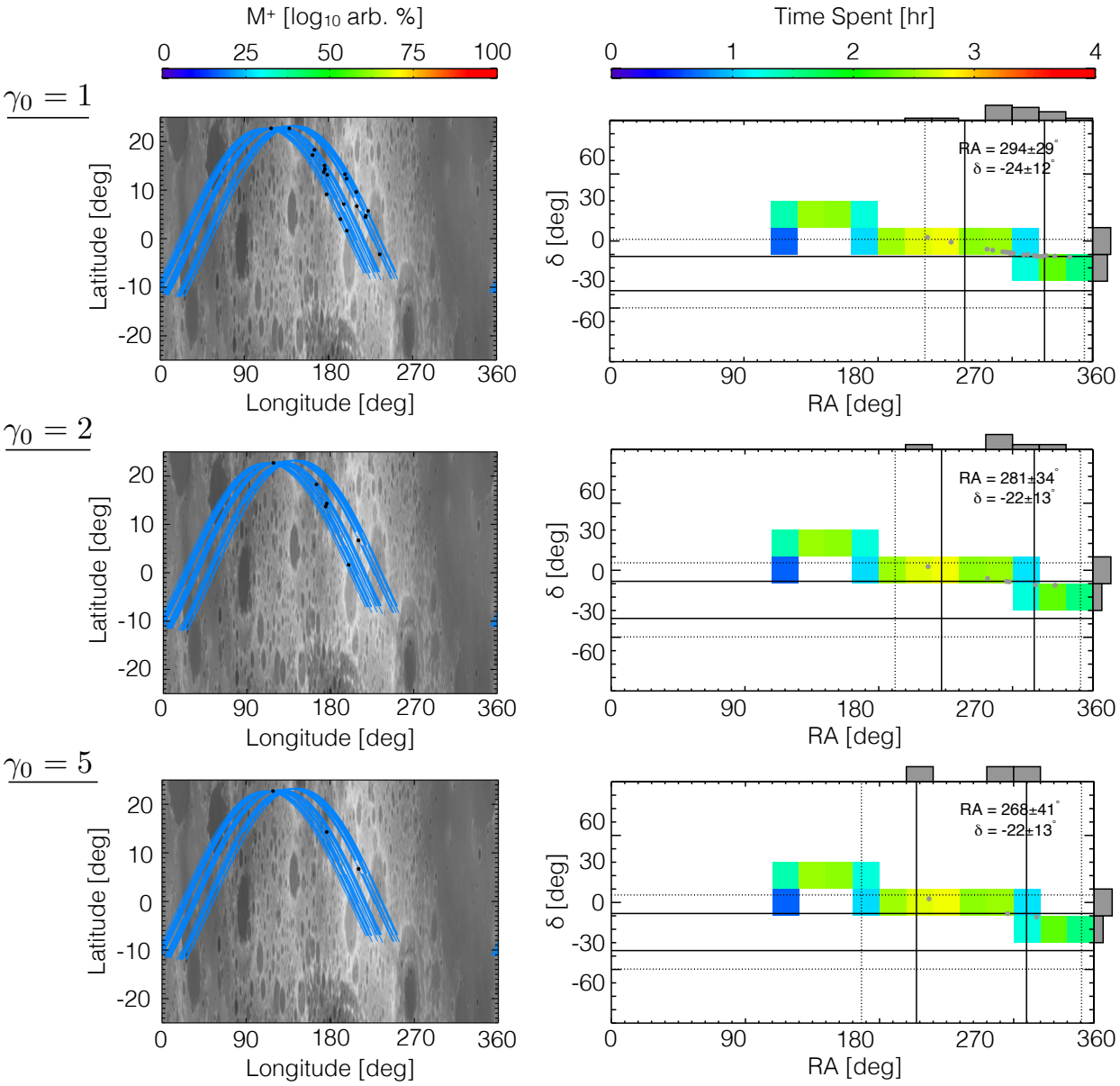

Figure 4.8: The burst distributions during Period F for $\gamma_0 = [1, 2, 5]$. For $\gamma_0 > 5$, there were less than 3 bursts. See Figure 4.2 caption for further explanation.

Chapter 5

Ejecta Plume Model

While the previous chapter focused on groupings of dense plumes detected by LDEX, this chapter will investigate the structure of individual plumes. Section 5.1 outlines how we determine the largest plume measurements in LDEX data and find four plumes to be significantly denser than all other measured plumes. To understand these measurements, we developed a model of impact ejecta plumes, described in Section 5.2. Section 5.3 describes the dynamics of ejecta plumes and the detection geometry involved in making measurements with a dust detector. Section 5.4 compares the LDEX data to the model and finds good agreement with the data. Section 5.5 discusses the findings of this analysis in the context of our previous understanding of impact ejecta plumes and gives an outline for future lines of study to further investigate this process.

5.1 Identifying Dense Plume Detections

To constrain the properties of ejecta plumes, we identify bursts with the largest number of particles. First, we implement a method to determine the number of particles per plume detection. In the previous chapter, consecutive bursts were removed from the analysis as we were strictly counting the total number of bursts and not the number of impacts within. In this analysis, we are concerned with the total number of impacts in a given plume and therefore we group consecutive bursts together. We search for bursts with n particles and probability of their subsequent detection to be less than P occurring within a sliding window of 30 seconds and group these together. In this way, we are able to estimate the total number of particles contained in each plume as

$N_{\text{plume}} = nN_{\text{b}}$, where N_{b} is the number of consecutive bursts. For the remainder of this discussion, plume detections are defined as a groupings of $n = 5$ particles with probability $P < 10^{-3}$. Since we group consecutive bursts together, plume identification is not very sensitive to n for sufficiently small values. Additionally, as long as P is small enough to exclude unrelated groupings but not too small to exclude most events, the results are not highly sensitive to P.

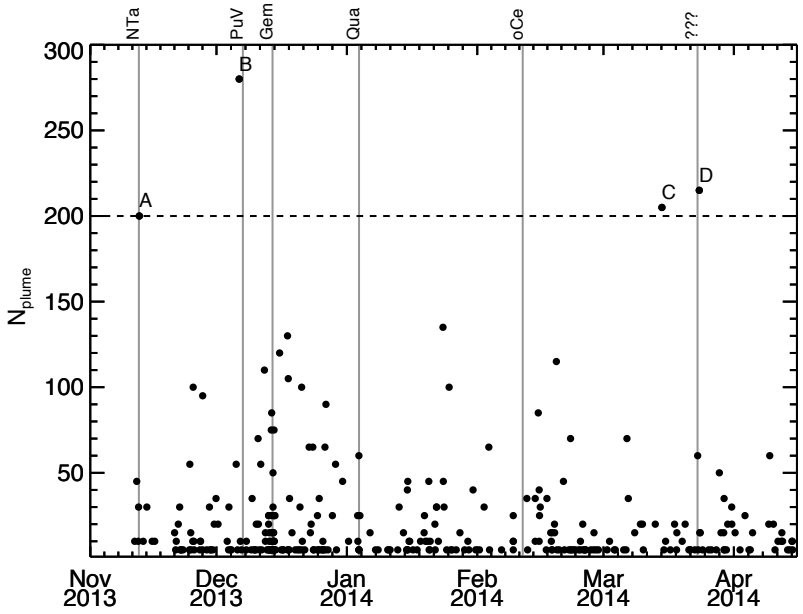

Figure 5.1: Number of impacts in each plume detection.

Figure 5.1 shows the number of impacts in each plume detected by LDEX. We investigate only the very largest plume detections, which contain 200 or greater impacts, labeled A-D in Figure 5.1 and listed in Table 5.1. Three of the four large plumes occurred during the catalogued or yet to be identified meteoroid showers discussed in the previous section.

These represent the most statistically significant detections of lunar impact ejecta plumes by LDEX. An impact rate times series for each is shown in Figure 5.2. These impact rates were calculated using a sliding window of 3 seconds and have been normalized by their peak values. The structure in any given plume detection is dependent on the time and location of LDEX relative to the lunar impact site. There is no a priori method to extract this temporal and geometric

id	Time [UTC]	N_{plume}	Alt [km]	Stream
A	12-Nov-2013 15:42	200	92	NTa
B	06-Dec-2013 09:39	280	71	PuV
C	16-Mar-2014 21:39	205	44	
D	25-Mar-2014 18:46	215	44	???

Table 5.1: The four plume measurements with $N_{\text{plume}} > 200$ particles and $P_0 < 10^{-3}$. Their peak time, total number of impacts, altitude at detection time, and temporally coincident streams (if they exist).

information from the LDEX data, therefore, a model must be used to interpret these impact rates in a meaningful way.

5.2 Model Description

A Monte-Carlo simulation was created to model the internal structure and dynamics of dust particles in an impact ejecta plume. The particles are launched with a distribution function of [42],

$$\begin{aligned} f(\varphi, v, m) &= f(\varphi) f(v) f(m) \\ f(\varphi) &= \frac{\sin\varphi}{\cos\varphi_1 - \cos\varphi_0} \\ f(v) &= \frac{1-\mu}{v_0^{1-\mu}} v^{-\mu} \\ f(m) &= \frac{\alpha}{m_{\min}^{-\alpha} - m_{\max}^{-\alpha}} m^{-(1+\alpha)}, \end{aligned} \tag{5.1}$$

as depicted in Figure 5.3. Here, φ_0 and φ_1 are the outer/inner angle from the surface normal respectively, v is the initial speed, and m is the grain mass. The mass and speed exponents are determined experimentally by LDEX to be $\mu = 3.4 \pm 0.1$ and $\alpha = 0.91 \pm 0.003$ [42]. The mass bounds are driven by the LDEX detection limits and are set to $[m_{\min}, m_{\max}] = [10^{-17}, 10^{-8}]$ kg corresponding to radius thresholds of $[a_{\min}, a_{\max}] = [0.1, 100]$ μm at the spacecraft apex velocity. To determine the trajectories of the simulated particles, a selection of orbits are numerically integrated on a grid of (φ, v). For each given (φ_i, v_j) pair of initial conditions, their equation of motion,

$$\ddot{\vec{r}} = -\frac{GM}{r^2}\hat{r} \tag{5.2}$$

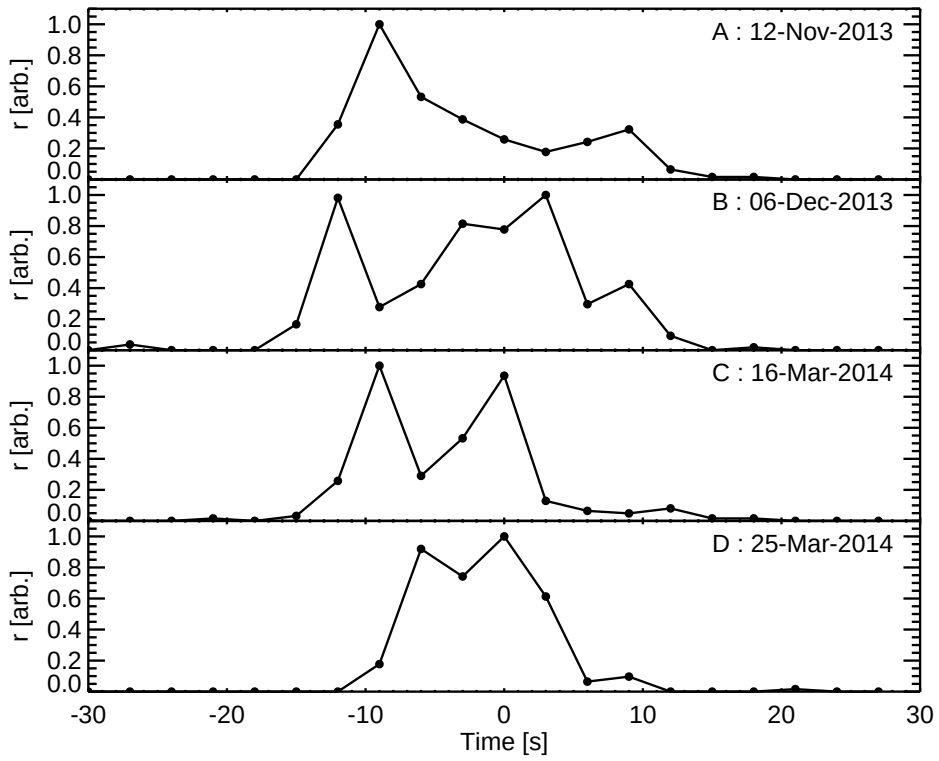

Figure 5.2: Impact rate time series for plumes A-D identified in Figure 5.1. The time for each plume has been centered on its mean plume time and the impact rates have been normalized by their peak values.

Number of Particles	Direct Integration	Interpolation Scheme	Computation Gain
100,000	∼1 hr	7 s	400

Table 5.2: Computation time comparison between directly integrating 100,000 particles and interpolating their trajectories.

is integrated numerically until each particle returns to the surface. For numerical integration, the equations are integrated in two dimensions to exploit the axial symmetry of the problem. For every trajectory, a 5th and 6th order polynomial is fit to the $x(t)$ and $z(t)$ solutions respectively, such that,

$$x(t) = \sum_{n=0}^{5} A_n t^n \qquad z(t) = \sum_{n=0}^{6} B_n t^n \tag{5.3}$$

and their polynomial coefficients $(A_{i,j}, B_{i,j})$ for each (φ_i, v_j) are stored in a grid, depicted in Figure 5.4. The polynomial orders of $x(t)$ and $z(t)$ are odd and even respectively since $x(t)$ is a monotonic function and $z(t)$ has parabolic-like character. The grid is populated with fit coefficients $(\vec{A}_{i,j}, \vec{B}_{i,j})$ in the range of $\varphi \in [0°, 50°]$ and $v \in [50, 2350]$ m/s with evenly spaced steps of $(\Delta\varphi, \Delta v) = (0.5°, 100$ m/s). To retrieve the trajectory for any arbitrary (φ, v) pair, $\vec{r}(\varphi, v)$ is calculated via bilinear interpolation on the (φ_i, v_j) grid.

A comparison was performed between the polynomial derived trajectories and the true trajectories calculated by numerical integration. Figure 5.5 shows an example of a typical particle trajectory used in the ejecta plume modeling and the error as a function of time. For particles returning to the surface, the error was no greater than 0.01% at their turning point altitudes. This method was used preferentially over direct integration as it reduced the computation time by a factor of approximately 400, as shown in Table 5.2.

5.3 Plume Dynamics and Detection Characteristics

To illuminate the dynamics of an ejecta plume an example plume is utilized throughout this section. The model parameters for this plume are: $N_{\text{part}} = 10^6$, $\varphi_0 = 20°$, $\varphi_1 = 5°$, $v_{\min} = 400$ m/s, and $v_{\max} = 765$ m/s. The velocity bounds are chosen to restrict the plume particles to the altitude

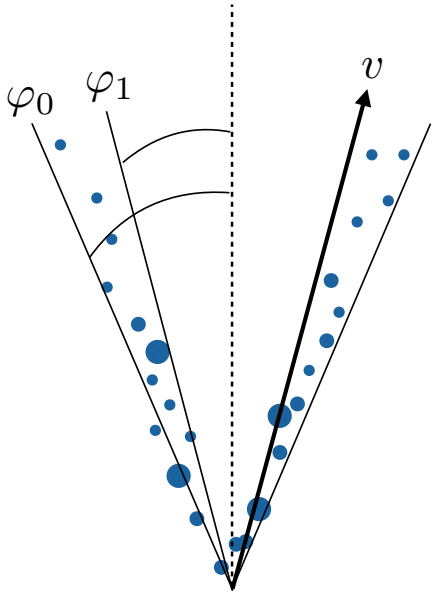

Figure 5.3: Diagram of the ejecta plume distribution.

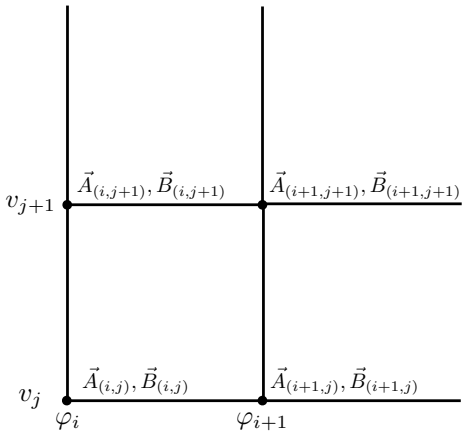

Figure 5.4: Visual representation of the polynomial coefficient grid calculated for the trajectory initial conditions of (φ, v).

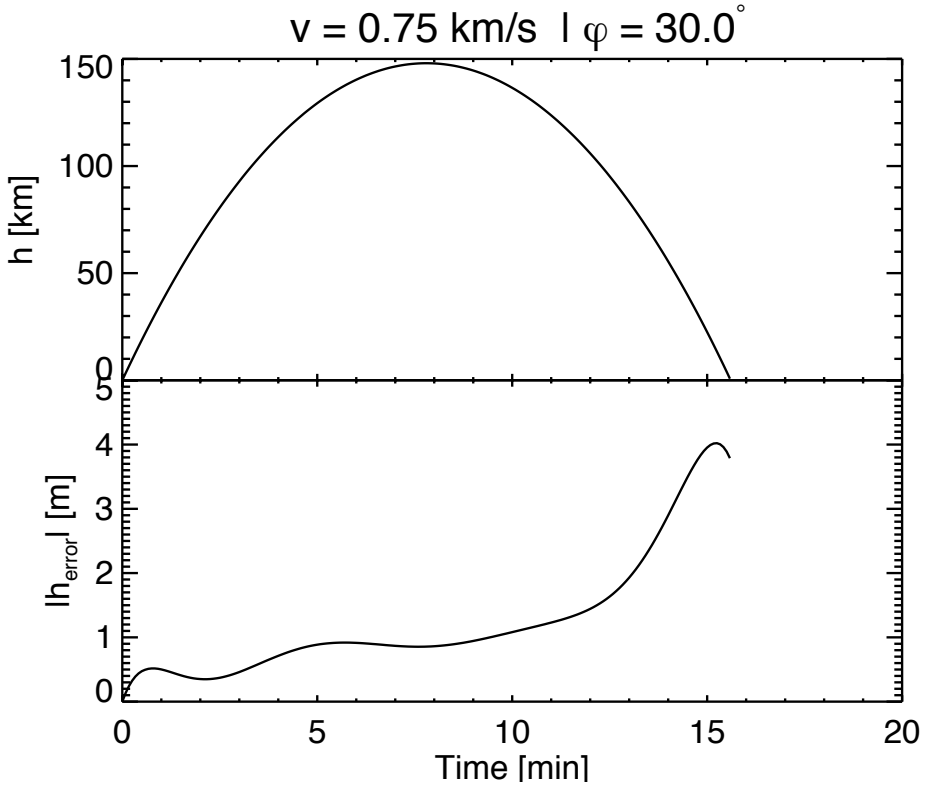

Figure 5.5: An example of the error as a function of time between the direct integration of a particle trajectory and the interpolation scheme. The trajectory scale is given in kilometers while the error is given in meters.

range of $h = 50$ - 150 km. Once the particles are launched from the surface with the distribution function given by Equation 5.1, they disperse vertically and radially. Figure 5.6 shows the positions of the simulation particles at four different times corresponding to 75, 150, 225, and 300 seconds after launch, and the corresponding number densities. The plume is found to be the most dense in the lower interior portion of each curtain and the density decreases as the cloud spreads out in time.

LDEX measures impact rates, not densities. Therefore, to compare modeled plumes to LDEX measurements, local impact rates must be calculated. LDEX's lowest detectable mass is a function of velocity, $m_{\min} = Cv^{-\mu}$ where $C = 4.8 \times 10^{-15}$, $\mu = 4.76$, and v is given in km/s [41]. The impact rate is

$$r = \int \Delta N/\Delta t = \int\int\int \mathrm{d}\mathbf{x}\, \mathrm{d}^3 v\, \mathrm{d}m\, A(\omega)\, \cos\omega\, \Theta(\cos\omega)\, n(m, \mathbf{v}, \mathbf{x})\, |\mathbf{v}_{\mathrm{imp}}| \Theta\left(m - C|\mathbf{v}_{\mathrm{imp}}|^{-\mu}\right) \tag{5.4}$$

where $\mathbf{v}_{\mathrm{imp}} = \mathbf{v} - \mathbf{v}_{\mathrm{sc}}$ is the grain impact velocity, $\mathbf{v}$ is the velocity of each grain, $\mathbf{v}_{\mathrm{sc}}$ is the spacecraft velocity, $\omega = \cos^{-1}(\mathbf{v}_{\mathrm{imp}} \cdot \mathbf{v}_{\mathrm{sc}}/|\mathbf{v}_{\mathrm{imp}}||\mathbf{v}_{\mathrm{sc}}|)$ is the angle between $\mathbf{v}_{\mathrm{imp}}$ and $\mathbf{v}_{\mathrm{sc}}$, $A(\omega)$ is the effective area of LDEX (Figure 2.4), $n(m, \mathbf{v}, x, z)$ is the dust number density, m is the dust grain mass, and $\Theta\left(m - C|\mathbf{v}_{\mathrm{imp}}|^{-\mu}\right)$ is a Heaviside function which ensures only particles above LDEX's detection threshold are counted. The LDEX boresight is assumed to be parallel to the spacecraft apex; for each detected plume in Table 5.1 the angle between the two was $\leq 1^\circ$. The dust grain velocity distributions are shown in Figure 5.7. Convolving this with the mass dependence in Equation 5.4, and assuming LDEX has a velocity vector at every location of $\mathbf{v}_{\mathrm{sc}} = 1.67\,\hat{\mathbf{x}}$ km/s allows for the calculation of a local, instantaneous impact rate throughout the plume, were LDEX to fly through that location.

While larger densities certainly lead to higher impact rates, these rates are not solely dependent on the dust number density. The impact velocity vector $\mathbf{v}_{\mathrm{imp}}$ plays a critical role as it determines both the LDEX effective detection area $A(\omega)$ and the minimum detectable mass $m_{\min}$. With larger impact velocities, LDEX can detect smaller particles, which have higher number den-

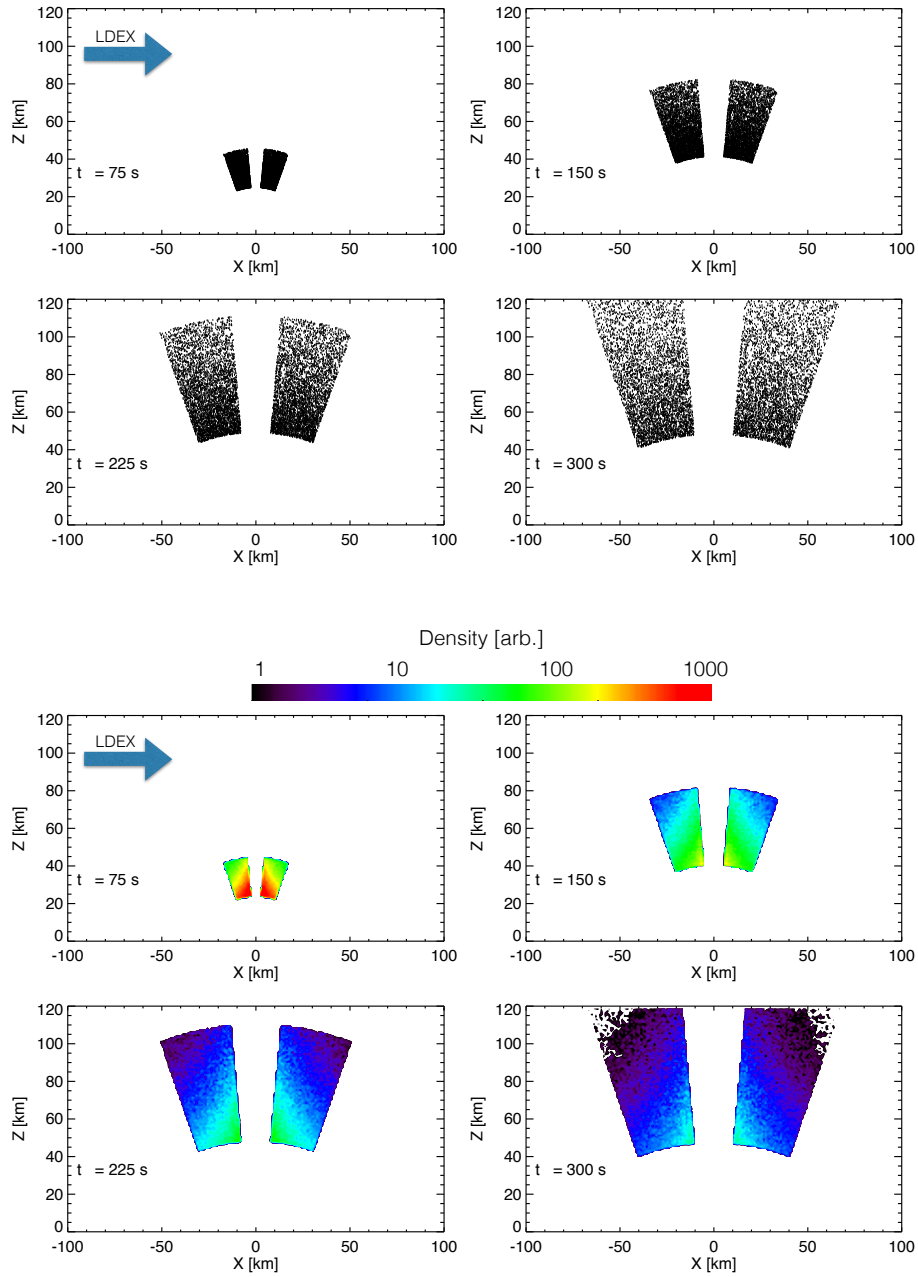

Figure 5.6: Top four: Modeled ejecta plume particle distributions for 100,000 particles at four different times. Bottom four: Modeled ejecta plume densities for four different times. Model parameters are $\varphi_0 = 20°$, $\varphi_1 = 5°$, $v_{\min} = 400$ m/s, and $v_{\max} = 765$ m/s.

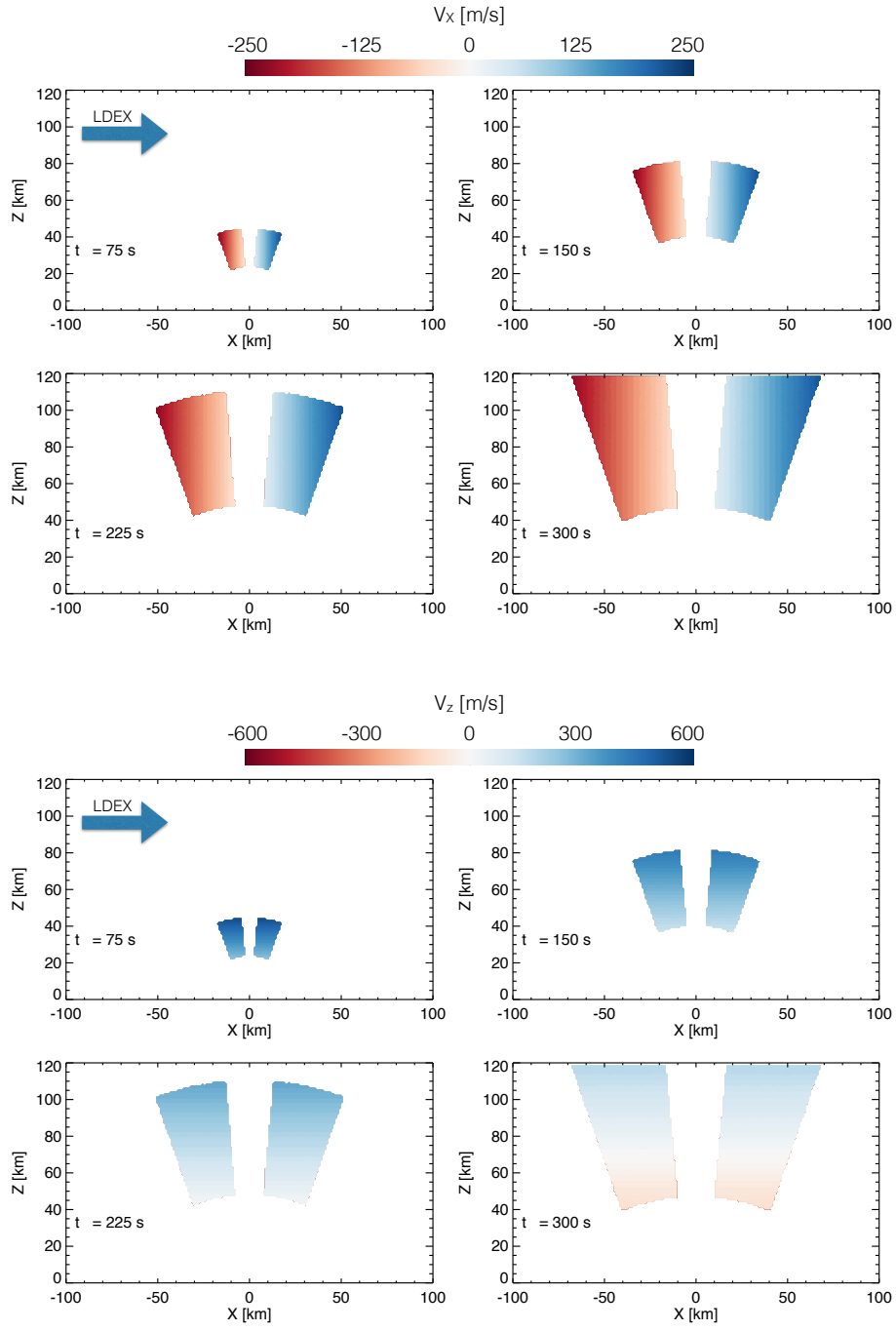

Figure 5.7: Modeled ejecta plume velocities V_x (top four) and V_z (bottom four) for four different times. See Figure 5.6 for model parameters.

sities. Since the mass distribution function is a power law, $f(m) \propto m^{-1.9}$ [42], small changes in $|\mathbf{v}_{\text{imp}}|$ can lead to a significant modulation in impact rates. Additionally, due to LDEX's response function (Figure 2.4), groups of particles with large impact angles will have significantly lower impact rates. Hence, the largest impact rates are produced when n and $|\mathbf{v}_{\text{imp}}|$ are large and ω is small. In this setup, impact rates are the largest when v_x is large and negative and v_z is small.

Figure 5.8 demonstrates the interplay between density and impact velocity in determining impact rates. Impact rates are calculated throughout the plume by assuming LDEX is instantaneously transiting everywhere in the entire plume. The velocity dependence is clearest in the discrepancy between the inbound (-x) and outbound (+x) curtains of the plume. The densities in each curtain are the same. However, since LDEX is moving in the +x direction relative to the plume, the inbound curtains have higher impact velocities, hence larger impact rates. This is clearly demonstrated in the impact rate asymmetry between the two curtains in Figure 5.8.

When comparing impact rates for regions with different densities or times, the interplay is even more complex. At $t = 75$ s, the grains are moving with large v_z, however the densities are very high since the plume has not had significant time to evolve and disperse. At this time, the large density overcomes the low effective area due to the large v_z of the grains and large impact rates are predicted. At $t = 150$ s, the density has decreased by a factor of ~ 10 and the vertical velocities are still large. In this regime, the densities are not large enough to account for the low effective area and a decrease in the impact rate of at least a factor of 2 is found.

For the 3rd and 4th time steps shown in Figure 5.8, the regime changes as the particles begin to arrive at their vertical turning points, reaching optimal velocity conditions for particle detection. The slowest particles in this simulation were launched with a velocity such that their vertical turning points occur at approximately 50 km after 255 seconds. At $t = 225$ s the densities have continued to decrease, however the vertical velocities at the bottom of the curtain are approaching zero, leading to small ω (large effective area) and therefore generate the highest impact rates. Finally, at $t = 300$ s, the lowest portion of the cloud has begun to descend. A peak is observed at approximately 70 km, which is the altitude of particles which reach their turning points at approximately 300 s. In

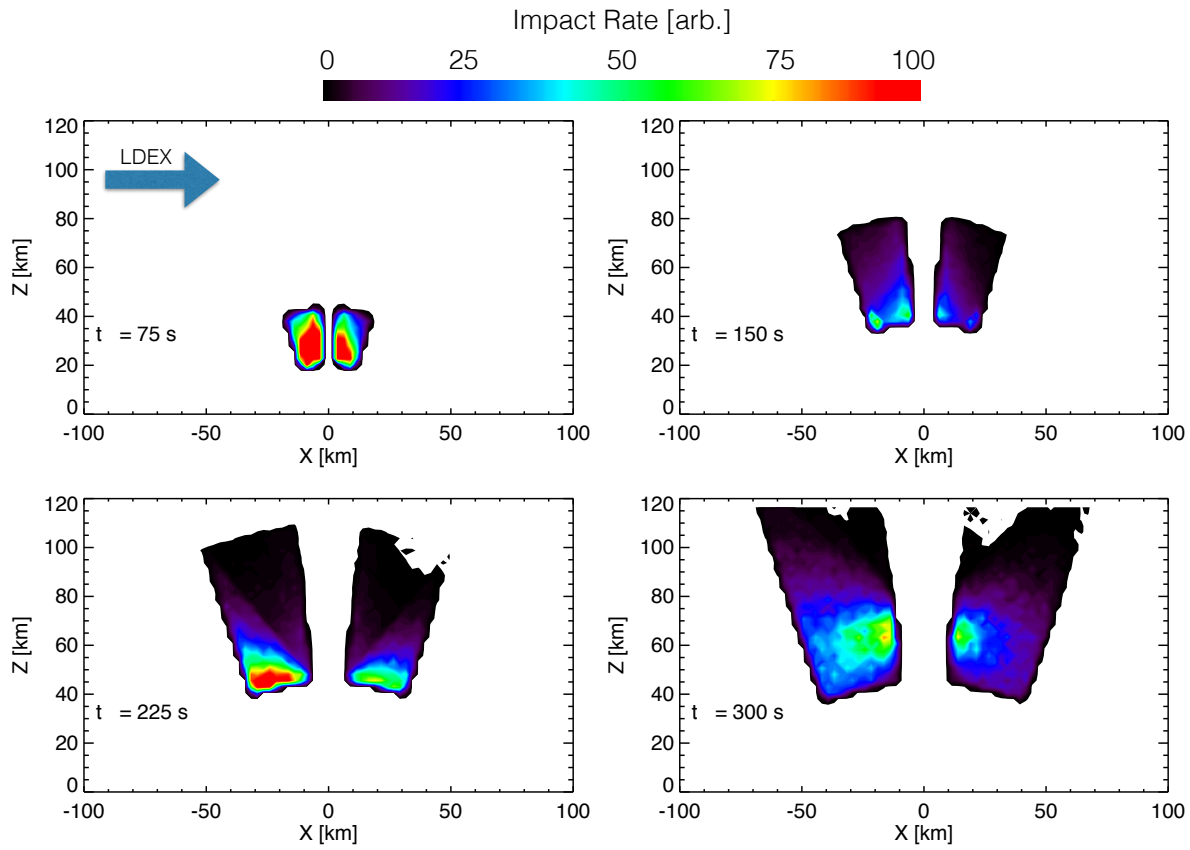

Figure 5.8: Modeled ejecta plume impact rates for four different times. Rates are calculated for the entire plume using Equation 5.4 by assuming LDEX is at every point in the plume instantaneously. See Figure 5.6 for model parameters.

this regime, the large density leads to the rate enhancement being located on the inner edges of each curtain, while the low velocities of particles at their turning points dictate the altitude of the impact rate peak.

5.4 Comparison to LDEX Data

The previous section outlined the dynamics of a representative ejecta plume and the impact rates a dust detector would register were it to fly through various sections of the plume at any given time. To interpret the impact rates measured by LDEX, the temporal evolution of the plume must also be taken into account. For example, if the particles in the plume are approximately restricted to a cone with a half angle of 45°, LDEX would completely transit the plume in $t_{\rm det} \approx 1.25h$. In the approximation with constant g, particles reach their vertical turning points in $t_{\rm plume} \approx 35\sqrt{h}$. For both times, t is in seconds and h is in km. $t_{\rm det}$ gives the timescale for a plume detection, while $t_{\rm plume}$ gives an estimate of the lifetime of the plume. The ratio of these two characteristic times is $t_{\rm det}/t_{\rm plume} \sim 10^{-1}$ for the relevant altitudes in Table 5.1. Since the plume timescale is larger than the detection timescale, the same plume could generate considerably different impact rates were LDEX to transit the plume at different times.

We generate simulated plume impact rates as a function of three parameters: φ_0, φ_1, and t_0, the time since the plume was initiated. However, we cannot immediately compare these simulated impact rates to the LDEX data since there is no a priori method to determine the time at which LDEX reached the center of the plume. Therefore, we allow the relative timing between each observed and simulated impact rate to be variable, adding a fourth parameter to the study, $t_{\rm LDEX}$, the elapsed time between the LDEX observed peak and the time at which LDEX crossed over the modeled impact site. We perform a χ^2 minimization on [φ_0, φ_1, t_0, $t_{\rm LDEX}$], with the constraint $\varphi_0 - \varphi_1 \geq 1°$. To compare impact rates, we normalize both the simulated and LDEX impact rates to their peak values, as we aim to compare solely the structure of each plume detection with model data. Additionally, for each detected plume, we generate model plumes with particles that reach their turning points within ±15 km in altitude. This is implemented to increase the statistics of

id	φ_0 [deg]	φ_1 [deg]
A	5	1
B	9	0
C	6	4
D	8	2

Table 5.3: Fit parameters for each plume detection, determined by minimizing χ^2.

the modeled plume by only modeling particles that will significantly contribute to the impact rate. Figures 5.9 to 5.12 show the χ^2 values for each plume. In each case, an absolute minimum in χ^2 is found and an estimate for the angle pairs is given in Table 5.3. Uncertainties in the fit for each of these estimates are approximately 1-2°, however the larger uncertainly based on geometry is discussed below.

5.5 Model Results and Future Work

Figure 5.13 shows the best fit rates for each plume, which have excellent agreement with the LDEX rates. The ejecta cones analyzed in this work (Table 5.3) are considerably narrower than the canonical cone angles used in the literature are $\varphi_0 = 30°$ and $\varphi_1 = 0°$ [50, 42]. Additionally, for three of the four plume detections analyzed in this work, the ejecta cones have an interior region devoid of ejecta particles, in contrast to the literature, which typically assumes $\varphi_1 = 0°$ or $\varphi_0 = \varphi_1$ such that particles only populate the cone's surface.

One explanation for this discrepancy could be the three dimensionality of impact ejecta plume detection. The probability that LDEX flew precisely through the center of the plume is fairly low. Therefore, the angles derived from a 2D fit would be smaller than the true plume's. If θ is the derived angle from the model, for which LDEX transited the plume by a distance b from the center of the plume, the true plume angle φ can be estimated. A diagram for this detection geometry is given in Figure 5.14. With $r/b = \tan\varphi/\tan\theta$,

$$\varphi = \tan^{-1}\left(\frac{\tan\theta}{b/r}\right) \tag{5.5}$$

where r is the maximum radial extent of the plume. Figure 5.15 shows φ as a function of b/r for

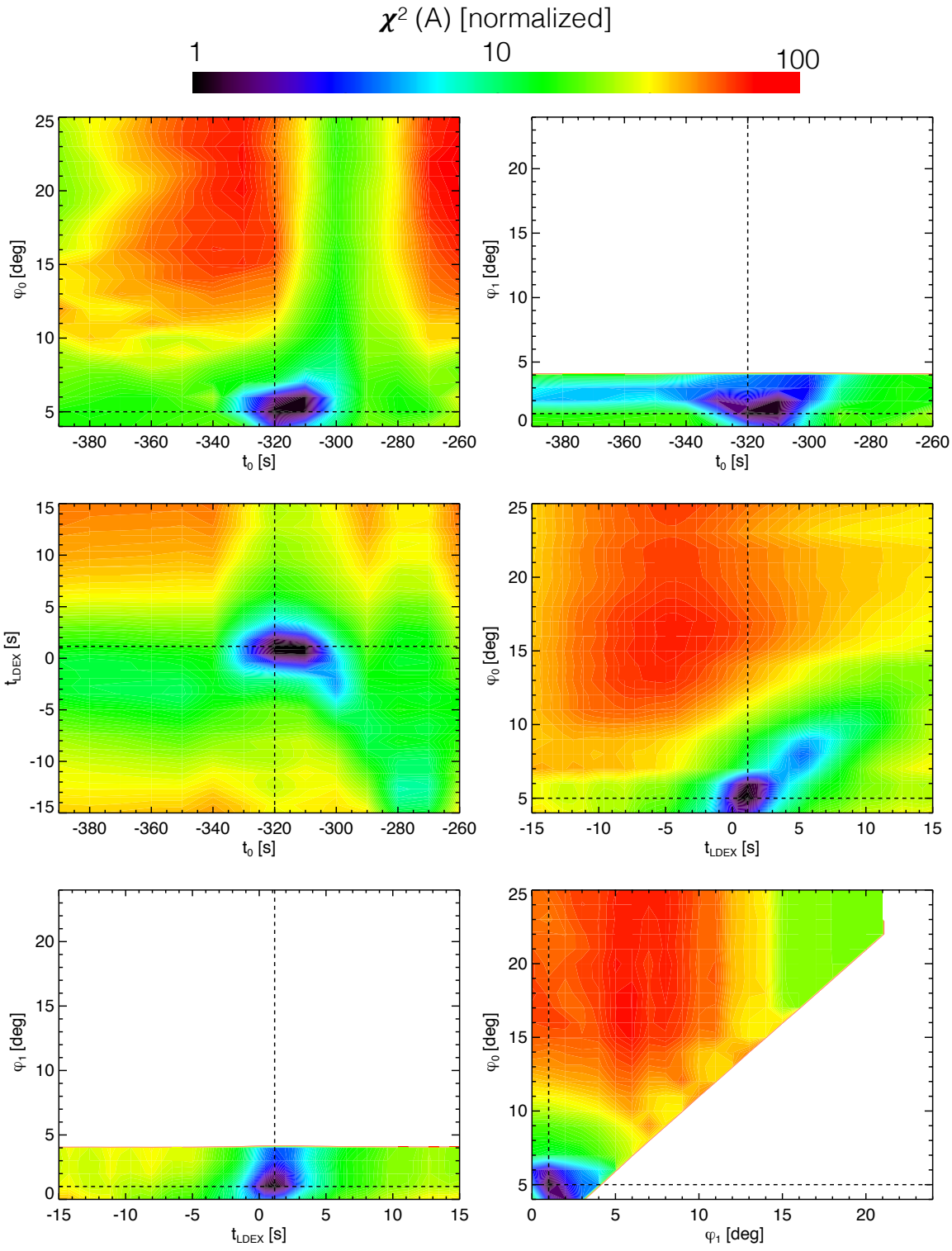

Figure 5.9: χ^2 for plume A. The blank data in 3 of the panels showing φ_1 is due to the constraint $\varphi_1 \leq \varphi_0 + 1^\circ$.

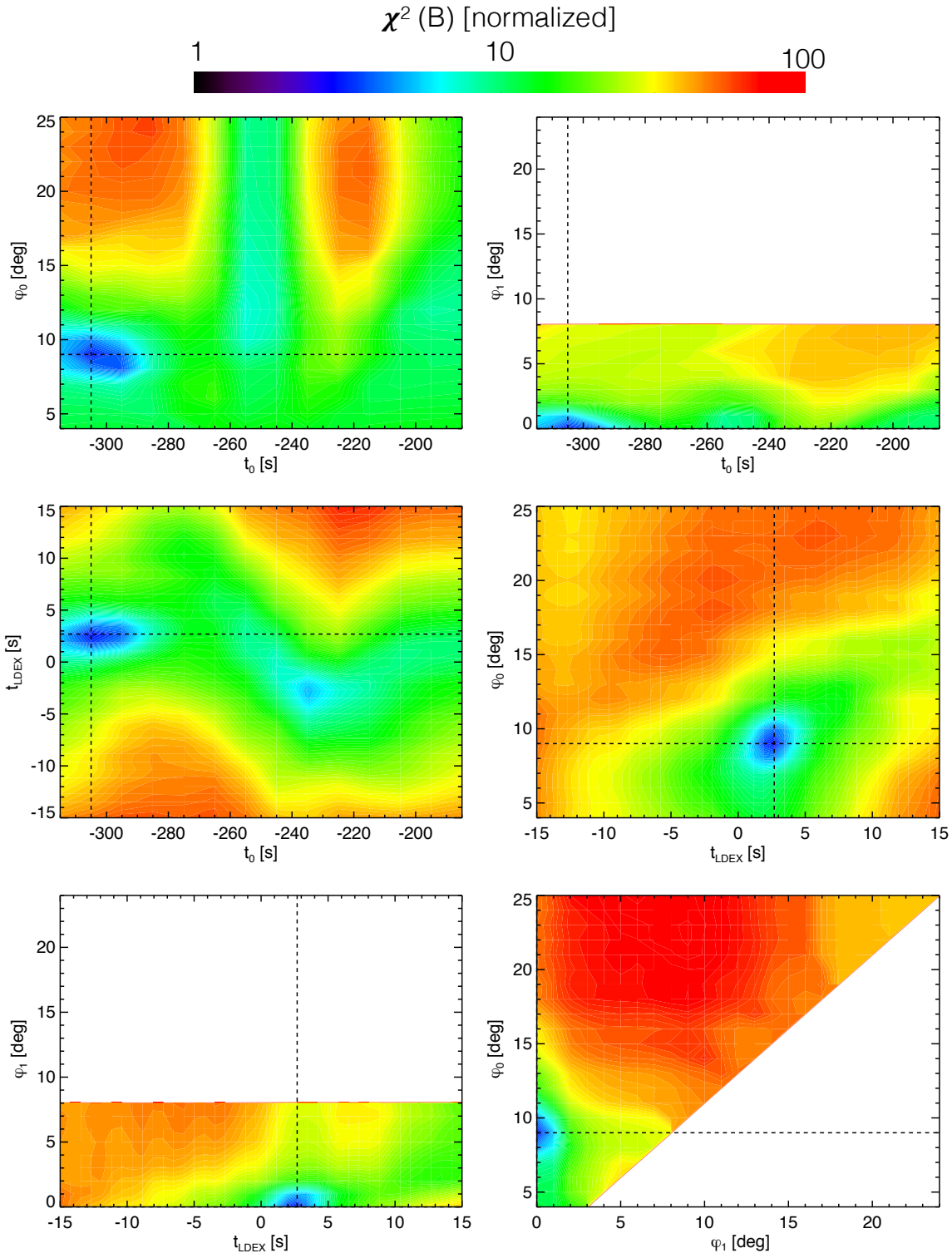

Figure 5.10: χ^2 for plume B. See Figure 5.9 caption for additional description.

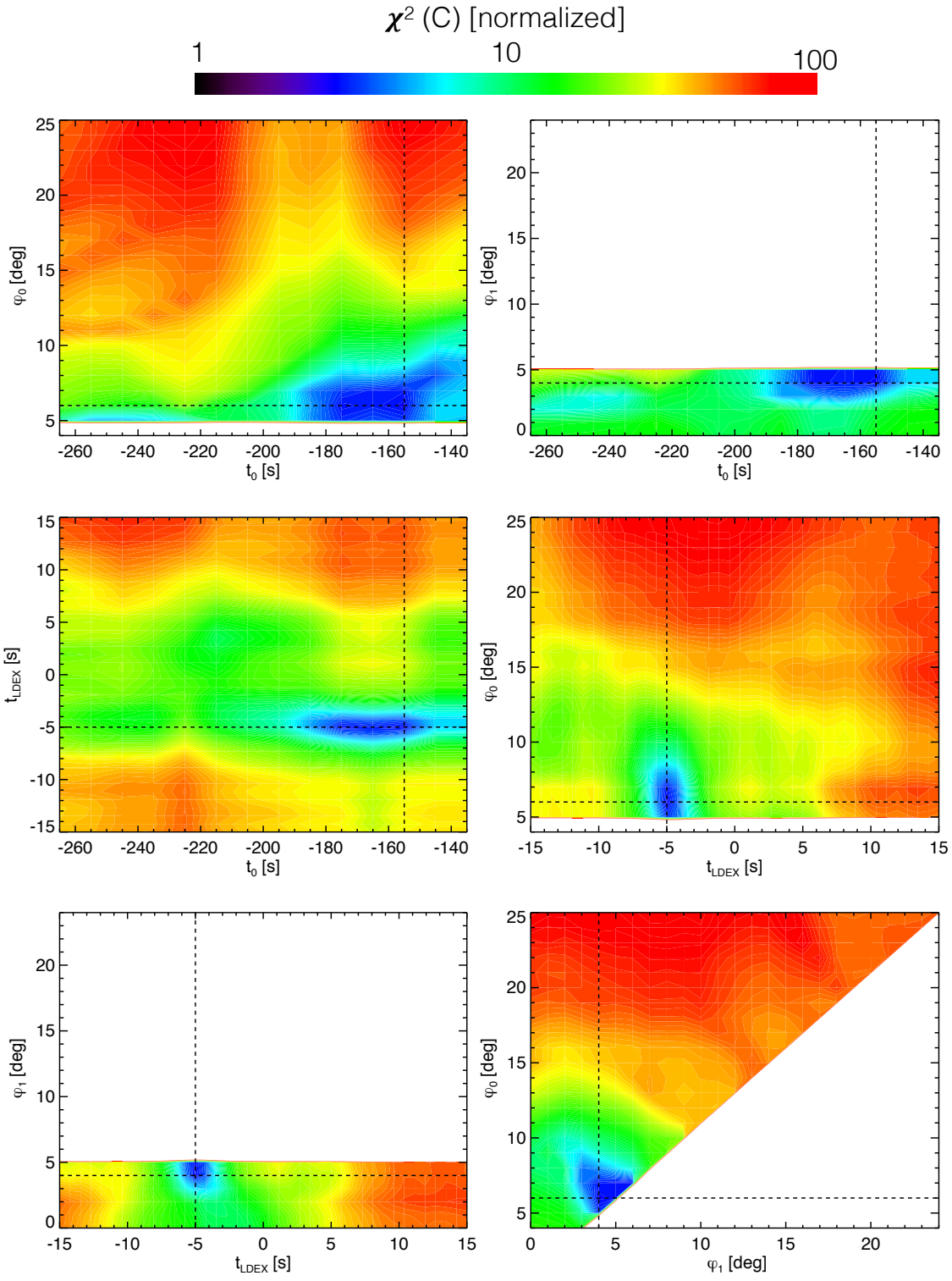

Figure 5.11: χ^2 for plume C. See Figure 5.9 caption for additional description.

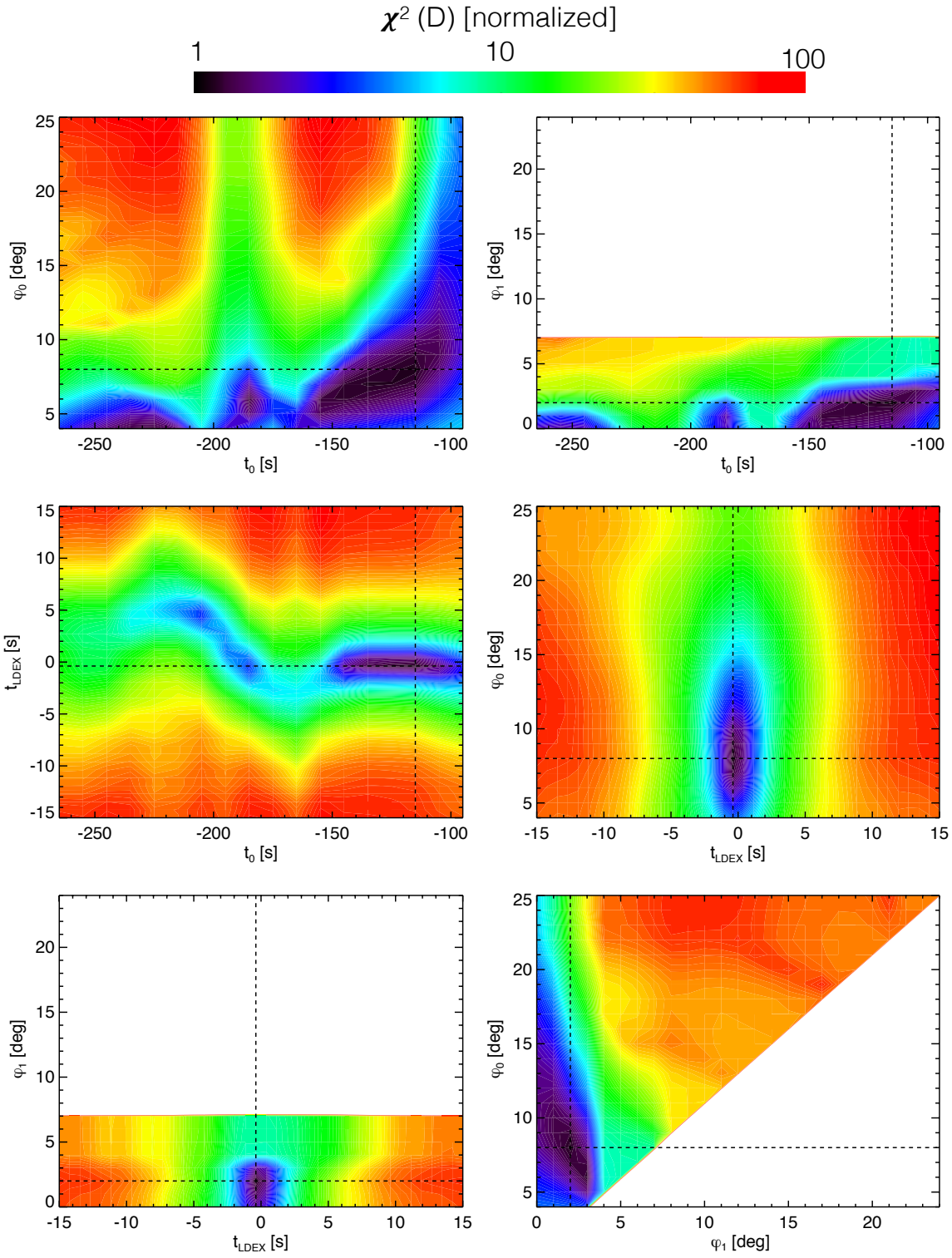

Figure 5.12: χ^2 for plume D. See Figure 5.9 caption for additional description.

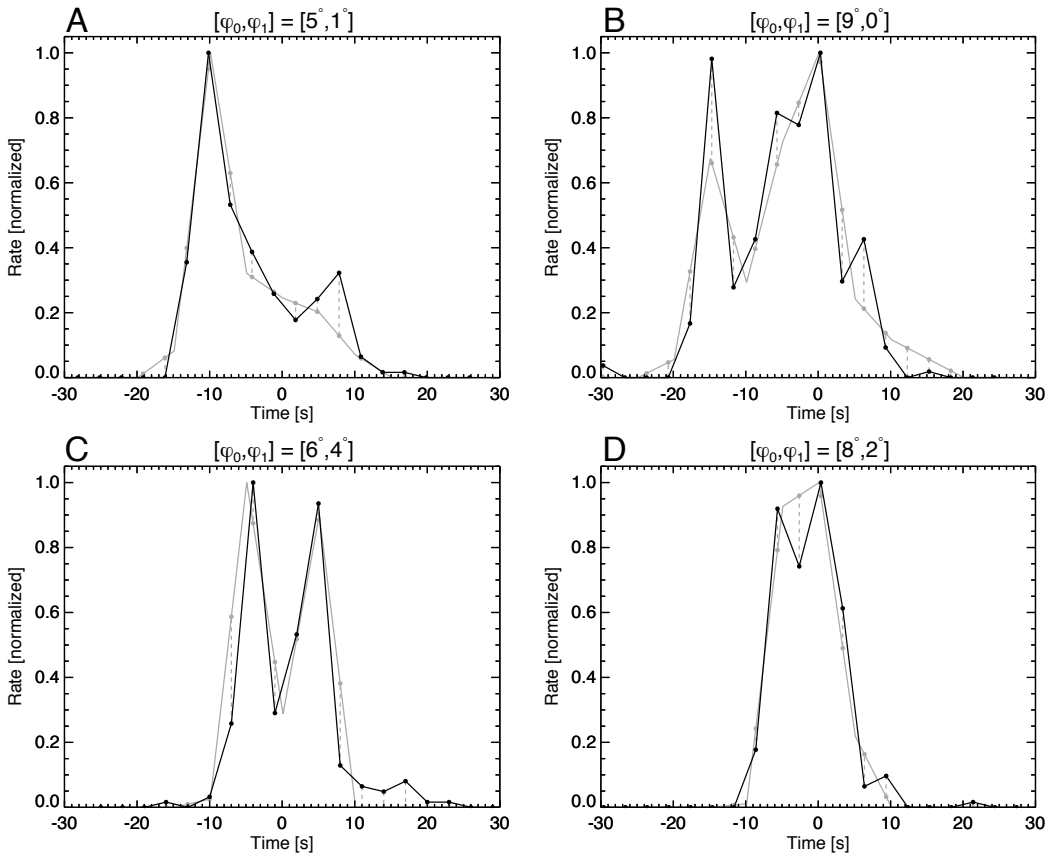

Figure 5.13: The LDEX impact rates (black) shown with their best model fits (gray) for A-D.

each of the four discussed plumes. As shown in this figure, if each of the ejecta plumes detected had an exterior angle of 30°, LDEX would have had to fly through each with an impact parameter ratio of $b/r = 0.7 - 0.95$. For larger b/r values, $A(\omega)$ will decrease due to the transverse horizontal velocities inherent in not flying through the center of the plume. Additionally, large values of b/r will have significantly less number of particles to detect. Therefore, while the distribution of b/r values encountered by LDEX should be uniform, the probability of detecting a plume at large b/r is significantly lower. Hence, we suggest the b/r values in the range of 0-0.5 are more likely than 0.5-1.0. Up to $b/r = 0.5$ the true angle varies from the derived angle by at most 50%, with a maximum exterior angle of 17°. This reinforces the idea that the canonical angle of 30° used in the literature may need revision, as it is highly unlikely all 4 discussed plumes were for $b/r = 0.7 - 0.95$.

Due to the uncertainty in the geometry of each plume detection, additional information must either be assumed or derived from the data. One possible method to further constrain the plume characteristics would be to analyze plumes with smaller than 200 particles. By looking at plumes with at least 75 particles (Figure 5.16), for example, we would be able to study the plume characteristics over a range of altitudes from ∼20-100 km. The relative structure of the plumes at various altitudes shows a trend of increased temporal width with increased altitude, consistent with ejecta plumes which spread radially with altitude. Analysis of the dependence on altitude of the impact rate profiles may allow us to further constrain the properties of these plumes. Furthermore, the bursts in the LDEX data may not represent the nominal plumes generated by sporadic meteoroids and may be generated by unusually energetic primary impactors.

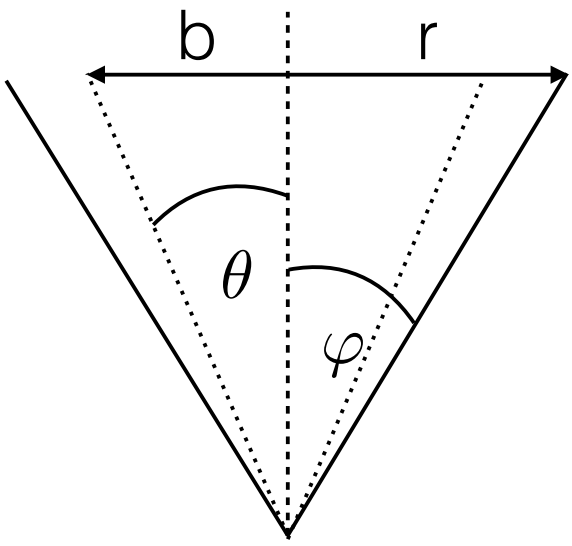

Figure 5.14: Schematic showing the impact parameter b for an impact plume detection with a maximum radial extent of the plume r.

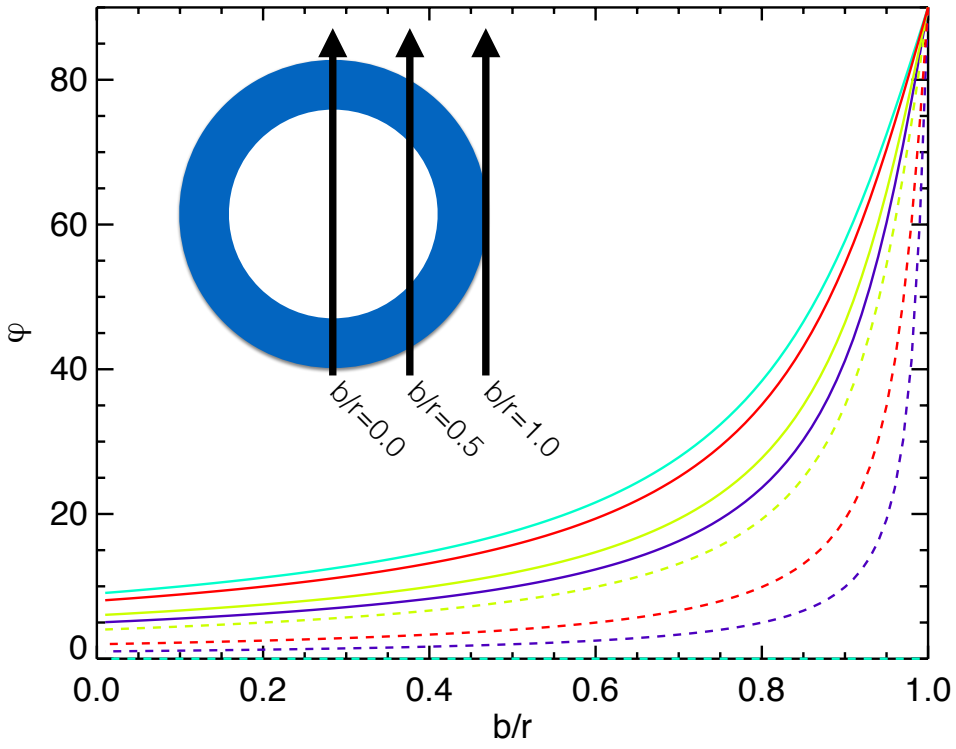

Figure 5.15: The true plume angles as a function of b/r for each measured plume. Purple, green, yellow, and red correspond to plumes A,B,C, and D respectively, with the solid (dotted) lines showing the exterior (interior) angles.

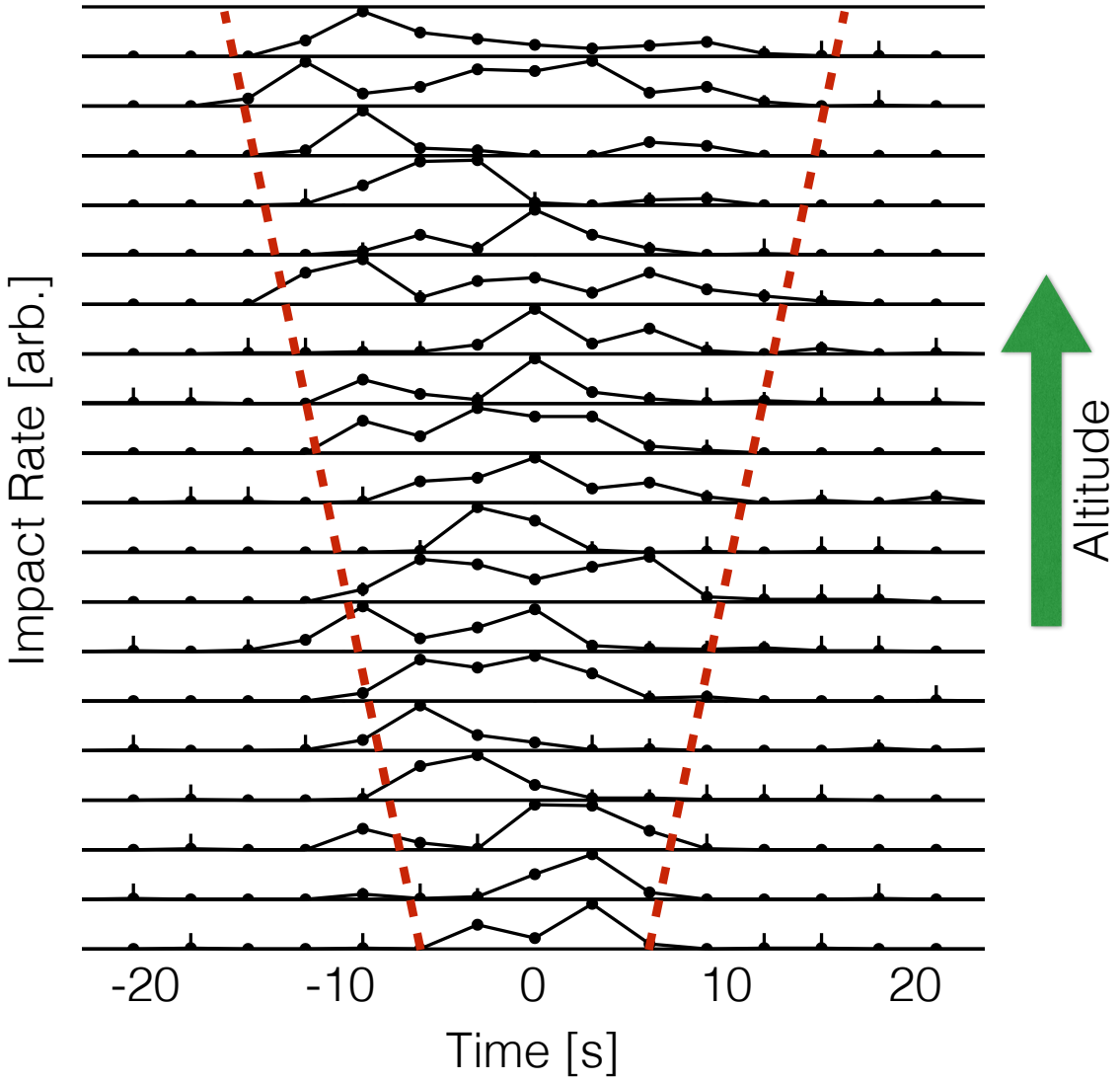

Figure 5.16: Impact rate profiles for all ejecta plume transits detected by LDEX with at least 75 particles. The rates are sorted by altitude, where the bottom rate occurred at 23 km, while the rate at the top of the figure occurred at 92km. The width of the impact rates tends to increase with high altitude detections.

Chapter 6

Electrostatic Dust Lofting

Chapters 3 through 5 focused on the LDEX measurements of the lunar dust cloud. This cloud is sustained by the continual bombardment of the lunar surface with micrometeoroids, which continually eject material into the lunar exosphere. As discussed in the introduction, an additional dense dust population of small ($a \sim 100$ nm) grains has been posited to exist above the lunar terminators. This putative population is suggested to be sustained by electrostatic ejection of tiny grains due to large electric fields that may exist at the lunar terminator. In this chapter, we discuss the LDEX measurements designed to investigate this putative population. Section 6.1 discusses the LDEX data taken near the terminator and gives an upper limit for the density of such a population of small grains. Section 6.2 discusses future lines of study with the LDEX current data.

6.1 Upper Limit on the Density of Small Grains Above the Lunar Terminator

The LDEX current data is used to search for the putative population of small grains near the terminator. Since it did not operate with the Sun in its field-of-view, LDEX made no ram-pointing observations between the lunar sunset terminator at 18:00 LT and the sub-solar point at 12:00 LT during the primary mission. Unless otherwise stated, "terminator" will refer to the lunar sunrise terminator at 6:00 local time (LT). This terminator is the boundary on the lunar surface between sunlit and shadowed terrain assuming a smooth surface, hence ignoring the complexity of this boundary due to the topography. LADEE followed a retrograde, near equatorial orbit with closest approaches over the sunrise terminator. During these closest approaches no direct solar UV

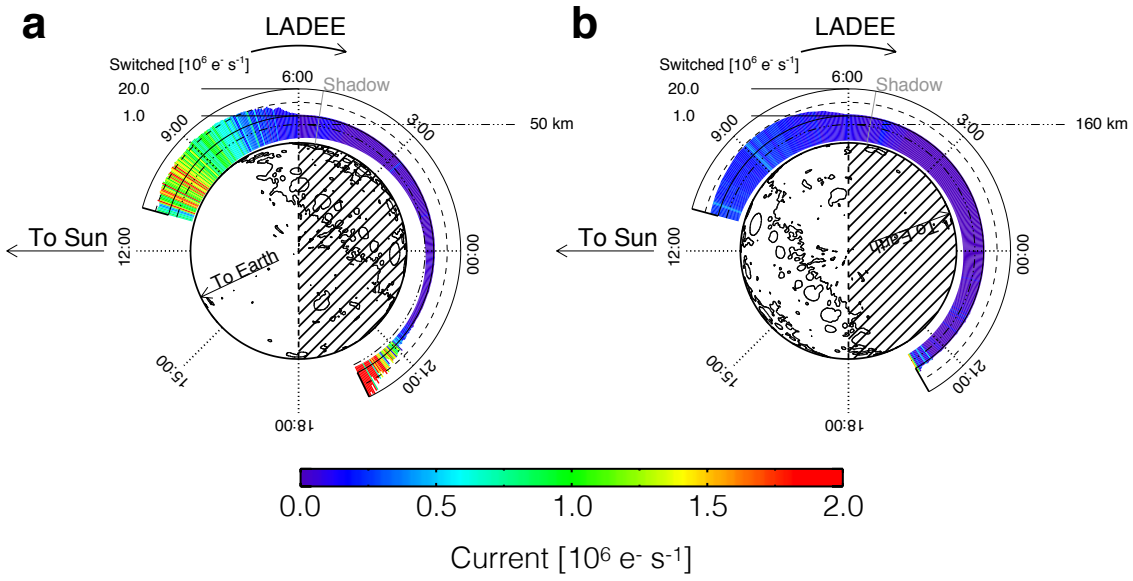

Figure 6.1: The residual, low-energy ion current measured by LDEX, shown in a frame with the Sun fixed on the x-axis. The color indicates the magnitude of the current, the gap between the surface of the moon and the color strip indicates the spacecraft altitude (not to scale), and the radial extent of the color strip shows the magnitude of the switched signal, which gives a measure of the contribution of the UV generated photoelectrons on the MCP itself, and the high energy ions entering LDEX. The times on the circular axis denote local time. **(a)** A representative orbit showing the many features frequently seen by LDEX. This data is the same as shown in Figure 2.6**(b)** A quiet period showing almost no activity on the current channel, observed regularly throughout the mission.

radiation could enter the LDEX field-of-view (FOV), maximizing LDEX's sensitivity to search for small lofted dust grains.

Figure 6.1a shows a typical LDEX current measurement taken during a single orbit. There are many features of note in this representative orbit. From turn on at approximately 10:00 LT (usually in the range of 12:00 to 10:00 LT) to approximately 7:00 LT, LDEX typically measured a large current that decreased as LADEE approached the lunar terminator. This is primarily due to low energy pickup ions from the lunar exosphere entering LDEX's detector [67]. At 6:00 LT LDEX typically measured a very low current on the order of 10^5 $e^- s^{-1}$. Next in the orbit, LDEX frequently measured a small but perceptible increase of current when LADEE entered the lunar optical shadow. This is due to the sudden change in spacecraft charging at this boundary, which causes a change in the spacecraft sheath and subsequent influx of positive ions to LDEX, however the exact details of this specific current remain an ongoing study. After shadow crossing, the current remained low until right before LADEE left the shadow. During many orbits, LDEX frequently measured the influx of ions streaming into the lunar wake just before LADEE left the shadow at approximately 21:00 LT. Figure 6.1b shows an example of an orbit for which LDEX measured very low current, which occurred frequently throughout the mission.

To discuss the putative density of 0.1 μm grains, we focus on the measurements taken near the terminator region, from 5:30 LT to 6:30 LT, which corresponds to $\pm$ 2.5 minutes about the terminator in the LADEE orbit. LADEE covered an altitude range of $\simeq$ 3 - 250 km over the terminator. Figure 6.2 shows the average LDEX current measurements for each terminator crossing, and also the expectation for J, based on previous remote sensing observations. The predicted densities from the Apollo mission [28, 59] and upper limits from the more recent Clementine [27] and LRO [23] missions are given by an exponential distribution of the form $n(z) = n_0 e^{-z/z_0}$ where z is the altitude and z_0 is the scale height. Values used for each estimates are given in Table 6.1.

For each dust density estimate, a predicted LDEX current is calculated $J = nAvq$, where A is the LDEX sensitive area (7.6×10^{-3} m^{-2} at normal incidence, including a factor of 0.9^3 for the 3 entrance grids [41]), v is the dust impact velocity onto LDEX, and q is the impact charge generated

Table 6.1: Terminator density parameters for $a = 0.1$ μm along with the expected currents LDEX would measure for such a population at LDEX's lowest terminator crossing altitude of 3 km. The last row gives the average current measured by LDEX, which remained approximately constant throughout the mission.

Source	n_0 $[\mathrm{m}^{-3}]$	z_0 [km]	$J(3$ km$)$ $[e^{-}\mathrm{s}^{-1}]$
[59]	6×10^4	9.3	6×10^7
[28]	3×10^4	8.5	3×10^7
[27]	9	12.0	9×10^3
[23]	5	9.0	5×10^3
LADEE/LDEX			1×10^5

by a 0.1 μm grain (approximately 100 electrons). The true spacecraft velocity is used to determine the density upper limit for each terminator crossing data point. At the lowest altitudes (< 10 km), the current is approximately two to three orders of magnitude lower than the current predicted by the Apollo measurements. Were LDEX to encounter a population of small grains with the expected Apollo inferred density [59], LDEX would have measured a current on the order of 10^7 $e^{-}s^{-1}$ and the region near the terminator would be bright red in Figure 6.1. With an approximately constant terminator current of 10^5 $e^{-}s^{-1}$, this puts a strict upper limit on the putative number density of smalls grains at 10^2 m^{-3} throughout all measured altitudes.

The LDEX current measurements at the terminator follow the solar wind ion density, as measured by ARTEMIS [2], with a correlation coefficient between the two measurements of 0.64. Figure 6.2 shows the ARTEMIS measured ion density during LDEX's operational period. It is not immediately clear how the solar wind ion density influences the LDEX terminator current measurements. During terminator crossings, LDEX is pointed in a direction anti-parallel to the solar wind flow and should not detect any solar wind ions. However, the correlation between the solar wind ion density and the LDEX current measurements indicates some additional plasma contribution to J. Hence, the possible subtraction of this contamination source will only further reduce the already low upper limit on the lofted dust density.

Figure 6.3 shows the dust density upper limits, including the subset of the observations taken during the periods when the Moon was in Earth's magnetotail, shielded from the solar wind. The lack of altitude dependence of the dust density upper limits and correlation with the solar wind ion density indicates that low energy ions are likely to be major contributors to J, and the lofted dust densities are even smaller than reported here.

LDEX's current measurement corresponds to an upper limit on the dust number density of $n_d < 100$ m^{-3} at an altitude of 3 km above the surface while the Moon is the solar wind, and $n_d < 40$ m^{-3} during its passage through the geotail, approximately two to three orders of magnitude below the expectations based on Apollo observations. This indicates that the anticipated electrostatic lofting mechanism is not operating on the lunar surface due to the lack of sufficiently strong electric fields and/or sufficiently large electrostatic charges on the small dust grains on the surface to overcome the cohesive forces acting between regolith particles [40]. However, such processes could still be at work if the resulting dust mobilization and transport remain confined close to the surface, below 3 km.

6.2 Future Work

The current that LDEX measured is most likely due to the presence of low energy ions and possibly energetic neutral atoms in the lunar environment. Figure 6.4 shows the LDEX current for one orbit along with the dot product between the LDEX boresight vector and the convection electric field vector, which is derived from ARTEMIS data. During the time LDEX was taking measurements before LADEE crossed into the Moon's umbral shadow, the cross correlation coefficient between the two is 0.95. Due to the high correlation, it is likely LDEX is measuring pickup ions in the lunar exosphere, which are swept into the detector by the convection electric field of the solar wind shortly after ionization, hence their low energies. Using contemporary plasma measurements by the ARTEMIS spacecraft [2], combined with improved modeling of the behavior of low energy ions within LDEX, will lead to a better estimate of their contribution in this measurement and further decrease the upper limit on the density small dust grains above the lunar terminator.

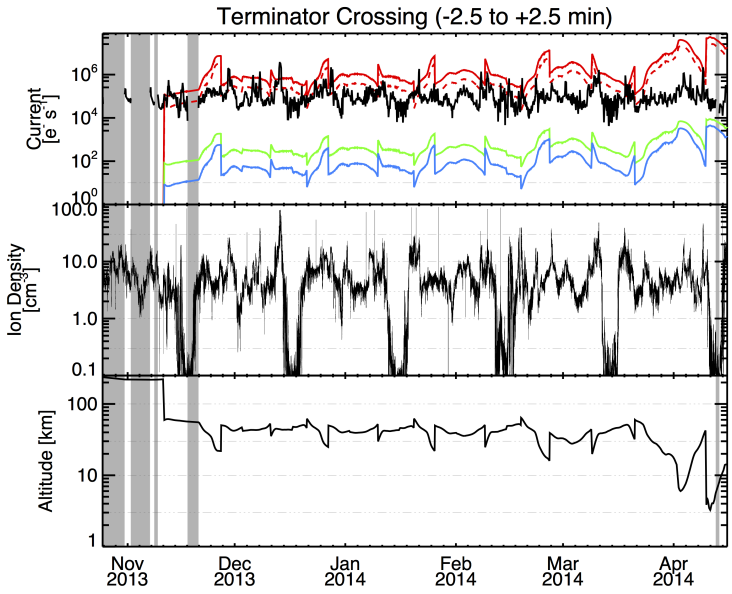

Figure 6.2: (*top:*) The LDEX current for each terminator crossing, averaged from 5:30 LT to 6:30 LT, and the predicted currents based on the Apollo [59, 28] (red and dashed red, respectively), Clementine [27] (green), and LRO [23] (blue) missions. (*middle:*) The solar wind ion density at the Moon measured by ARTEMIS [2]. (*bottom:*) The altitude of the spacecraft at each terminator crossing. Gray vertical bars indicate time periods LDEX was not taking measurements.

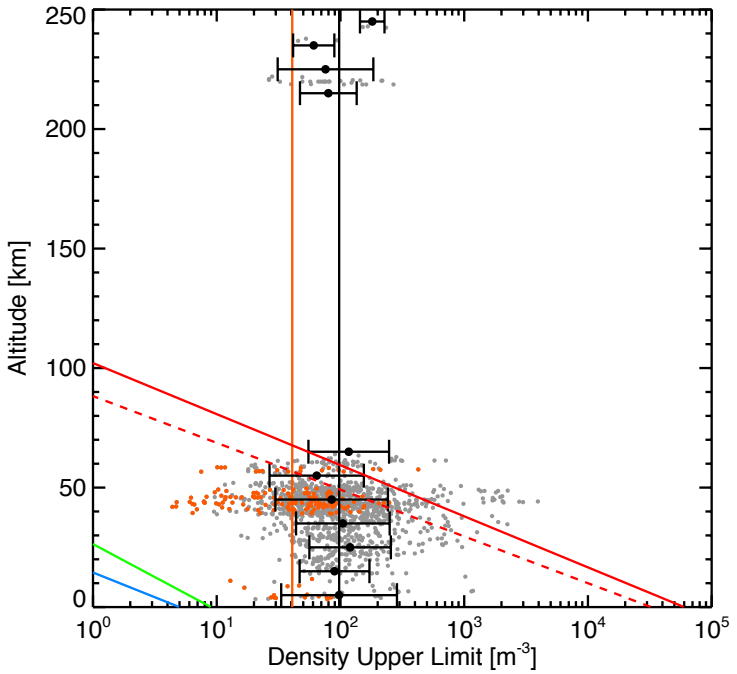

Figure 6.3: The upper limit of the density of dust particles as a function of altitude, derived from the LDEX current measurements (Figure 6.2). Each gray dot represents a terminator crossing. Black dots show the the averages in 10 km increments. The orange points indicate LDEX measurements taken in Earth's magnetotail.

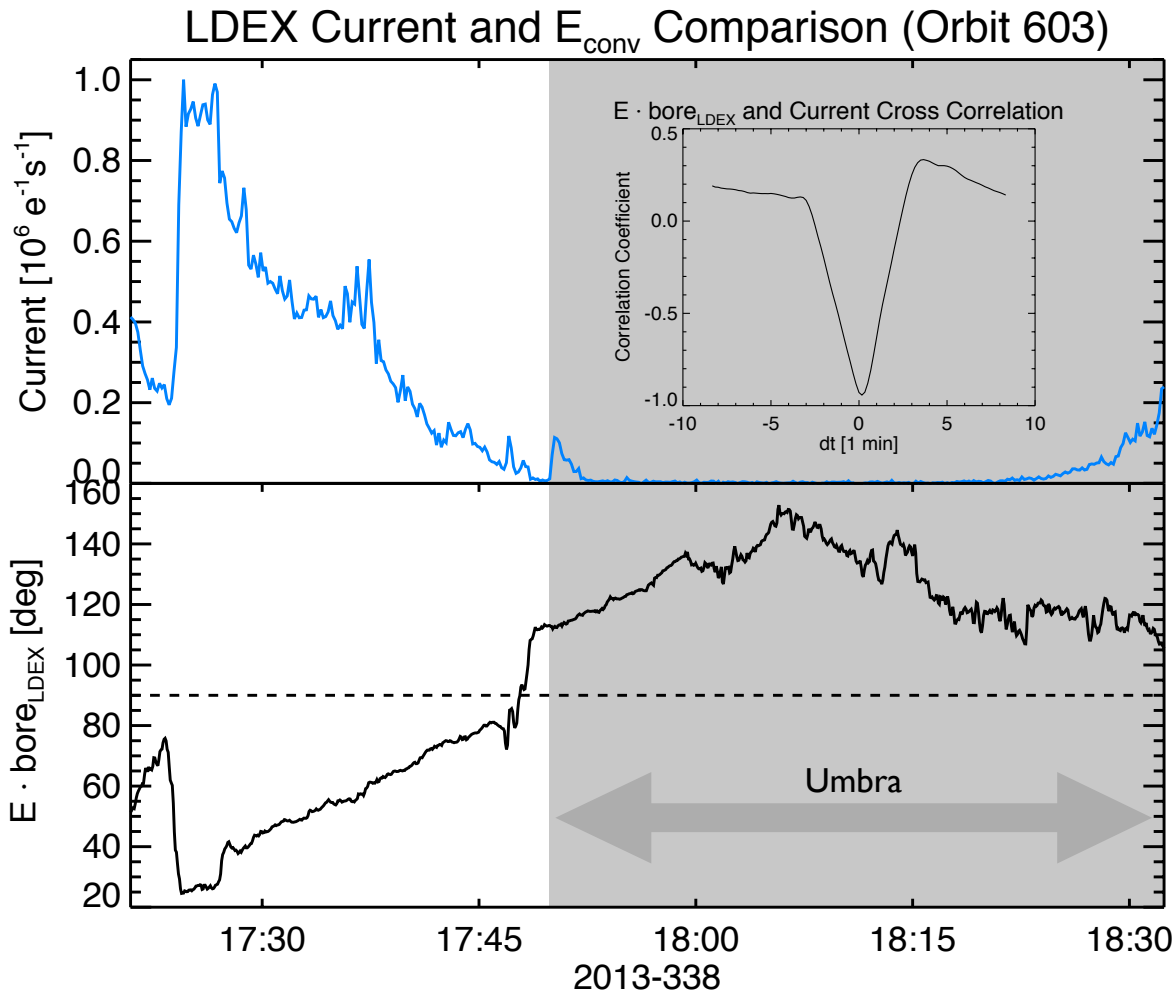

Figure 6.4: Top: The LDEX current for a single orbit (603). Bottom: the dot product between the LDEX boresight vector and the electric convection electric field vector, as determined by ARTEMIS. The gray area indicates when LADEE was in the Moon's umbral shadow and the smaller panel in the top shows the cross correlation coefficient between the current and the dot product during the non-umbral times.

Chapter 7

Conclusion

This thesis has investigated the characteristics of the lunar dust cloud, an environment which has been relatively unconstrained until the LADEE mission. The study was motivated by two main science questions:

1) What are the characteristics of the lunar dust cloud and how does it respond to the influx of meteoroids bombarding the surface?

2) Is there evidence of electrostatically lofted dust above the lunar terminator?

7.1 Lunar Dust Ejecta Cloud

To investigate question 1), we first characterize the bulk properties of the lunar dust cloud and analyze its steady state on the timescale of months. The mass distribution of the lunar dust cloud was measured and found to be relatively constant throughout the mission, informing us on the size distribution of grains gardening the lunar surface.

The lunar dust cloud was found to have a peak density on its apex side, canted towards the Sun. We find the dust cloud density profile to be in very good agreement with the sum of three known sporadic meteoroid sources (HE, AP, and AH). By fitting the cloud profile to the response of these three sources, we find the HE and AP sources to dominate over the AH source, which is qualitatively consistent with ground based measurements and explains the sunward cant. Of the two dominant sources, the AP source is primarily responsible for the ejecta production at the Moon

due to its large relative velocity and power law dependence on velocity in the mass production, generating the most impact ejecta around 6 LT.

We also find the lunar dust cloud density to wax and wane with lunar phase, peaking during the Moon's waning gibbous phase. This observation is an independent validation of the relative weakness of the AH source during the discussed measurement period. Were LDEX to have operated in July, when the AH source is observed to be five times stronger than the HE source [12], we suggest the lunar dust cloud density would have peaked towards the anti-helion direction.

After analyzing the global characteristics of the lunar dust cloud on long timescales, we explore its transient characteristics. Using Poisson statistical methods to quantitatively identify unusual periods in the LDEX impact rate data, a method similar to the analysis of lunar seismic data [64] is proposed to characterize meteoroid streams. By analyzing the distribution of right ascension and declinations of groupings of impacts, the radiant for a strong and established meteoroid stream (the Geminids) was successfully reproduced within 1σ error. Partial radiants and/or peak times are correctly estimated for 4 other meteoroid streams. An unidentified meteoroid stream was potentially observed by LDEX. Using the methods outlined therein, an estimate for the radiant of this putative stream is calculated as (RA, δ) = (268$\pm$41°, -22$\pm$13°), with a peak solar longitude of $\lambda = 4.1\pm0.3°$. While LDEX observed a handful of dense ejecta plumes during this period, the rate of detected bursts was not significantly higher than the sporadic background.

We then investigated the LDEX data on the shortest timescale available, single ejecta plumes. We identified 4 very large impact rate enhancements and interpret them to be plume detections. Each plume detection has appreciable structure in the LDEX impact rate time series. To understand the detection geometry of a plume transit, we developed a Monte Carlo model of impact ejecta plumes. By studying their dynamics and simulating LDEX flying through model plumes, we are able to fit the LDEX plume detections to model plumes. The plumes which are most consistent with the LDEX data are all significantly narrower in angular extent than the 30° canonical values used in the literature [50, 42]. The geometry of each transit may have bearing on this discrepancy and we outline future lines of study in this topic.

7.2 Electrostatic Lofting

To address question 2), we analyzed LDEX current data designed to search for an abundance of small grains. The LDEX in-situ dust measurements over the lunar sunrise terminator were taken in the altitude range of $\simeq$ 3 - 250 km. LDEX searched for the putative high-density population of small grains through their cumulative contribution to the current it recorded. LDEX's current measurement of $\approx 10^5\ e^- s^{-1}$ corresponds to an upper limit on the dust number density of $n_d < 100$ m^{-3} at an altitude of 3 km above the surface while the Moon is the solar wind, and $n_d < 40$ m^{-3} during its passage through the geotail, approximately two to three orders of magnitude below the expectations based on Apollo observations. This indicates that the anticipated electrostatic lofting mechanism is not operating on the lunar surface due to the lack of sufficiently strong electric fields and/or sufficiently large electrostatic charges on the small dust grains on the surface to overcome the cohesive forces acting between regolith particles [40]. However, such processes could still be at work if the resulting dust mobilization and transport remain confined close to the surface, below 3 km.

We found the current LDEX measured is most likely due to the presence of low energy ions and possibly energetic neutral atoms in the lunar environment. Further constraining these sources and how they contribute to the LDEX current will only continue to lower the already small upper limit on the putative population of small grains above the lunar terminator.

7.3 Summary

Our understanding of the lunar dust environment has been significantly improved by the data taken by LDEX. Not only did LDEX successfully characterize the lunar dust environment and determined that there is no evidence for an electrostatically levitated dust population, it also proved dust detectors have many far reaching applications. While the additional plasmas sources LDEX detected are "noise" with respect to dust measurements, they provide a proof-of-concept that LDEX and therefore any impact ionization dust detector can be used as a plasma detector as

well. With plasma detection modes in mind during the design phase, future dust detectors may be able to characterize both the dust and plasma environment of their surroundings in a manner complementary to traditional plasma instruments.

Additionally, detecting and measuring the orbital properties of meteoroid streams is currently undertaken via multiple methods, each with its own strengths and weaknesses. The meteoroid stream characterization outlined in this work provides a novel method to measure the local meteoroid environment using the Moon as large surface area dust detector, by exploiting the large magnification factor in the density of the ejecta plumes. We are also able to constrain relative fluxes of the sporadic background sources, a topic which is still highly in debate due to the difficulties of such a measurement. Future longer duration lunar missions carrying an LDEX type instrument, and following orbits with higher inclinations than LADEE could greatly enhance our knowledge about the meteoroid environment at 1 AU in a manner unique to dust detectors. An LDEX type instrument sent to any airless body in the solar system would gather critical information about its local meteoroid environment, and potentially its plasma environment.

Bibliography

[1] F Allegrini, M A Dayeh, M I Desai, H O Funsten, S A Fuselier, P H Janzen, D J McComas, E Möbius, D B Reisenfeld, D F Rodríguez M, N Schwadron, and P Wurz. Lunar energetic neutral atom (ENA) spectra measured by the interstellar boundary explorer (IBEX). Planetary and Space Science, 85(c):232–242, September 2013.

[2] V. Angelopoulos. The ARTEMIS Mission. Space Science Reviews, 165:3–25, December 2011.

[3] S. Auer and K. Sitte. Detection technique for micrometeoroids using impact ionization. Earth and Planetary Science Letters, 4:178, April 1968.

[4] Geert Barentsen and Dusty Lefevre. Interactive 3D visualization of the Geminid meteoroid stream. In Proceedings of the International Meteor Conference, pages 71–75. Volkssterrenwacht Urania, Mattheessensstraat 60, 2540 Hove, Belgium. gbar@urania.be, December 2007.

[5] O. E. Berg, H. Wolf, and J. Rhee. Lunar soil movement registered by the Apollo 17 cosmic dust experiment. In H. Elsaesser and H. Fechtig, editors, Interplanetary Dust and Zodiacal Light, volume 48 of Lecture Notes in Physics, Berlin Springer Verlag, pages 233–237, 1976.

[6] Otto E Berg. Lunar Terminator Configuration. Earth and Planetary Science Letters, 39(3):377–381, 1978.

[7] T Birnstiel, H Klahr, and B Ercolano. A simple model for the evolution of the dust population in protoplanetary disks. Astronomy and Astrophysics, 539:A148–12, March 2012.

[8] Peter Brown, Robert Weryk, D K Wong, and J Jones. A meteoroid stream survey using the Canadian Meteor Orbit Radar. I. Methodology and radiant catalogue. Icarus, 195(1):317–339, May 2008.

[9] E. Buhl, F. Sommer, M. H. Poelchau, G. Dresen, and T. Kenkmann. Ejecta from experimental impact craters: Particle size distribution and fragmentation energy. Icarus, 237:131–142, July 2014.

[10] M Campbell-Brown. High resolution radiant distribution and orbits of sporadic radar meteoroids. Icarus, 196(1):144–163, July 2008.

[11] M. D. Campbell-Brown. High resolution radiant distribution and orbits of sporadic radar meteoroids. Icarus, 196:144–163, July 2008.

[12] Margaret Campbell-Brown and J Jones. Annual variation of sporadic radar meteor rates. Monthly Notices of the Royal Astronomical Society, 367(2):709–716, April 2006.

[13] Margaret Campbell-Brown and J Jones. Annual variation of sporadic radar meteor rates. Monthly Notices of the Royal Astronomical Society, 367(2):709–716, April 2006.

[14] G R Carruthers and T D Seeley. Global Imaging Monitor of the Ionosphere (GIMI): a far-ultraviolet imaging experiment on ARGOS. SPIE's 1996 ..., 1996.

[15] A. Colaprete and *et al.* The ladee ultaviolet/visible spectrometer. Space Sci. Rev., 185:63 – 91, 2014.

[16] A. Collette, Z. Sternovsky, and M. Horányi. Production of neutral gas by micrometeoroid impacts. Icarus, 227:89–93, January 2014.

[17] J. E. Colwell, M. Horanyi, S. Robertson, X. Wang, A. Haugsjaa, and P. Wheeler. Behavior of Charged Dust in Plasma and Photoelectron Sheaths. Dust in Planetary Systems, 643:171–175, January 2007.

[18] W. Cooke and D. Moser. The 2014 meteor shower activity forecast for earth orbit. 2013.

[19] H. Dietzel, G. Eichhorn, H. Fechtig, E. Grun, H.-J. Hoffmann, and J. Kissel. The HEOS 2 and HELIOS micrometeoroid experiments. Journal of Physics E Scientific Instruments, 6:209–217, March 1973.

[20] V. Dikarev, E. Grün, J. Baggaley, D. Galligan, M. Landgraf, and R. Jehn. The new ESA meteoroid model. Advances in Space Research, 35:1282–1289, 2005.

[21] G. Drolshagen. Comparison of meteoroid models. Report 24.1, Inter-Agency Space Debris Coordination Committee (IADC), 2009.

[22] R. C. Elphic, G. T. Delory, B. P. Hine, P. Mahaffy, M. Horanyi, A. Colaprete, M. Benna, and S. Noble. The lunar atmosphere and dust environment explorer mission. Space Science Reviews, 185:3–25, 2014.

[23] P. D. Feldman, D. A. Glenar, T. J. Stubbs, K. D. Retherford, G. Randall Gladstone, P. F. Miles, T. K. Greathouse, D. E. Kaufmann, J. W. Parker, and S. Alan Stern. Upper limits for a lunar dust exosphere from far-ultraviolet spectroscopy by lro/lamp. Icarus, 233:106–113, May 2014.

[24] K Fox, Iwan P Williams, and David W Hughes. The evolution of the orbit of the Geminid meteor stream. Monthly Notices of the Royal Astronomical Society, 200:313–324, July 1982.

[25] K Fox, Iwan P Williams, and David W Hughes. The rate profile of the Geminid meteor shower. Monthly Notices of the Royal Astronomical Society (ISSN 0035-8711), 205:1155–1169, December 1983.

[26] D. E. Gault. Displaced mass, depth, diameter, and effects of oblique trajectories for impact craters formed in dense crystalline rocks. Moon, 6:32–44, January 1973.

[27] D. A. Glenar, T. J. Stubbs, M. Hahn, and Y. Wang. Search for a high altitude lunar dust exosphere using Clementine navigational star tracker measurements. Journal of Geophysical Research, 119:2548 – 2567, 2014.

[28] D. A. Glenar, T. J. Stubbs, J. E. McCoy, and R. R. Vondrak. A reanalysis of the Apollo light scattering observations, and implications for lunar exospheric dust. Planetary and Space Science, 59:1695–1707, November 2011.

[29] A.L. Graps, E. Grün, H. Svedhem, H. Krüger, M. Horányi, A. Heck, and S. Lammers. Io as a source of the jovian dust streams. Nature, 405:48–50, 2000.

[30] J. Greaves. Four IAU MDC Working List Meteor Showers confirmed via SonotaCo Network Japan data. WGN, Journal of the International Meteor Organization, 40:53–58, April 2012.

[31] E. Gruen, H. Fechtig, J. Kissel, D. Linkert, D. Maas, J. A. M. McDonnell, G. E. Morfill, G. Schwehm, H. A. Zook, and R. H. Giese. The ULYSSES dust experiment. Astronomy & Astrophysics, 92:411–423, January 1992.

[32] E. Grün, H. Fechtig, M. S. Hanner, J. Kissel, B.-A. Lindblad, D. Linkert, D. Maas, G. E. Morfill, and H. A. Zook. The Galileo Dust Detector. Space Science Reviews, 60:317–340, 1992.

[33] E. Grün and M. Horányi. A new look at Apollo 17 LEAM data: Nighttime dust activity in 1976. Planetary and Space Science, 89:2–14, December 2013.

[34] E. Grün, H. A. Zook, H. Fechtig, and R. H. Giese. Collisional balance of the meteoritic complex. Icarus, 62:244–272, May 1985.

[35] E. Grün, H.A. Zook, H. Fechtig, and R.H. Giese. Collisional balance of the meteoritic complex. Icarus (ISSN 0019-1035), vol.62, May 1985, p.244-272., 62:244–272, 1985.

[36] Eberhard Grün and Mihály Horányi. Planetary and Space Science. Planetary and Space Science, 89:1–13, November 2013.

[37] Eberhard Grün, Herbert A Zook, M Baguhl, A Balogh, S J Bame, H Fechtig, R Forsyth, M S Hanner, M Horanyi, J Kissel, B A Lindblad, D Linkert, G Linkert, I Mann, J A M McDonnell, Gregor E Morfill, J L Phillips, C Polanskey, G Schwehm, N Siddique, P Staubach, J Svestka, and A Taylor. Discovery of Jovian dust streams and interstellar grains by the ULYSSES spacecraft. Nature (ISSN 0028-0836), 362(6419):428–430, April 1993.

[38] Dong Han, Andrew R Poppe, Marcus Piquette, Eberhard Grün, and M Horanyi. Constraints on dust production in the Edgeworth-Kuiper Belt from Pioneer 10 and New Horizons measurements. Geophysical Research Letters, 38(2):24102–, December 2011.

[39] W. K. Hartmann. Impact experiments. I - Ejecta velocity distributions and related results from regolith targets. Icarus, 63:69–98, July 1985.

[40] C. M. Hartzell, X. Wang, D. J. Scheeres, and M. Horányi. Experimental demonstration of the role of cohesion in electrostatic dust lofting. Geophys. Rev. Lett., 40:1–5, 2013.

[41] M. Horányi, Z. Sternovsky, M. Lankton, C. Dumont, S. Gagnard, D. Gathright, E. Grün, D. Hansen, D. James, S. Kempf, B. Lamprecht, J. Szalay, R. Srama, and G. Wright. The Lunar Dust Experiment (LDEX) onboard the Lunar Atmosphere and Dust Environment Explorer (LADEE) mission. Space Science Reviews, 185:93 – 113, 2014.

[42] M. Horányi, J. Szalay, S. Kempf, J. Schmidt, E. Grün, R. Srama, and Z. Sternovsky. A permanent, asymmetric dust cloud around the Moon. Nature, 522(7556), 2015.

[43] H. Iglseder, K. Uesugi, and H. Svedhem. Cosmic dust measurements in lunar orbit. Advances in Space Research, 17:177–182, 1996.

[44] D Janches, S Close, J L Hormaechea, N Swarnalingam, A Murphy, D O'Connor, B Vandepeer, B Fuller, D C Fritts, and C Brunini. THE SOUTHERN ARGENTINA AGILE METEOR RADAR ORBITAL SYSTEM (SAAMER-OS): AN INITIAL SPORADIC METEOROID ORBITAL SURVEY IN THE SOUTHERN SKY. The Astrophysical Journal, 809(1):1–16, August 2015.

[45] D Janches, Michael C Nolan, David D Meisel, John D Mathews, Qihou H Zhou, and D E Moser. On the geocentric micrometeor velocity distribution. Journal of Geophysical Research-Space Physics, 108(A):1222, June 2003.

[46] Peter Jenniskens. Meteor stream activity I. The annual streams. Astronomy and Astrophysics 287, 287:990–1013, July 1994.

[47] J Jones and Peter Brown. Sporadic meteor radiant distributions - Orbital survey results. Monthly Notices of the Royal Astronomical Society, 265:524, December 1993.

[48] A King. An ephemeris of the Geminid radiant-point. Monthly Notices of the Royal Astronomical Society, 1926.

[49] D. Koschny and E. Grün. Impacts into Ice-Silicate Mixtures: Ejecta Mass and Size Distributions. Icarus, 154:402–411, December 2001.

[50] A. V. Krivov, M. Sremčević, F. Spahn, V. V. Dikarev, and K. V. Kholshevnikov. Impact-generated dust clouds around planetary satellites: spherically symmetric case. Planetary and Space Science, 51:251–269, March 2003.

[51] H. Krüger, A. V. Krivov, and E. Grün. A dust cloud of Ganymede maintained by hypervelocity impacts of interplanetary micrometeoroids. Planetary and Space Science, 48:1457–1471, December 2000.

[52] H. Krüger, A.A. Krivov, D.P. Hamilton, and E. Grün. Detection of an impact-generated dust cloud around ganymede. Nature, 399:558–560, 1999.

[53] Harold F Levison, Katherine A Kretke, and Martin J Duncan. Growing the gas-giant planets by the gradual accumulation of pebbles. Nature, 524(7565):322–324, August 2015.

[54] J. F. Lindsay. Lunar Stratigraphy and Sedimentology. Elsevier, 1976.

[55] S G Love and D E Brownlee. A Direct Measurement of the Terrestrial Mass Accretion Rate of Cosmic Dust. Science, 262(5133):550–553, October 1993.

[56] P. R. Mahaffy, R. Richard Hodges, M. Benna, T. King, R. Arvey, M. Barciniak, M. Bendt, D. Carigan, T. Errigo, D. N. Harpold, V. Holmes, C. S. Johnson, J. Kellogg, P. Kimvilakani, M. Lefavor, J. Hengemihle, F. Jaeger, E. Lyness, J. Maurer, D. Nguyen, T. J. Nolan, F. Noreiga, M. Noriega, K. Patel, B. Prats, O. Quinones, E. Raaen, F. Tan, E. Weidner, M. Woronowicz, C. Gundersen, S. Battel, B. P. Block, K. Arnett, R. Miller, C. Cooper, and C. Edmonson.

The Neutral Mass Spectrometer on the Lunar Atmosphere and Dust Environment Explorer Mission. Space Sci. Rev., 185:27 – 61, 2014.

[57] C. B. Markwardt. Non-linear Least-squares Fitting in IDL with MPFIT. In D. A. Bohlender, D. Durand, and P. Dowler, editors, Astronomical Data Analysis Software and Systems XVIII, volume 411 of Astronomical Society of the Pacific Conference Series, page 251, September 2009.

[58] A. McBeath. International Meteor Organization. `http://www.imo.net`, 2015. Accessed: 2015-09-18.

[59] J. E. McCoy. Photometric studies of light scattering above the lunar terminator from apollo solar corona photography. In Lunar and Planetary Science Conference Proceedings, pages 1087–1112, April 1976.

[60] H. McNamara, J. Jones, B. Kauffman, R. Suggs, W. Cooke, and S. Smith. Meteoroid Engineering Model (MEM): A Meteoroid Model For The Inner Solar System. Earth Moon and Planets, 95:123–139, December 2004.

[61] D. Nesvorný, D. Janches, D. Vokrouhlický, P. Pokorný, W. F. Bottke, and P. Jenniskens. Dynamical Model for the Zodiacal Cloud and Sporadic Meteors. Astrophysical Journal, 743:129, December 2011.

[62] David Nesvorny, David Vokrouhlický, Petr Pokorný, and D Janches. DYNAMICS OF DUST PARTICLES RELEASED FROM OORT CLOUD COMETS AND THEIR CONTRIBUTION TO RADAR METEORS. The Astrophysical Journal, 743(1):37–12, November 2011.

[63] H A Newton. An account of two meteoric fireballs, observed in the United States, Aug. 2, and Aug. 6, 1860, with computation of their paths; I. Meteor of August 2, 1860, 338; II. Meteor of August 6, 1860. American Journal of Science, Series 2 Vol. 33(99):338–348, May 1862.

[64] J. Oberst and Y. Nakamura. A search for clustering among the meteoroid impacts detected by the Apollo lunar seismic network. Icarus, 91:315–325, June 1991.

[65] M. E. Ockert-Bell, J. A. Burns, I. J. Daubar, P. C. Thomas, J. Veverka, M. J. S. Belton, and K. P. Klaasen. The Structure of Jupiter's Ring System as Revealed by the Galileo Imaging Experiment. Icarus, 138:188–213, April 1999.

[66] L. M. G. Poole. The structure and variability of the helion and antihelion sporadic meteor sources. Monthly Notices of the Royal Astronomical Society, 290(2):245–259, September 1997.

[67] A. R. Poppe, J. S. Halekas, J. R. Szalay, M. Horányi, and G. T. Delory. Model-data comparisons of ladee/ldex observations of low-energy lunar dayside ions. 45th Lunar and Planetary Science Conference, 1393, 2014.

[68] Andrew Poppe, David James, and Mihály Horányi. Measurements of the terrestrial dust influx variability by the Cosmic Dust Experiment. Planetary and Space Science, 59(4):319–326, March 2011.

[69] V. Porubcan and T. Jopek. Meteor Data Center. `http://www.astro.amu.edu.pl/~jopek/MDC2007/index.php`, 2015. Accessed: 2015-04-23.

[70] J. J. Rennilson and D. R. Criswell. Surveyor Observations of Lunar Horizon-Glow. Moon, 10:121–142, June 1974.

[71] Y. Saito, S. Yokota, T. Tanaka, K. Asamura, M. N. Nishino, M. Fujimoto, H. Tsunakawa, H. Shibuya, M. Matsushima, H. Shimizu, F. Takahashi, T. Mukai, and T. Terasawa. Solar wind proton reflection at the lunar surface: Low energy ion measurement by MAP-PACE onboard SELENE (KAGUYA). Geophys. Res. Lett., 35:24205, December 2008.

[72] L Saul, P Wurz, A Vorburger, D F Rodríguez M, S A Fuselier, D J McComas, E Möbius, S Barabash, H O Funsten, and P H Janzen. Solar wind reflection from the lunar surface: The view from far and near. Planetary and Space Science, 84(C):1–4, August 2013.

[73] A. B. Severny, E. I. Terez, and A. M. Zvereva. The Measurements of Sky Brightness on Lunokhod-2. Earth, Moon, and Planets, 14(1):123–128, 1975.

[74] David E Smith, Maria T Zuber, Gregory A Neumann, Frank G Lemoine, Erwan Mazarico, Mark H Torrence, Jan F McGarry, David D Rowlands, James W Head, Thomas Duxbury, Oded Aharonson, Paul G Lucey, M S Robinson, Olivier S Barnouin, John F Cavanaugh, Xiaoli Sun, Peter Liiva, Dan-dan Mao, James C Smith, and Arlin E Bartels. Initial observations from the Lunar Orbiter Laser Altimeter (LOLA). Geophysical Research Letters, 37(1):L18204, September 2010.

[75] F. Spahn, J. Schmidt, N. Albers, M. Hörning, M. Makuch, M. Seiß, S. Kempf, R. Srama, V. Dikarev, S. Helfert, G. Moragas-Klostermeyer, A. V. Krivov, M. Sremčević, A. J. Tuzzolino, T. Economou, and E. Grün. Cassini Dust Measurements at Enceladus and Implications for the Origin of the E Ring. Science, 311:1416–1418, March 2006.

[76] R. Srama, T. J. Ahrens, N. Altobelli, S. Auer, J. G. Bradley, M. Burton, V. V. Dikarev, T. Economou, H. Fechtig, M. Görlich, M. Grande, A. Graps, E. Grün, O. Havnes, S. Helfert, M. Horányi, E. Igenbergs, E. K. Jessberger, T. V. Johnson, S. Kempf, A. V. Krivov, H. Krüger, A. Mocker-Ahlreep, G. Moragas-Klostermeyer, P. Lamy, M. Landgraf, D. Linkert, G. Linkert, F. Lura, J. A. M. McDonnell, D. Möhlmann, G. E. Morfill, M. Müller, M. Roy, G. Schäfer, G. Schlotzhauer, G. H. Schwehm, F. Spahn, M. Stübig, J. Svestka, V. Tschernjawski, A. J. Tuzzolino, R. Wäsch, and H. A. Zook. The Cassini Cosmic Dust Analyzer. Space Science Reviews, 114:465–518, September 2004.

[77] M. Sremčević, A. V. Krivov, H. Krüger, and F. Spahn. Impact-generated dust clouds around planetary satellites: model versus Galileo data. Planetary and Space Science, 53:625–641, May 2005.

[78] S. A. Stern. The lunar atmosphere: History, status, current problems, and context. Reviews of Geophysics, 37:453–492, 1999.

[79] R. M. Suggs, D. E. Moser, W. J. Cooke, and R. J. Suggs. The flux of kilogram-sized meteoroids from lunar impact monitoring. Icarus, 238:23–36, August 2014.

[80] A. D. Taylor. Earth encounter velocities for interplanetary meteoroids. Advances in Space Research, 17:205–209, 1996.

[81] A J Tuzzolino, T E Economou, R B McKibben, J A Simpson, S BenZvi, L Blackburn, H D Voss, and H Gursky. Final results from the space dust (SPADUS) instrument flown aboard

the earth-orbiting ARGOS spacecraft. Planetary and Space Science, 53(9):903–923, August 2005.

[82] Fred L Whipple. A Comet Model. II. Physical Relations for Comets and Meteors. Astrophysical Journal, 113:464, May 1951.

[83] Paul A Wiegert, Jeremie Vaubaillon, and Margaret Campbell-Brown. A dynamical model of the sporadic meteoroid complex. Icarus, 201(1):295–310, May 2009.

Appendix A

Publications

A.1 Papers Published

- A. Stern *et al.* The Pluto system: Initial results from its exploration by New Horizons, *Science*, **350**(6258), 2015

- **Szalay, J. R.** and M. Horányi (2015), The search for electrostatically lofted grains above the Moon with the Lunar Dust Experiment, *Geophys. Rev. Lett.*, 42, doi:10.1002/2015GL064324.

- Horányi, M., **Szalay, J. R.**, Kempf, S., Schmidt, J., Gruen, E., Srama, R., and Sternovsky, Z. (2015), A permanent, asymmetric dust cloud around the Moon, *Nature*, **522**(7556), 324-326, doi:10.1038/nature14479

- Horányi, M. and **Szalay, J. R.** (2015), Dust charge measurements by the Lunar Dust Experiment, *Aerospace Conference, 2015 IEEE*, 7-14 March 2015, doi: 10.1109/AERO.2015.7119090

- Horányi, M., Sternovsky, Z., Lankton, M., Dumont, C., Gagnard, S., Gathright, D., Gruen, E., Hansen, D., James, D., Kempf, S., Lamprecht, B., Srama, R., **Szalay, J. R.** and Wright, G. (2014), The Lunar Dust Experiment (LDEX) Onboard the Lunar Atmosphere and Dust Environment Explorer (LADEE) Mission. *Space Sci. Rev.*, **184**(1-4), 93-113, doi:10.1007/s11214-014-0118-7

- **Szalay, J. R.**, Piquette, and M., Horányi, M. (2013), The Student Dust Counter: Status report at 23 AU. *Earth, Planets and Space*, **65**(10), 1145-1149, doi:10.5047/eps.2013.02.005

A.2 Papers in Review

- **Szalay, J. R.** and M. Horányi (2015), Detecting Meteoroid Streams with an In-Situ Dust Detector above an Airless Body, *Icarus*
- **Szalay, J. R.** and M. Horányi, Annual Variation and Synodic Modulation of the Sporadic Meteoroid Flux to the Moon, *Geophys. Rev. Lett.*
- Bagenal, F., *et al.*, Pluto's Interaction: Solar Wind, Energetic Particles, Dust

A.3 Papers in Preparation

- **Szalay, J. R.**, M. Horányi, *et al.*, Meteoritic Influence on the Lunar Exosphere
- **Szalay, J. R.** and M. Horányi, Analysis of Lunar Impact Ejecta Plumes Measured by the Lunar Dust Experiment
- Poppe, A. R., Halekas, J. S., **Szalay, J. R.**, Horányi, M., Levin, Z., and Kempf, S., LADEE/LDEX observations of lunar pick-up ion variability